System Level Challenges for Microfabricated Magnetoelastic Transducers in Implantable Biomedical Applications

by

Ramprasad Mohanan Nambisan

A dissertation submitted in partial fulfillment
of the requirements for the degree of
Doctor of Philosophy
(Electrical and Computer Engineering)
in the University of Michigan
2019

Doctoral Committee:

Professor Yogesh B. Gianchandani, Co-Chair
Dr. Scott R. Green, Co-Chair
Professor Raj R. Nadakuditi
Professor James D. Weiland

Ramprasad Mohanan Nambisan

rampmn@umich.edu

ORCID iD: 0000-0002-8674-0856

To my wife, parents, and Nikola Tesla

Acknowledgements

The work described by this dissertation was funded in part by the University of Michigan, and the National Institutes of Health. Samples for this work were provided by Metglas Inc. and Arnold Magnetic Technologies. Fabrication processes were performed at the Lurie Nanofabrication Facility.

I would like to express my sincere gratitude to my research advisor, Professor Yogesh Gianchandani, for his patience, motivation, and wise guidance that enabled me to think scientifically and execute pragmatic research. I am also heartily thankful to my co-chair Dr. Scott Green, for his insightful mentoring that nurtured my scientific curiosity. Our stimulating discussions were always exciting and inspiring. I would also like to thank my committee members, Prof. Nadakuditi and Prof. Weiland, for their guidance and suggestions on this research and dissertation.

Although not a part of my committee, I would like to thank Dr. Richard Kwon and Dr. Grace Elta for their contribution in executing animal tests for the biliary stent monitoring system. I am also thankful to Dr. Joshua Stein for his help in performing the *in situ* experiments for the actuator research. I would also like to thank Dr. Ying Han and Dr. Behzaad Amoozgar (University of California, San Francisco) for their valuable contribution to performing *in vivo* experiments for the actuator project. I am also thankful to the staff members at the University of Michigan Medical School, including Amber Yanovich, Gail Rising, Dr. Bob Sigler, Lauren Krueger, Rafael Ramirez,

and all the ULAM husbandry and veterinary technician staff, who assisted in the surgical operations, animal care, and *in situ* and *in vivo* experiments.

I would like to take this opportunity to thank my group members and 2001 office mates, including Tao, Yutao, Venkat, Yushu, Yu, Shiyang, Andy, Alex, Qisen, Jiqing, Neeharika, Jonathan, Partha, Sajal, Leo, Weilin, Daniel, Tsengun, Declan, Pengchao, Zeyu, Tal, Stacey, Amin, Ali, Yi, Christopher, Farzad, Sajal. Thank you all for the encouragement and support in both study and personal life. I would also like to thank my friends at the University of Michigan and in Ann Arbor.

Most importantly, I would like to thank my family. My mother, Sreedevi, always believed in me and inspired me to pursue my interests. My father, Mohanan, has always extended his unconditional support in my studies and career. I am grateful to my brother Ramdas also for his support and encouragement. Finally, I am thankful for the unconditional love, support, and inspiration from my wife, Arsha.

Table of Contents

List of Figures

List of Tables

List of Appendices

Abstract

Magnetoelastic devices have potential utility as sensors and actuators in implanted biomedical applications because of their inherent passive wireless nature which avoids the need for batteries and simplifies the implanted module. This work focuses on addressing system level challenges in two applications, one requiring an actuator and one a sensor. The first application is mitigation of glaucoma valve encapsulation; challenges addressed in this application include the integration of an actuator onto the valve and especially the development of an acoustomagnetic interrogation module for verifying actuator functionality. The second application is biliary stent monitoring; challenges include protection of the sensor during and after deployment, and development of an interrogation module with vastly increased wireless range.

An Ahmed glaucoma valve (AGV) is used in the treatment of glaucoma to drain fluid from the eye and decrease the elevated intraocular pressure. However, adhesion of cells and encapsulation of the AGV often lead to its failure. The magnetoelastic system described in this work consists of a magnetoelastic actuator integrated onto the AGV that can agitate the nearby liquid and potentially mitigate encapsulation, and an interrogation module to excite the actuator. The interrogation module addresses the signal feedthrough and clinical utility challenges by implementing physical domain decoupling and tailored signal processing. The *in situ* experiments with the system resulted in the first recorded acoustic signatures from a magnetoelastic sensor in an implanted environment; the measured signal-to-noise ratio was 3-6. *In vivo* experiments performed on live rabbits along with the *in situ* results indicate that the magnetoelastic system does

not adversely affect the health of the animal and can feasibly provide sufficient wireless range and actuation amplitudes after implantation.

A magnetoelastic system for biliary stent monitoring consists of a magnetoelastic sensor integrated into the stent, and an interrogation module to communicate with the sensor. The change in the resonant response of the sensor by mass loading and viscosity shifts due to sludge accumulation can diagnose early occlusion and allow timely intervention.

A self-biased sensor is designed and fabricated, decreasing the footprint considerably while preserving its resonant frequency. *In vitro* experiments mimicking sludge accumulation were performed, and the ratio of the shift in resonant frequency to the quality factor was found to be well-correlated with occlusion. The receiver operator characteristic of this parameter indicated an accuracy of 97.84% for a detection threshold of 50% decrease in flow rate through the stent due to occlusion. To protect the sensor during and after endoscopic deployment, a Nitinol reinforced polymer hybrid package is designed and used. *In vitro* tests utilizing bile-resistant bacterial cultures were conducted to evaluate the effect of the packaged sensor itself on the stent occlusion dynamics. Non-inferiority statistical tests performed on the results indicate that the instrumented stent is not inferior to the normal stent in terms of the occlusion time (p-value <0.05).

The implementation of the interrogation module addresses challenges, including wireless range, signal feedthrough, and clinical utility, and these are solved in part by time domain decoupling and signal processing techniques. The complete magnetoelastic system was successfully demonstrated *in vivo*, with the sensor-integrated stent implanted in the bile duct of a live pig at a wireless range of ≈17.15 cm with a signal to noise ratio $\approx 10^6$. These are the first reported signals from a stent-integrated magnetoelastic sensor implanted in a live animal.

Chapter 1: Introduction

1.1 Magnetoelastic sensors and actuators

Magnetoelastic devices are widely used as anti-theft tags in the retail sector. Expanding the use of these devices as sensors or actuators in different applications has recently been an area of study. Magnetoelastic sensors have been shown to be useful for environmental sensing, with measurands including temperature, pressure, and humidity [Gri99a, Gri00a, Kou00]. They have also been used for sensing physical properties like viscosity and density [Gri00b]. Several chemical/biological which use magnetoelastic devices have also been reported [Cai04, Rua04, Cai01]. Implanted biosensor applications have been explored for viscosity sensing, muscle stress sensing, and peripheral artery monitoring [Gur07, Pin01, Vis13].

In particular, magnetoelastic devices are attractive for implanted biomedical applications due to their inherent passive and wireless nature which eliminates the need for a battery implanted alongside the device [Gri99b, Ong05, Gre09a, Vis12, Pep15a, Nam17]. Additionally, the inherently wireless transduction mechanism eliminates the need for an implanted antenna. Both features reduce implant complexity and size. Another advantage is that these devices work at resonance, which helps to improve detection accuracy in noisy environments. The low cost of amorphous metals, which is one of the best-suited classes of magnetoelastic materials, is an added advantage.

Magnetoelastic devices vibrate at their resonant frequency in response to an oscillating magnetic field applied at a frequency of mechanical resonance. The vibration is due to the strain

caused by the alignment with an applied field of elongated magnetic domains that are tightly coupled with the material atomic structure. The mechanical vibration of the magnetoelastic device, in turn, launches magnetic waves, which can be sensed externally by using an inductive coil [Gri02a]. This physical phenomenon follows the linearized constitutive relations coupling stress, strain, magnetic field, and magnetic flux density [Kat59]:

$$[\varepsilon] = [s^H][\sigma] + [d][H] \tag{1.1}$$

$$[B] = [d]^T[\sigma] + [\mu^\sigma][H] \tag{1.2}$$

where $[\varepsilon]$ is the strain tensor, $[\sigma]$ is the stress tensor, $[s^H]$ is the compliance matrix at constant magnetic field intensity, $[d]$ is the magnetostrictivity matrix, $[H]$ is the magnetic field intensity, $[B]$ is the magnetic flux density, $[\mu^\sigma]$ is the permeability matrix at constant stress. These equations can be used in analytical modeling of the sensors or actuators [Gre09b, Pep15a]

A typical system consists of a magnetoelastic device and an interrogation module (Fig. 1.1). The magnetoelastic device can be either a sensor or an actuator, depending on the application. Magnetoelastic sensors are generally read by detecting resonant frequency shifts caused by the measurand, such as mass loading, changes in effective stiffness, or a change in viscosity/density of the medium surrounding the device. An external interrogation module is used to excite the magnetoelastic device and sense the magnetic field or acoustic field generated from the sensor using an inductive coil or an acoustic sensor. Although magnetoelastic actuators do not require measurement of the frequency response, its availability allows the verification of vibration or operation in a servo-controlled fashion.

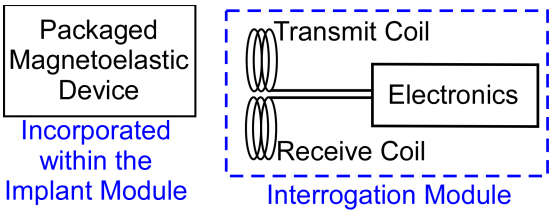

Fig. 1.1: A typical system consists of a magnetoelastic device and an interrogation module.

In spite of these advantages and interesting benefits of magnetoelastic devices, there are several open challenges in using these devices in implanted biomedical applications. There are specific challenges associated with the design and fabrication of the magnetoelastic device, its integration to the implant module, and the development of an interrogation module for communicating with the implanted device.

A major challenge in device design and fabrication is miniaturization to reduce its impact while incorporating it into the implant module. The incorporated device must not introduce significant interference to the existing functionality of the implant module; for example, a sensor (device) meant to monitor stent occlusion should not vastly accelerate the occlusion of the stent (implant module). Also, the accommodation of the standard implantation procedure plays a major role in designing the device as well as a protective package if needed.

There are also specific challenges associated with the design and implementation of the interrogation module. The excitation signal that is directly received by the receive coil can obscure the response of the implanted sensor and is termed signal feedthrough. Overcoming this feedthrough is one of the major challenges. The miniaturized sensor also poses the challenge of reduced wireless range due to reduced sensor response. Finally, the clinical utility of the interrogation module must also be considered for the practical implementation of these devices for implanted biomedical applications.

This work focuses on two applications which are representative of these challenges. The first application is a magnetoelastic actuator that agitates liquid locally and minimizes fibrosis in glaucoma valves. This application has specific challenges in terms of integration of the actuator onto the valve and in terms of the interrogation approach for verifying the actuator functionality after implantation. The second application investigated in this work is a magnetoelastic sensor for monitoring sludge deposition in biliary stents, which will help in diagnosing stent occlusion. In this application, the specific challenge regarding sensor miniaturization is avoiding any effect of the sensor on existing stent functionality. The sensor protection while stent implantation is also another major challenge addressed in this work. Finally, the challenge of development of an interrogation module addressing signal feedthrough, wireless range, and clinical utility is addressed. In the following sections, the backgrounds of – and open challenges facing – these specific applications are described in detail.

1.2 Mitigation of glaucoma valve encapsulation

1.2.1 Background

One of the implantable applications of magnetoelastic devices targeted in this work is in the mitigation of glaucoma valve encapsulation. Glaucoma is a leading cause of blindness in the world. One of the treatments for glaucoma involves implanting a mechanical valve in the eye, which drains the aqueous humor and reduces intraocular pressure. However, this valve becomes encapsulated by fibrous tissue which leads to its eventual failure in as many as 72% of devices [Cvi16]. Recent efforts have proposed the integration of a magnetoelastic actuator onto this valve, and the mechanical vibrations of this valve can agitate the liquid around, minimizing the cell adhesion and subsequent encapsulation [Pep15b]. The actuator, along with an interrogation module to excite it and measure and verify its response, constitute a magnetoelastic system for this

application. The open challenges associated with this system include the integration of the actuator onto the valve and the verification of actuation after implantation using the interrogation module. These challenges are addressed in this work.

Glaucoma is an eye disease which is estimated to be affecting eighty million people worldwide by 2020; 11.1 million people are estimated to be bilaterally blind from glaucoma by 2020 [Qui06]. The resistance to the outflow of aqueous humor (AH) from the eye that results in elevated intraocular pressure (IOP) is a major risk factor for the development of glaucoma [Roh83]. This elevated IOP results in damage to the optic nerve, leading to loss of peripheral vision and if left untreated, blindness. One effective treatment of glaucoma is to surgically implant an Ahmed glaucoma valve (AGV), which is a mechanical valve that helps to lower IOP by creating a new pathway for AH to exit the eye [Ged07]. The AH exits through the lumen of the AGV and collects around the AGV, forming a reservoir. Over time, adhesion of endothelial cells can lead to a fibrous capsule formation around the AGV which, in turn, limits the size of the reservoir and increases the resistance to AH outflow [Mol03, Eib05, Lee14, Cho10] (Fig. 1.2).

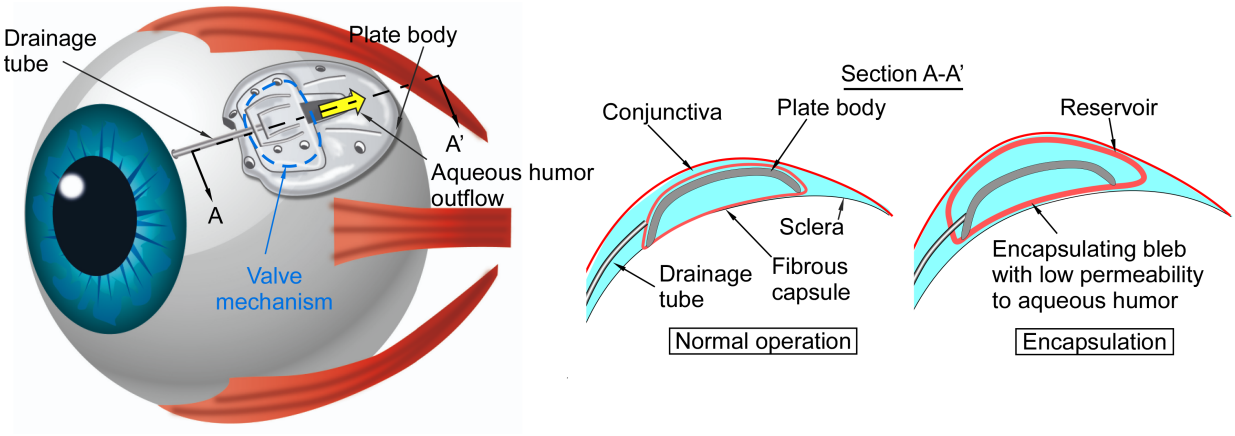

Fig. 1.2: Schematic of implanted AGV on the eye (left). (b) Schematic of normal operation and encapsulation (right) [Pep15a].

Although several chemical and physical surface modifications have been proposed to limit fibrosis, these have mostly been ineffective [Par02]. Previously reported benchtop tests have

shown that magnetoelastic microactuators can locally agitate the fluid to potentially limit cell adhesion and fibrosis [Ito11, Vla11]. A magnetoelastic actuator can be integrated onto the valve which vibrates at its resonance frequency in the presence of an external magnetic field. The vibrating actuator agitates the liquid around it. This liquid agitation is intended to mitigate the adhesion of cells onto the valve and thus reduce the extent of fibrous encapsulation.

An interrogation module is used to remotely interact with the implanted actuator. This interrogation module can either provide just an excitation to the actuator, or it can combine excitation of the actuator with some measurement of the actuator response. An interrogation module which can verify the vibratory response from the actuators after implantation is useful. This verification would help to confirm the functionality of the actuator and can be used to adjust the therapeutic parameters. For example, changes in the implanted environment, including tissue accumulation, can result in a resonant frequency shift. By measuring the frequency response of the actuator with an interrogation module, a feedback loop can be used to adjust the actuation frequency accordingly.

1.2.2 Challenges in actuator design and solution strategies

There are several challenges associated with the design and fabrication of an actuator that can be integrated onto an AGV for this application. This actuator should have a small footprint in order to reduce its impact on the size of the valve and the implantation process. The actuator also must be curved to conform to the surface of the valve to prevent further irritation of the eye. Previously reported works have utilized an annealing method using aspherical molds to curve the actuators [Pep15b].

The integration of the actuator onto the AGV itself presents a challenge, and additionally, the actuator must be biocompatible and protected from corrosion since it is in a liquid environment.

Actuator coating techniques are investigated to address these challenges. Mounting of the actuator onto the AGV must account for the dissimilarities in the two materials – the AGV is silicone rubber while the actuator is a metal alloy. The effects of mounting to a high-mechanical-loss substrate – like silicone rubber – on the vibratory response of the actuator must also be considered and evaluated. These challenges are investigated in this work.

1.2.3 Challenges in interrogation and solution strategies

The interrogation of the actuator for mitigation of glaucoma encapsulation poses several challenges due mainly to the aspherical actuator structure and immersion of the actuator in a fluidic environment. Three major challenges focused on here in this work include; (i) signal feedthrough; (ii) wireless range; and (iii) clinical utility. The interrogation module developed in this work focuses on overcoming these challenges.

One of the critical considerations associated with developing an interrogation module for magnetoelastic devices is the approach for reducing signal feedthrough. The signal feedthrough is defined as the superposition of the excitation magnetic field on the sensor magnetic field at the receive coil. Physical domain decoupling is used to tackle the signal feedthrough issue in this application. The magnetoelastic actuator of this application will vibrate at a resonant frequency in the presence of an excitation magnetic field at that frequency. However, electromagnetic detection of the response cannot be applied with the particular actuators studied here. This is because the flexural vibrational modes of the curved actuators have opposing strain patterns (i.e., some portions of the material is in tension while other nearby portions are in compression), resulting in a weak cumulative electromagnetic response. As such, this work utilizes other means for detecting the frequency response of the actuator. Initially, verification of actuation with a laser displacement sensor is investigated. However, that method requires precise positioning of the laser onto the

actuator, and the laser may be obscured by tissue overlying the actuator in the implanted situation. Thus, this work further investigates an interrogation module that senses the acoustic signals from the magnetically excited actuator. Actuation in the magnetic physical domain and sensing in the acoustic domain results in physical domain decoupling, which minimizes the signal feedthrough.

The acoustic signal detected is noisy due to the presence of background signals and results in a low wireless range. The module developed in this work utilizes a series of digital signal processing steps to tackle this challenge and improve the wireless range. Relative to laser displacement sensing, this acoustomagnetic and signal processing method has improved the SNR as well as eliminated the issues with precise positioning and movement of the eye, both of which are important for *in vivo* use.

The *in situ* experiments indicate that the frequency shift after implantation is not significant, and hence, feedback is not necessary over a short-term period (Section 2.7). As such, a simple patient-friendly module consisting of only the actuation capability (without feedback) is developed for the *in vivo* experiments. A range of frequencies is used to excite the actuator, and this module only consists of the actuation mechanism with no response detection or feedback loop; this simplifies the module for ease of use in the clinical environment. *In vivo* experiments were performed on live rabbits as subjects. The *in vivo* results presented in this work indicate that the implanted actuator does not adversely affect the health of the animal. The *in situ* results indicate that the magnetoelastic system can feasibly provide sufficient wireless range after implantation.

1.3 Biliary stent monitoring

1.3.1 Background

Another promising use of magnetoelastic systems is in biliary stent monitoring. Plastic biliary stents are prone to occlusion due to sludge deposition in the stent. Previous works have reported the integration of a magnetoelastic sensor into the stent for monitoring this sludge deposition [Gre07, Gre08, Gre09b, Gre10, Gre13], which will subsequently help in occlusion diagnosis. However, these works have not addressed challenges in terms of miniaturizing the sensor, integrating the sensor into the stent, and increasing the distance from which the sensor can be interrogated while maintaining a strong signal to noise ratio (SNR). The work here focuses on overcoming these challenges related to this specific application.

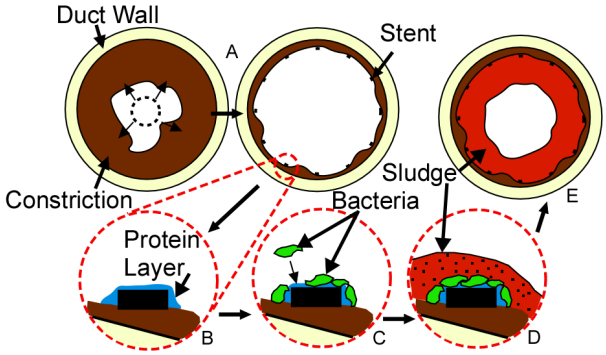

Fig. 1.3: Schematic of sludge formation and stent occlusion for a biliary stent [Gre09b].

Typical plastic stents have the complication of stent occlusion due to "sludge" formation [Don07] (Fig. 1.3). The bile duct carries the bile from the liver and gallbladder to the duodenum, which is a part of the small intestine. A biliary stent relieves the constricted bile duct, with the stricture caused by pancreatitis, cholangitis, tumors, surgical injury, duct breakdown due to gallstones, collagen deposition, or duct tissue fibrosis [Lib96, Fra96]. At the beginning of occlusion, a protein layer starts to form on the stent surfaces. Then, on this protein layer, bacteria starts to adhere, collects, and forms an extracellular biofilm and matrix. The enzymes produced by the bacteria precipitate the cholesterol and calcium bilirubinate in the bile solution, and these

precipitates deposit in the extracellular matrix. Altogether this matrix, biofilm, and bacteria form "sludge" which occludes the stent. Solutions to this stent occlusion due to "sludge" formation are either stent replacement or insertion of another stent within the original stent.

There are several medical methods for diagnosing stent occlusion. One of the methods is a blood test known as a liver function test. Abnormal levels of enzymes formed by the liver can be an indication of a malfunctioning liver due to the occluded stent. However, this indirect measurement method can give an indication of occlusion very late or can indicate abnormal liver function not associated with the stent. Other methods include imaging by ultrasound or magnetic resonance, which can typically image only the outer surface of the stent and can detect occlusion at later stages based on bile duct dilation upstream of the stent. However, these imaging methods are not effective at detailing the interior of the stent or at detecting early progression of occlusion. The integration of a magnetoelastic sensor has the potential to help in early occlusion detection and decisions on appropriate treatment, allowing the avoidance of both unnecessary stent replacements and high-risk infections.

The magnetoelastic sensor integrated into the stent is remotely interrogated using an external interrogation module. The wireless interrogation module induces resonant vibration and senses the magnetic field generated by the sensor, allowing the resonant frequency and quality factor to be determined. These parameters are indicative of the sludge build-up. The resonant magnetoelastic sensor vibrates at maximum amplitude at its resonant frequency. Any mass deposition due to sludge accumulation onto the sensor will result in a shift in this frequency as well as a reduction in quality factor (Fig. 1.4).

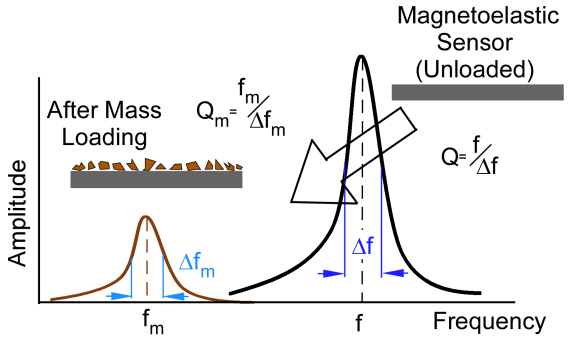

Fig. 1.4: Deposition of viscoelastic material onto the resonant sensor results in a shift in resonant frequency as well as (typically) a reduction of the quality factor.

1.3.2 Challenges in sensor design and solution strategies

There are several challenges associated with the design and fabrication of the magnetoelastic sensor and its integration to the stent for monitoring the biliary stent. These include: (i) the miniaturization of the sensor without significant signal reduction; (ii) packaging of the sensor for protection during implantation and integration of the packaged sensor with the stent.

Sensors must be small in order to be assembled in a biliary stent. Typical plastic biliary stents have outer diameters 0.33 cm (10 Fr) or 0.38 cm (11.5 Fr), and the shape and size of the sensor need to be such that the sensor introduces minimal obstruction to the bile flow through the stent. A solution to this is to have thin ribbon sensors along the inner sidewall of the stent. The small cross section of these sensors is not expected to significantly affect the bile flow through the stent. Long sensors can give better signal compared to shorter ones, but they are not ideal in this application because the stent tends to undergo tight longitudinal curvature during endoscopic deployment into the bile duct [Jia18b]. Long sensors are particularly stressed by this tight curvature, which can lead to sensor damage during implantation or a decrease in signal strength. While fabricating small sensors is straightforward, the critical challenge in miniaturization is that small sensors generate weaker signals at higher resonant frequencies. These effects, in combination, add to the challenge in detecting signals from a miniaturized sensor at practical

wireless ranges. One of the main objectives of the sensor design presented in this work is to reduce the sensor footprint while maintaining the resonant frequency and preserving the signal amplitude.

A simple approach to reduce the resonant frequency is to increase the length of the resonator, but this will also increase the size of the resonator, defeating the miniaturization goal. Reducing the stiffness of the resonator also decreases the resonant frequency. This can be done, for instance, by adding perforations to the structure, as examined in prior work on magnetoelastic sensors [Gre09b]. However, this approach typically introduces local areas of in-plane bending and requires removing material, both of which can have a negative effect on the signal amplitude. Alternatively, the effective mass can be increased to lower the resonant frequency. This can be done by attaching mass strategically, which is the method examined in this work. Also, a magnetoelastic sensor must be biased with a DC magnetic field for higher vibrational amplitudes. In general, the DC bias is either provided by external coils with DC current or small magnets placed next to the sensor. External coils are not ideal for most wireless applications where the sensor position may vary because it is difficult to apply a consistent bias field externally, and also as the distance between the sensor and coil increases, high power is required to generate sufficient bias strength. However, placing small magnets adjacent to the sensor increases the total device footprint, and any small change in air gaps between the magnets and the sensor can significantly alter the sensor performance. In this work, the mass loads on the sensor itself can acts as magnets, making the sensor self-biased. This helps in reducing the sensor footprint considerably while providing an extremely consistent DC bias.

Another challenge is to protect the sensor during and after implantation. The biliary stent is deployed in the bile duct by endoscopy. These stents are available in various lengths, typically from 5 cm to 10 cm. The stent and sensor need to pass through the endoscope during deployment.

During deployment, the stent and sensor are passed over an introducer – a relatively small, long tube that passes through the endoscope and is placed in the bile duct to act as a guide for the stent. The introducer itself has a diameter of 1.7 mm (for a 10 Fr stent) or 2 mm (for an 11.5 Fr stent). The introducer is a vital part of the stent delivery process, and its mechanical interaction directly with unprotected sensors is likely to cause damage [Gre13]. This indicates the need for a package to protect the sensor during implantation.

There are a number of requirements for any such package. The package must be biocompatible and chemically inert such that it does not affect the tissue around it after implantation. Also, it must be electromagnetically transparent so as not to affect the sensor signal. The stent goes through extreme longitudinal curvature when passing through the endoscope during the implantation procedure (Fig. 1.5(a)). To withstand this tight radius of curvature (R_c ~2 cm), the sensor package must be flexible without being easily plastically deformed or damaged. Also, the stent after implanted is under stress due to the anatomical curvature of the bile duct, as shown in Fig. 1.5(b). This bile duct curvature also tends to bend the compliant stent (R_c ~5 cm). To keep the sensor straight in the stent, the package must be stiff enough to oppose the anatomical curvature and minimize signal attenuation due to sensor bending. Previous work used polymer structures to tackle this, but these structures were found to be either too flexible or too inelastic and thus ineffective after deployment [Jia18a, Jia18b].

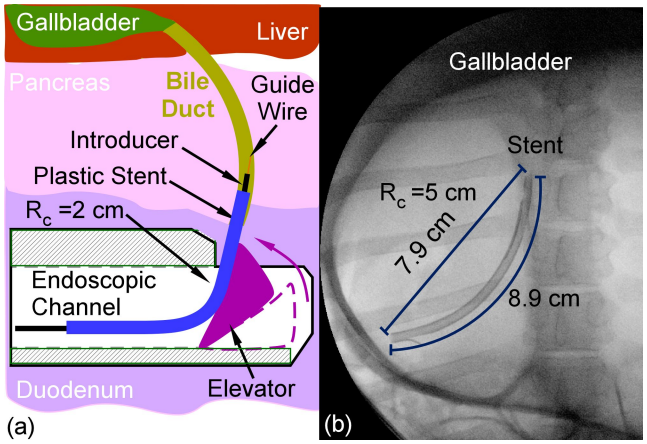

Fig. 1.5: (a) Stent passing through the endoscope with elevator at maximum raised position, the radius of curvature (Rc) =2 cm. (b) Radiographic image of an implanted stent showing the inherent anatomical curvature of the bile duct with Rc =2 cm.

This work uses a novel hybrid approach using a 3D printed polymer package with metal reinforcing features in order to meet the performance requirements. Benchtop and *in vitro* tests are used to evaluate the robustness of this package. The packaged sensor is bent in curvatures representative of those required during endoscopic deployment and in the bile duct anatomy. Of course, the addition of the package and sensor to the internal surfaces of the stent could lead to more rapid sludge development and negate the benefits of the sensing system. *In vitro* experiments are performed with test and control stents to evaluate the difference in the sludge development process in an instrumented stent relative to a non-instrumented stent.

1.3.3 Challenges in interrogation and solution strategies

The challenges associated with the interrogation of magnetoelastic sensors for biliary stent monitoring are similar to those discussed in the previous section 1.2.3. These challenges include (i) signal feedthrough; (ii) wireless range; and (iii) clinical utility. The specifics of this application change the nature of each of these challenges. The interrogation module developed in this work focuses on overcoming these challenges.

The issue of signal feedthrough results in the obscuration of the sensor signal, as shown

in Fig. 1.6. The reduction of signal feedthrough can allow larger transmission fields and more sensitive receive circuitry, which can boost wireless range or enable sensor size reduction. One approach to avoid this signal feedthrough issue is time domain decoupling. With this method, the sensor is excited using a short transmitted burst, and then the ringdown response of the sensor is measured. This is illustrated in Fig. 1.5. This contrasts with a previously used method that used continuous transmission and reception and was limited by significant signal feedthrough as well as shifts in the electromagnetic characteristics of the media near the receive coil (for instance, due to respiration or movement of the patient) [Gre09b].

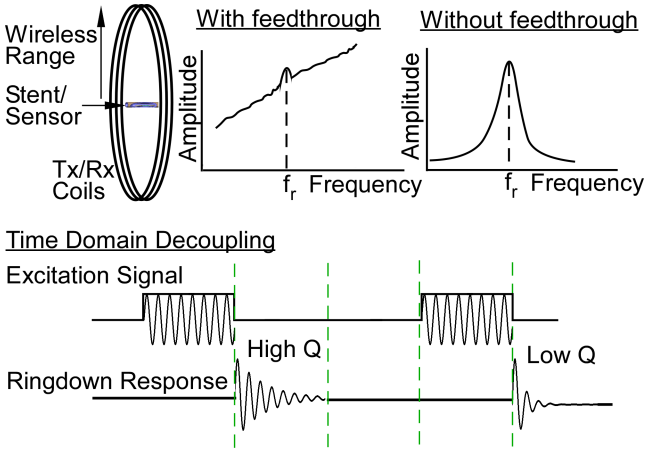

Fig. 1.6: Challenges in the interrogation of a magnetoelastic sensor and time-domain decoupling approach.

While feedthrough can be significantly reduced with the time domain decoupling method and it has shown to be useful in the rapid interrogation of magnetoelastic strain sensors [Gri02b, She10, Pep17], there is a drawback to the method in the context of implantable resonators. Because such resonators are typically immersed in a viscous fluid, the quality factor of the resonance is relatively low. During ringdown, this manifests itself as a low amplitude and quickly decaying signal envelope. As such, the interrogation module must have sufficient sensitivity and transmit-to-receive switching speeds to capture this signal.

Another challenge in interrogating the implantable magnetoelastic sensors is the wireless range. The magnetic field generated by the sensor decays rapidly with distance, which makes the detection extremely difficult at a longer range. For example, the signal strength decreases 25-fold for a 1.5-fold increase in interrogation distance (Section 5.4.1). Also, the magnetic field generated by the sensor decreases as the sensor size is scaled down. A signal strength decrease of 15-fold is reported for a sensor with the length halved [Jia18b]. A series of digital signal processing techniques, along with careful hardware choices, are performed in this work in order to minimize the noise and achieve a high SNR. A comparison of the wireless ranges achieved from sensors of various footprints in the previous works to those achieved in this work is illustrated in Fig. 1.7.

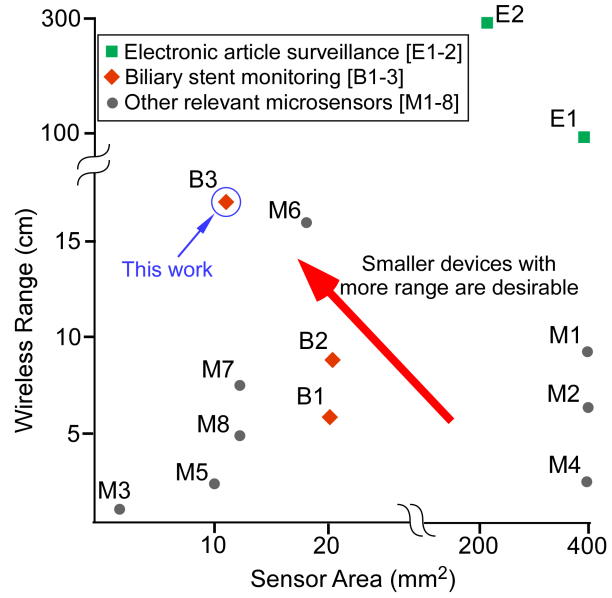

Fig. 1.7: Comparison of wireless range and sensor size achieved in this work to previous works in magnetoelastic sensors.

Finally, the interrogation module design must consider clinical utility. The interrogation time must be short for clinical tests, and the hardware components for testing must introduce

minimal inconvenience to the patient. The module must also accommodate anatomical variations in the position and orientation of the sensor with respect to the interrogation coils. These points are considered while hardware implementation for the interrogation module.

1.4 Organization of this report

The two main goals for this thesis are: (i) investigate and demonstrate a magnetoelastic system for mitigation of glaucoma valve encapsulation *in vitro*, *in situ,* and *in vivo*. (ii) investigate and demonstrate a magnetoelastic system for biliary stent monitoring *in vitro*, *in situ,* and *in vivo*. This first chapter has introduced these two applications of magnetoelastic sensors and actuators: biliary stent monitoring and glaucoma valve encapsulation mitigation. This chapter also presented the challenges associated with sensor design and fabrication, interrogation modules in both the applications and overarching goals for the work. These challenges are:

- Integration of a magnetoelastic actuator onto a glaucoma valve
- Implementation of an interrogation module for verification of implanted actuator
- Design and fabrication of a miniaturized sensor for biliary stent
- Design and fabrication of a protective package and packaged sensor integration onto stent
- Implementation of an interrogation module for communicating with the implanted sensor

The remainder of this dissertation is organized as follows. The magnetoelastic system for mitigation of glaucoma valve encapsulation is discussed in chapter 2. Chapter 3 discusses the design and fabrication of the miniaturized sensor for biliary stent monitoring system. The design and fabrication of the in-stent hybrid package for protecting the sensor are discussed in chapter 4. Chapter 5 discusses the interrogation module developed for the biliary stent monitoring system

and the demonstration of the complete system *in vivo*. Finally, chapter 6 summarizes the major contributions of this work and the potential future efforts.

The second chapter describes the interrogation module for actuation and verification of the actuation of magnetoelastic actuators integrated onto a glaucoma valve. The vibration of the excited actuator is intended to reduce the cell adhesion and fibrous capsule formation, improving the efficacy of these valves. This interrogation module also includes sensing for verification of actuation to ensure that the actuator is functional over the implant period. A physical domain decoupling approach is implemented in this module. A series of DSP techniques are implemented for improving the SNR and wireless range. This chapter discusses the benchtop experiments with the actuator using the developed interrogation module. Finally, this chapter discusses the *in situ* and *in vivo* experiments conducted.

The third chapter details the miniaturized self-biased sensor design, and fabrication methods. The sensor structure is a rectangular beam with two mass loads, one on each longitudinal end. These mass loads act as magnets to bias the sensor as well as help in preserving a low resonant frequency. The sensor is fabricated using microfabrication tools, including micro-electro-discharge machining, and the mass loads are attached at the longitudinal ends using a transient liquid phase bond. This chapter also includes the *in vitro* experiments performed, mimicking the sludge accumulation and sensor sensitivity results.

The fourth chapter discusses the design and fabrication of hybrid packages for protecting the magnetoelastic sensors for biliary stent monitoring. The hybrid package presented here is a polymer structure reinforced by highly elastic Nitinol wires to strike a balance between the required elasticity and stiffness for successful endoscopic deployment. Bending tests were carried out to ensure that this hybrid package is able to tackle the mechanical challenges of delivery and

deployment. This chapter also discusses the effect of the packaged sensor itself on the occlusion dynamics. Finally, *In vitro* tests, including culturing of bacteria in bile and flowing the mixture through both package-instrumented stents and normal stents, were carried out to evaluate the effect of the package on occlusion dynamics.

The fifth chapter describes the implementation of an interrogation module for the biliary stent monitoring system. This interrogation module works on time domain decoupling approach to minimize the signal feedthrough and careful hardware implementation for improving the wireless range. Several digital signal processing techniques are also used to improve the signal to noise ratio. Finally, this chapter also discusses the successful *in vivo* experiments with a porcine subject for a demonstration of the complete biliary stent monitoring system. Finally, chapter 6 summarizes the performance of these two magnetoelastic systems and discusses the major contributions of this work to the field. This chapter also describes future potential work to improve these systems.

Chapter 2: Magnetoelastic System for Mitigation of Glaucoma Valve Encapsulation

2.1 Introduction

In this chapter, a magnetoelastic system for use in glaucoma valve encapsulation mitigation is discussed, particularly concerning the development and characterization of an appropriate interrogation module. As described in Chapter 1, a magnetoelastic actuator can be integrated onto the glaucoma valve, and the vibration of the actuator at resonance can agitate the liquid around it and potentially mitigate the onset or acceleration of fibrous encapsulation of the valve. The system level challenges in this application include (i) the fabrication of magnetoelastic actuators and their integration onto an AGV, and (ii) the challenges associated with the interrogation module including signal feedthrough, wireless range, and clinical utility. These challenges are addressed in this work.

The following sections focus on the approaches used to overcome these challenges and experimental demonstrations of the system. First, the challenges with respect to the actuator fabrication and integration onto the AGV are discussed. Subsequently, the benchtop experimental results of an interrogation module using a laser displacement sensor are presented. Challenges with this module are addressed by an acoustomagnetic interrogation module which utilizes a hydrophone; the concept and design for this module are presented. The benchtop, *in vitro,* and *in situ* experimental results with this acoustomagnetic module are then discussed. Further, a simplified interrogation module is developed for *in vivo* experiments, and the *in vivo* experiments with this simplified module are detailed, followed by conclusions.

2.2 Fabrication of magnetoelastic actuator and integration onto the AGV

The challenges associated with the magnetoelastic actuator for glaucoma valve encapsulation mitigation include its fabrication, corrosion protection of the actuator – since the valve is in a liquid environment – and finally, the integration of the actuator onto the AGV. The magnetoelastic actuator for this application must be a three-dimensional structure so that it can be conformally be integrated on to the curved surface of the AGV. A three-dimensional aspherical structure also allows for out of plane vibrations that can agitate the liquid around. First, the actuators are fabricated from 28 μm thick Ni/Fe foil (Metglas^{TM} 2826MB) using photochemical machining. These fabricated actuators are planar and were sandwiched between the Cobalt-Chrome alloy molds of exaggerated curvatures and annealed at 275ºC for 12 hours. These curved actuators can then conform to the curved surface of the AGV. This fabrication procedure is adapted from previous work [Pep15b].

The actuator has several structural features – including paddles, anchors, and springs – which allow the actuator to vibrate effectively to agitate the surrounding fluid. The paddles are specifically for moving the liquid around, while the springs help to enable out of plane vibration and reduce losses through the valve substrate. Two designs are used in this work; Type I has paddles with a joint, whereas Type II has continuous paddles, as shown in Fig 2.1. Experiments have demonstrated that both of these designs can agitate the liquid around it; only the mode shapes differ [Pep15b]. The schematics of these two types of actuators are shown in Figure 2.1. The overall size of both actuator types is 10.3 × 5.6 mm^2 with minimum features of 125 μm.

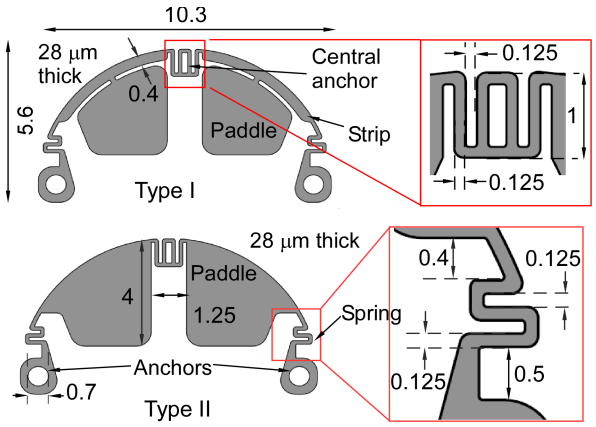

Fig. 2.1: Schematic of Type I and Type II actuators [Pep15b].

The specific challenges addressed in this work are corrosion in the liquid medium and valve mounting issues. A 100 nm-thick aluminum oxide is coated onto these actuators using atomic layer deposition (ALD) in order to provide biocompatibility and to prevent corrosion. Experimental results showing the efficacy of this approach are presented in a later section of this chapter. The actuator is a metal alloy, and the AGV is made of silicone rubber. This poses a challenge in attaching the actuator onto the AGV, due to its deformability and relatively low surface energy. Several experiments were conducted with various biocompatible epoxies, and NuSil epoxy (Med3-4213) was found to be effective and was used to bond the actuator onto the AGV. This is a two-part epoxy which is biocompatible, and a two-part side-by-side kit adapter and mix tip are used to prepare the epoxy in a 1:1 ratio. The epoxy is applied to cover the entire anchor of the actuator, as shown in Fig. 2.2.

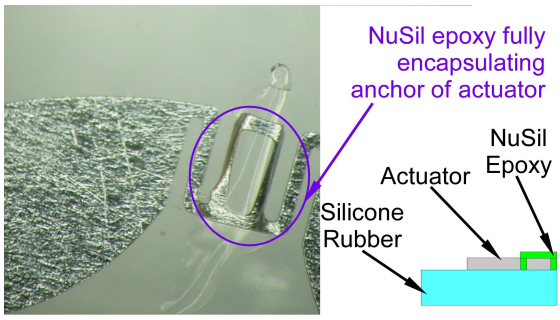

Fig. 2.2: Photograph and schematic of the application of NuSil epoxy onto the actuator.

The bond is then cured in an oven at 100°C for 30 mins and cured further for 12 hours at room temperature. The bond was strong enough that the separation force applied deformed the actuator before breaking the bond apart. Type I and Type II actuators mounted on AGVs using this technique are shown in Fig. 2.3.

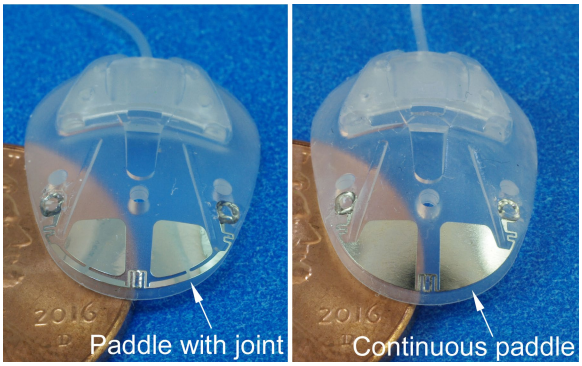

Fig. 2.3: Actuators mounted on AGVs. (a) Type I; (b) Type II.

2.3 Interrogation using a Laser Displacement Sensor

This section describes the development of an interrogation module for the magnetoelastic actuators for glaucoma valve encapsulation mitigation using a laser displacement sensor. The actuators need to be excited, but also the interrogation must include a detection mechanism for the verification of actuation. Confirmation of actuation is required to ensure that the actuator is operational after the implantation as the tissue heals and grows. Experiments demonstrating that actuation can be measured with this set-up when the actuator is in water and under the conjunctiva

simulant layer were conducted. The experimental set-up developed toward this goal is shown in Fig. 2.4.

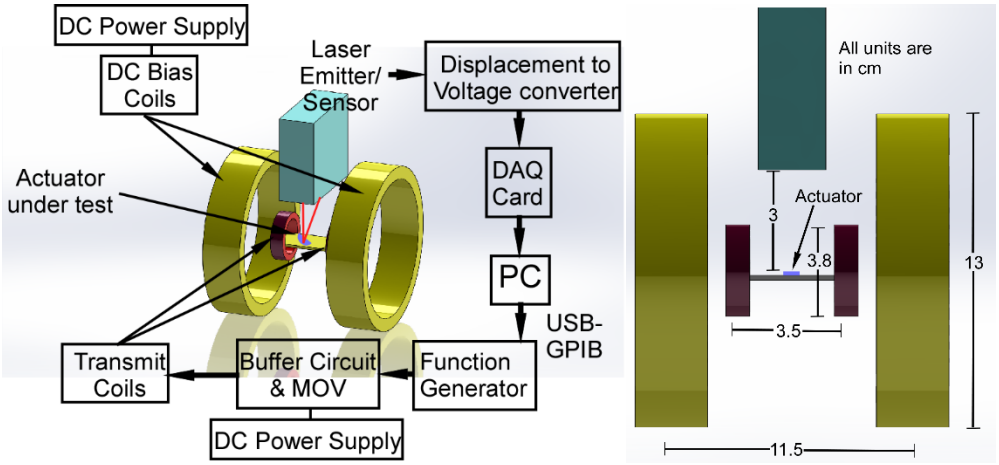

Fig. 2.4: Interrogation module using a laser displacement sensor for exciting the actuator as well as for the verification of actuation.

This interrogation module consists of an inductive transmit coil for actuation, a laser displacement sensor for sensing the vibration and several hardware components. In this module, the required AC magnetic field is generated via inductive transmit coils and DC bias by a commercial Helmholtz coil system. The transmit coils consist of two coils in parallel with each having 100 turns. The function generator (Agilent 33220A) generates the required sine wave and is programmed by the PC using GPIB-USB-HS cable (National Instruments). The buffer circuit (with a buffer amplifier) and metal oxide varistor (MOV) (More details on this is in Chapter 6) is for protecting the function generator from any fly-back voltage from inductive coils. For the verification of actuation, a laser displacement sensor (Model LK-G32, Keyence) (LDS) is used. The laser is pointed onto the paddle of the actuator for displacement measurements. As the actuator vibrates, the LDS senses the displacement of the paddle, and this data is collected to the PC using a data acquisition device (National Instruments DAQmx).

A series of signal processing techniques were implemented in LabVIEW to improve the SNR and subsequently, the wireless range. Filters were optimized, and group delay (GD) compensation was implemented in order to efficiently recover the signal. The details of the signal processing techniques are discussed later in this chapter. With this set-up, actuation was measured in water and under conjunctiva simulant (a silicone contact lens draped over the actuator), and results are illustrated in Fig. 2.5. For these experiments, the actuators were mounted onto metal plates rather than onto a real AGV.

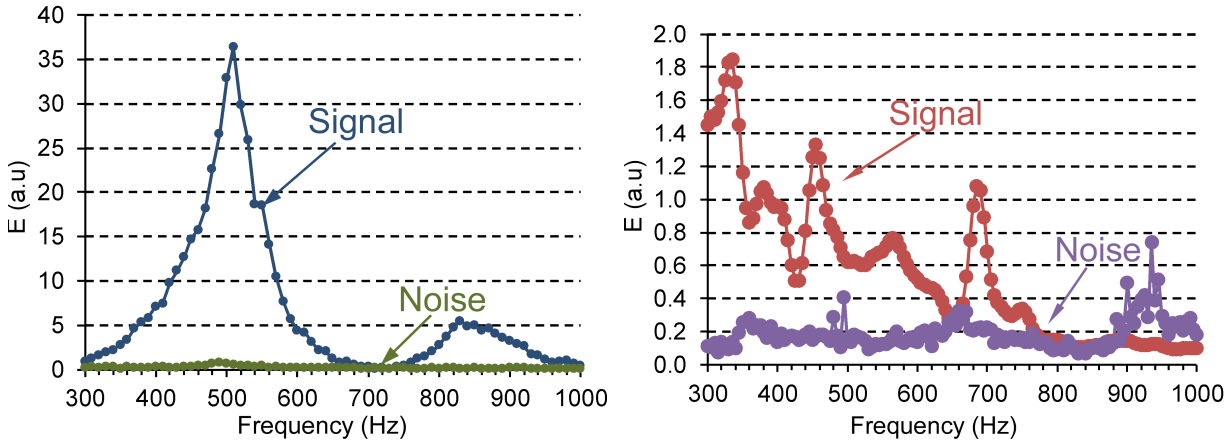

Fig. 2.5: Frequency response from the actuator Type I in water (left), in water with conjunctiva simulant (right).

This interrogation module developed using an LDS for detection of the vibration of the actuator could successfully excite the actuator and detect the actuator vibrations indicating the actuator functionality. Fig. 2.5 shows that the actuator resonance occurs at ~480 Hz. Although the signal reduced and the resonant frequency shifted lower after introducing the conjunctiva simulant, the interrogation module could successfully verify the actuation.

2.4 Acoustomagnetic interrogation module

The interrogation module using LDS posed several drawbacks which led to the development and interrogation module using a hydrophone. Although the vibration of the actuator was successfully verified using the interrogation module with LDS, the SNR in the case with a conjunctiva simulant was weak. Moreover, this method requires precise positioning of the laser onto the actuator, and the laser may be obscured or scattered by tissue overlying the actuator. A laser detection method also has a potential blinding hazard associated with it. In contrast, an alternate approach using a hydrophone may be less sensitive to precise positioning and eye movement and is investigated. This approach is similar to the ophthalmologic B-scan ultrasonography, indicating clinical utility. The actuator is excited magnetically, and the acoustic response from the vibrating actuator is detected in this module. This physical domain decoupling eliminates the issue of the signal feedthrough. Various signal processing techniques are also implemented to improve the SNR and thus wireless range. The schematic of the interrogation module is illustrated in Fig. 2.6.

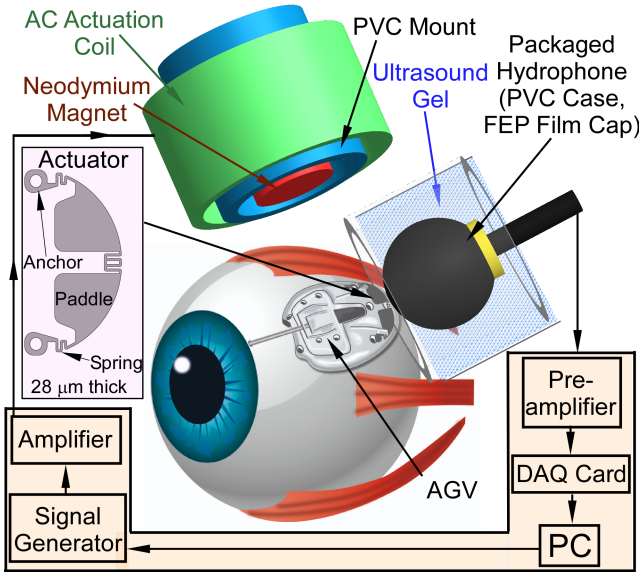

Fig. 2.6: Interrogation module using hydrophone for glaucoma valve encapsulation mitigation

The interrogation system consists of several hardware for the excitation of the actuator and detection of the signals generated by the actuator. A signal generator (Keysight 33220A) along with a power amplifier (Krohn-Hite 7500) is used to generate the required voltage at the frequency necessary. This voltage is applied across the AC actuation coils (inductive coil) which in turn produce the AC magnetic field (≈4 kA/m) that excites the actuator. A neodymium disk magnet is used for providing the required DC bias (40-55 kA/m). This disk magnet is attached to an adjustable piston which can be used to adjust the distance from the actuator to optimize the DC bias magnetic field. A commercially available hydrophone (Aquarian-H3) is used for sensing acoustic signals generated by the actuator vibration. An audio preamplifier (PA-4 Hydrophone Preamplifier) is used to amplify the acoustic signal received by the hydrophone with a gain of 12 dB. The hydrophone and preamplifier convert the acoustic pressure to a voltage signal, and this signal is then collected by a data acquisition device (NI-DAQmx) and sent to a PC for processing and display. The actuator excitation and data acquisition are synchronized by programming in LabVIEW^{TM}. Details of these hardware components, along with digital signal processing, are discussed in the following sections.

Transmit coils: The transmit coils are designed and fabricated to maximize the excitation magnetic field for maximum actuator vibrations. The output impedance of the power amplifier is 200 Ω, and for obtaining the highest magnetic field intensity, the impedance of the coil is matched to this value. The optimized number of turns for maximizing the output is found to be 220. So, the actuation coil is fabricated by winding 220 turns (motor winding wire, 28 AWG) on a PVC pipe with a 24 mm radius.

Signal generator and the amplifier: The signal generator and the power amplifier are used to generate the sinusoidal voltage across the transmit voltage. The sine signal generated by the signal generated is amplified by the power amplifier for increasing the excitation field.

Hydrophone, audio preamplifier and data acquisition device: The hydrophone and preamplifier are used in the actuator signal detection for sensing the acoustic signals generated by the vibrating actuator and then convert to voltage signals. The data acquisition device then records these voltage signals for process and display. The hydrophone is sensitive to acoustic pressure generated by the movement of the actuator, transmitted through the intervening tissue and fluids. The hydrophone is specified as having a sensitivity of -192 dB re: 1 V/µPa. For reducing acoustic attenuation at tissue/air interfaces, the hydrophone is custom-packaged in ultrasound gel, as shown in Fig. 2.7. The hydrophone is packaged inside a PVC tube filling the sensor area in ultrasound gel. A thin, one-side-cementable 60 µm FEP film is used to close the side that is facing the actuator. The thin film will ensure low attenuation at this boundary. Finally, the voltage signals amplified by the audio preamplifier is recorded to a PC using a data acquisition device.

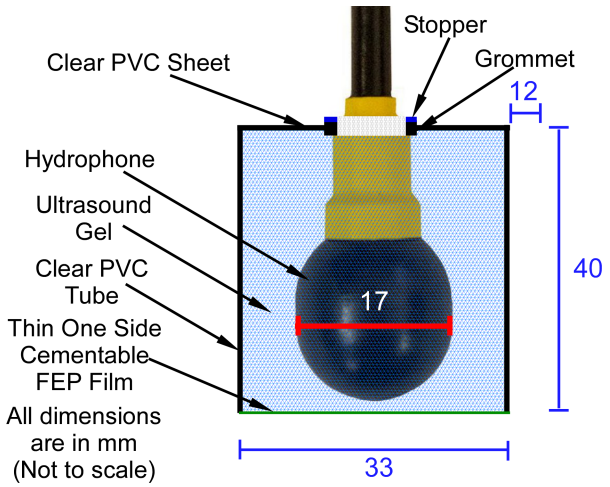

Fig. 2.7: Custom packaged hydrophone for minimizing acoustic attenuation.

Digital signal processing: Although the acoustic signal received by the hydrophone is amplified using the preamplifier, the signal is still noisy. As such, a series of digital signal processing techniques are implemented to improve the SNR and thus the wireless range. The flow diagram of the signal processing steps in LabVIEW is shown in Fig. 2.8.

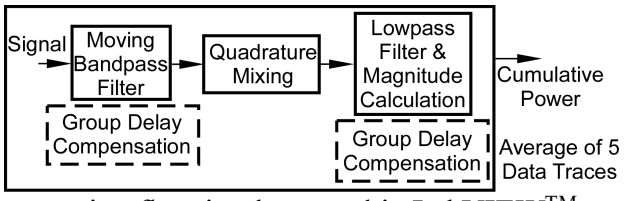

Fig. 2.8: Digital signal processing flow implemented in LabVIEW™.

The acquired signal is first filtered using a moving bandpass filter to remove the higher and lower frequency noise. This filter is a narrow bandpass filter centered at the actuation frequency, which is swept. The filtered signal is then quadrature mixed to isolate the essential frequency component. The magnitude calculation and the low pass filter are then used to extract the envelope of the amplitude of the signal. The signal amplitude is integrated over time to leverage the full signal response energy. The measured E (cumulative power) is defined as:

$$E = \sum_{n=0}^{1000} {x_n}^2 \tag{2.1}$$

where x_n is the amplitude of the signal at sample n after digital signal processing. The reference signal in these plots is the signal measured when the actuator was absent. The actuation frequency is swept while monitoring the acoustic response, which is expected to peak at resonance frequencies of the actuator. All these processes are programmed using a LabVIEW code.

2.5 Benchtop Experiments

Several benchtop experiments were conducted in order to evaluate the performance of the interrogation module developed as well as to investigate the challenges related to integrating the actuator onto the valve and corrosion protection. Previously, the actuator response was detected

while mounted on a metal plate [Pep15b]. So, experiments were conducted to see if the actuator response attenuates when mounted onto a valve-like substrate. The AGV is implanted inside the eye above the scleral tissue but under the conjunctiva layer. So, experiments were conducted to see if the actuator signal attenuates in the presence of the conjunctiva layer. Finally, experiments were performed involving corrosion protection techniques using an aluminum oxide coating. These experiments are detailed in the following sections.

PDMS Mold Experiments: Previous experiments were conducted mounting the actuator onto metal plates. So, initial investigations were focused on making sure the actuator behaves similarly when mounting to a real AGV instead of metal plates. An AGV is made of silicone rubber. Hence a similar material, Polydimethylsiloxane (PDMS), was chosen to mimic the properties. A PDMS mount with similar curvature to that of the real valve is fabricated. For this, the annealing plates that were used for curving the actuator are used as the mold. These plates were cleaned with acetone, isopropyl alcohol, and DI water. PDMS (Dow Corning Sylgard 184) was prepared at 10:1 ratio and filled in the mold, as shown in Fig 2.9 (left). Scotch tape was placed around the open edges of the metal plates to keep the PDMS inside the mold. PDMS was then cured at 120ºC for 30 minutes. Annealing plates were separated (peeled off) using a tweezer. The fabricated PDMS mount is shown in Fig. 2.9 (right).

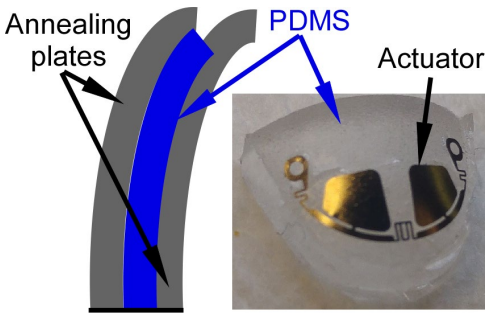

Fig. 2.9: Schematic of mold created using annealing plates filled with PDMS, and photograph of the resulting PDMS substrate with the mounted actuator.

The thickness of this mold was measured and found to be 1.56 mm. (A typical valve thickness varies between 1.1 mm to 1.84 mm.) A Type I actuator was mounted onto this, as shown in Fig. 2.9 (right). The frequency response from the experiments is illustrated in Fig. 2.10. The DC bias (30 G) in this experiment was applied using Helmholtz coils instead of a permanent magnet.

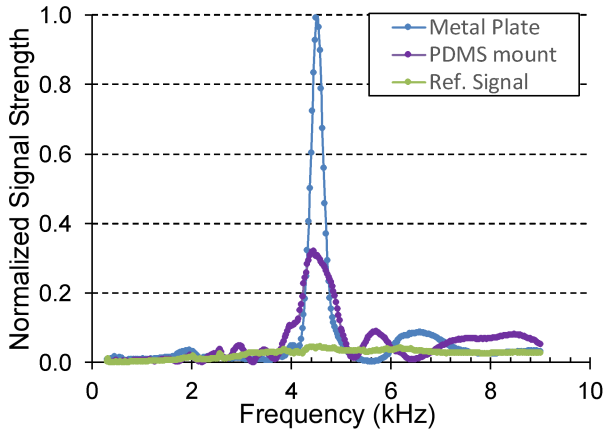

Fig. 2.10: Frequency response while the actuator is mounted onto a metal plate and onto the PDMS mount. "Ref. signal" is the signal when no actuator is present (i.e., background noise).

The signal strength is reduced to 30% in the case of PDMS substrate used instead of an actuator mounted on a metal plate. This is attributed to the change in acoustic impedance due to the difference in the mounting substrate. However, the functionality of the actuator could be verified with an SNR of ≈28.

Conjunctiva simulant experiments: In the intended application, the actuator integrated valve is implanted above the sclera and under the conjunctiva layer. In the next step, tests were conducted to see if the presence of a conjunctiva simulant affects the actuator response. The conjunctiva simulant (contact lens), is placed over the actuator, as shown in Fig. 2.11 (top). The actuator was mounted on a metal plate for this experiment. Type I and Type II actuators were used

for these experiments. The DC bias applied was 47 G for Type I and 40 G for Type II. The frequency response in these cases is shown in Fig. 2.11.

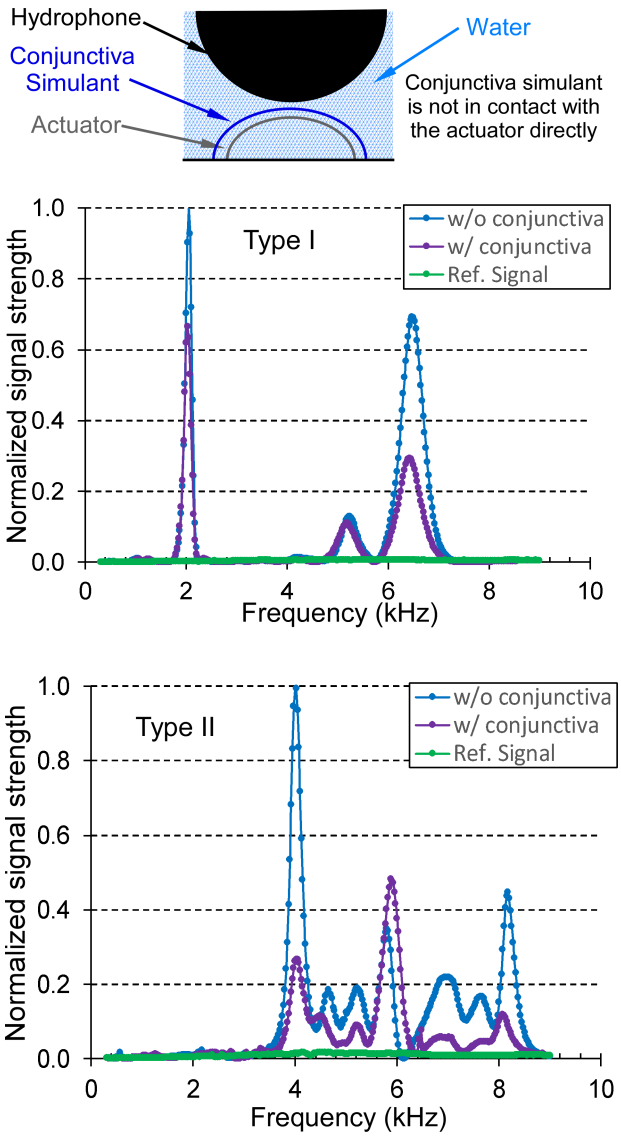

Fig. 2.11: : Schematic showing placement of conjunctiva simulant over the actuator (Top). Frequency response from the actuators in cases with and without conjunctiva simulant. Type I, Type II (right). The traces labeled "w/o conjunctiva" are signals without the contact lens. The traces labeled "w/ conjunctiva" are signals with the conjunctiva simulant. "Ref. signal" is the signal when no actuator is present (i.e. background noise).

The signal strength in various cases is reduced by ≈50% -80% for both the actuators while the conjunctiva simulant is present. However, the signal strength was sufficient, with an SNR ≈12, to confirm that the actuator is functional.

Corrosion prevention experiments: The actuator will be in a liquid medium – aqueous humor and other biological fluids – after implantation. Thus, there is a possibility of corrosion/rusting of the actuator after implantation. Experiments were conducted to assess the prevention of corrosion by coating with aluminum oxide. The thickness of aluminum oxide must be determined. Two samples were coated, one with a 10 nm thick layer and the other with a 100 nm thick layer. The actuator with 10 nm thick coating was immersed in DI water while the one with 100 nm thick coating was immersed in brine solution (prepared with dissolving 0.37 g of calcium chloride and 0.37 g of sodium chloride (2%) in 17.36 g of water). Rusting was observed in the case of the actuator which was placed in DI water after one week. Also, the actuator did not produce any measurable signal while interrogated. A photograph of the actuator and the schematic showing the rusted area are shown in Fig. 2.12.

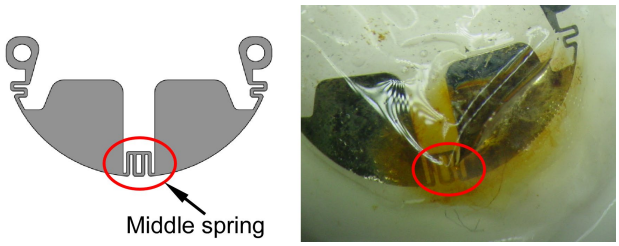

Fig. 2.12: Visuals of the rusted actuator, highlighting the middle spring where the rusting is suspected to have started.

For the actuator with 100 nm alumina coating and immersed in brine, some rusting was observed after 20 days, but the actuator still provided a good signal. A photograph of the actuator is shown in Fig. 2.13 (inset). The frequency response before and after rusting is shown in Fig. 2.13. Although

the signal is reduced by 40%, it is concluded that 100 nm aluminum oxide coating is sufficient to keep the actuator from extreme rusting and to maintain functionality.

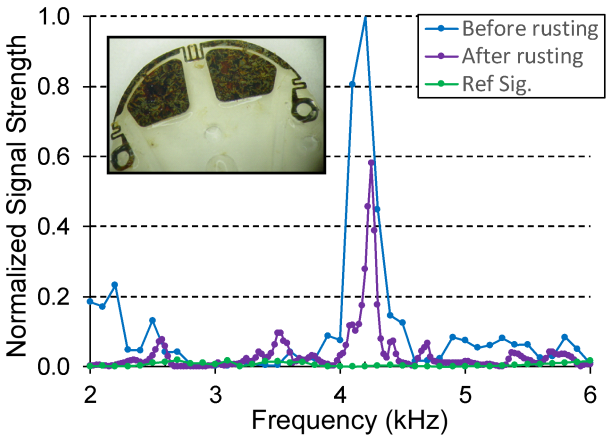

Fig. 2.13: Frequency response from the actuator before and after rusting. "Ref. Sig." is the signal when the actuator is absent. Rusted actuator after immersing in brine for 20 days (inset).

2.6 *In vitro* Experiments

In vitro experiments were conducted to demonstrate the magnetoelastic system and evaluate the performance of the interrogation module developed in this work. These experiments were conducted by immersing the actuator integrated AGVs in water, as shown in Fig. 2.14.

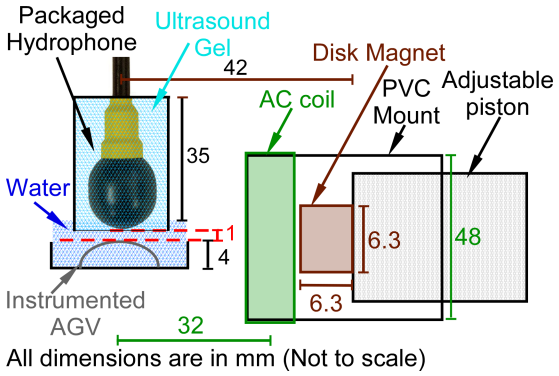

Fig. 2.14: Schematic of the in vitro experimental setup.

The actuator integrated AGV was immersed in water while the custom-packaged hydrophone was

positioned close (≈1 mm) to the actuator. The front surface of the package was submerged in water so that there was no intervening air in the path of the acoustic signal generated by the actuator. The excitation coil (AC coil) was ≈32 mm away from the actuator, and the neodymium disk magnet was positioned ≈42 mm away from the actuator. The frequency responses measured using this setup are shown in Fig. 2.15.

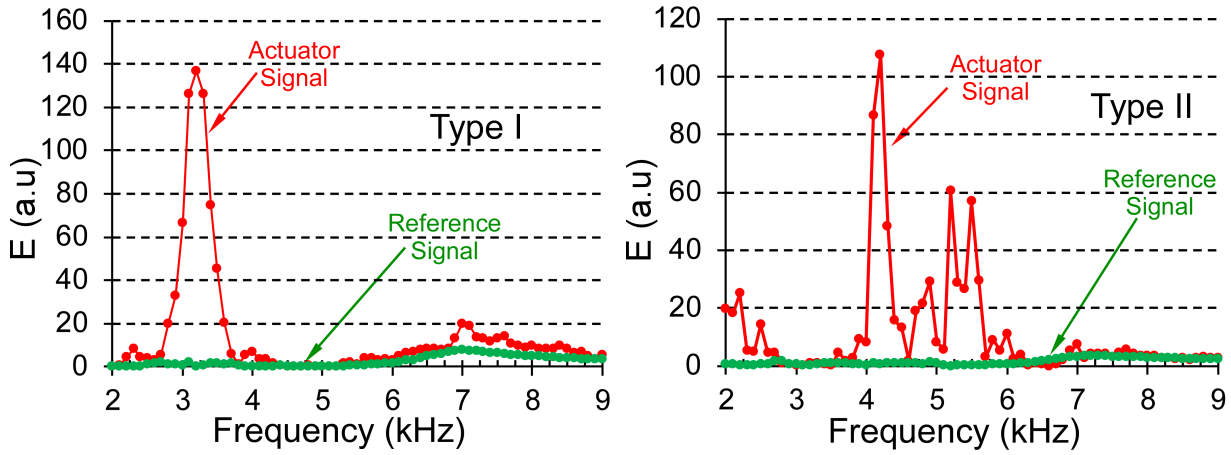

Fig. 2.15: In vitro frequency response of the actuators. Type I (left); Type II (right). The reference signal in these plots is the signal measured when the actuator was absent.

The resonant frequency of the Type I actuator was found to be ≈3.2 kHz while that of Type II was ≈4.2 kHz. The signal strength in terms of summed squared signal amplitude was ≈140 for Type I while that of Type II was ≈110. The maximum pressure amplitude *in vitro* estimated using experimental results is ≈140 Pa. The generated acoustic pressure can be estimated assuming the actuator to be a circular piston [Pie89]:

$$p(z) = \rho_0 c v (e^{jkz} - e^{jkr}) \tag{2.2}$$

where acoustic propagation: p is the pressure generated by vibrating circular piston, z is the distance from the piston (0 m for calculating maximum pressure), c is the velocity of sound in water (1500 m/s), ρ_0 is the density of water (1000 kg/m^3), v is the maximum velocity of the actuator

surface (150 μm/s), k is the propagation constant ($2\pi f/c$), f is the vibration frequency, and r is the distance from the edge of the piston to z (5 mm). With a vibration frequency of 4 kHz and the values listed above, Eq. (2.2) estimates a maximum acoustic pressure of 225 Pa. This agrees with the estimated experimental value of ≈140 Pa. Successful verification of actuation indicated that the system is ready to test *in situ.*

2.7 *In situ* experiments

The *in situ* experiments were conducted to demonstrate the functionality of the system in an implanted environment. These experiments investigated to evaluate the factors like the presence of tissue in an implanted environment that could affect the performance of the system. These tests used eyes that were harvested from deceased porcine specimens. The size and shape of a porcine eye are similar to that of a human eye, and also the conjunctiva and scleral tissue are similar in composition to that of a human eye.

The surgical procedure for the implantation was as follows. Using Westcott scissors and forceps, a conjunctival incision was made at the limbus. Blunt dissection was carried out to separate the overlying conjunctiva from the underlying sclera. The AGV was primed using a balanced salt solution. Using a Nugent forceps, the AGV was positioned between the conjunctiva and sclera and sutured to the sclera 8 mm posterior to the limbus using 7-0 polyglactin suture. The tube of the implant was trimmed and inserted through a sclerotomy into the anterior chamber of the eye. The tube was secured to the globe using a 9-0 nylon suture. A paracentesis was created to reflate the chamber during the testing. The overlying conjunctival tissue was reapproximated using an 8-0 polyglactin suture. After the AGV was attached to the globe, the fluid flowed through the tube forming a reservoir around the device. Visuals of the implantation in progress and the actuator under the conjunctiva layer are shown in Fig. 2.16.

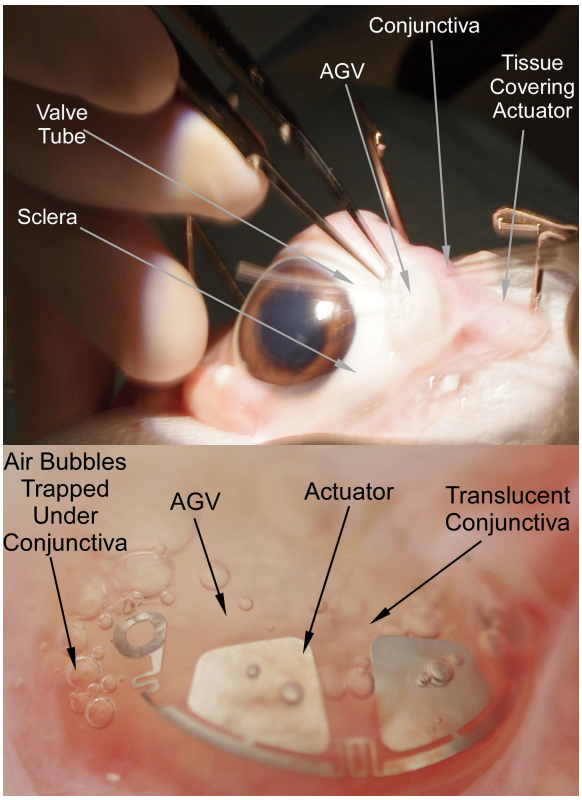

Fig. 2.16: AGV implantation in progress (Top). Implanted actuator and valve covered by conjunctiva (bottom).

The Type I actuator was measured with the conjunctiva layer in place (Fig. 2.16 (bottom)). For expediency, the Type II actuator was measured with connective tissue draped over the valve. Fig. 2.17 shows typical measurements from the implanted actuators using the interrogation module.

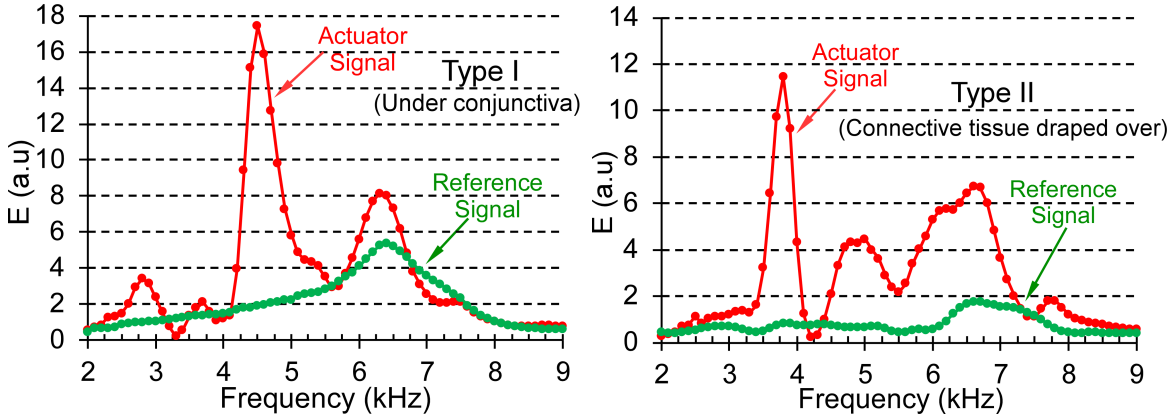

Fig. 2.17: Post-implantation frequency response of the actuators. Type I (left); Type II (right). The reference signal in these plots is the signal measured using the interrogation module on an eye which is not implanted with the instrumented AGV.

The resonant frequency of Type I is 4.5 kHz, and Type II is 3.8 kHz; the SNR is 3 to 6 with a quality factor of ≈10. Compared to the *in vitro* response of the actuators shown in Fig. 2.15, the signal from the actuator after implantation is attenuated as well as shifted. The resonant frequency of Type I is shifted by ≈1.4 kHz while that of Type II is shifted by ≈600 Hz. The summed square signal amplitude dropped by ≈120 a.u in the case of Type I and ≈96 a.u. in the case of Type II. Successful signal detection from the actuator indicates that the actuator is functional after implantation. These acoustic signals measured are first acoustic signatures measured from an implanted magnetoelastic device.

2.8 *In vivo* experiments

In vivo experiments were conducted to demonstrate the functionality of the magnetoelastic system in a live animal. Successful *in vivo* experiments will indicate the readiness of the system for clinical trials in the future. The *in situ* experiments indicated that the frequency shift after implantation is not significant, a simple patient-friendly interrogation module consisting of only the actuation module without feedback is developed for the *in vivo* experiments. Also, having an interrogation module in a closed loop with hydrophone sensing and multiple hardware components is difficult to be implemented in an *in vivo* scenario. As such, the interrogation module was simplified to just an actuation module without measurement of response or feedback. First, the development of this simplified actuation module is detailed, followed by the *in vivo* experiments performed with it.

Simplified actuation module: As described before the interrogation module is simplified to an actuation module for *in vivo* experiments. This module is developed focusing on the clinical utility to easily implement on a live subject by clinicians under minimal instructions. In this

module, the actuator is subjected to a wide range of frequencies which include the resonant frequency of the actuator. Using a range of frequencies, in the form of a slowly swept signal, ensures that the actuator will be excited even if its resonant frequency is shifted after implantation. The schematic of the simplified actuation module is shown in Fig. 2.18.

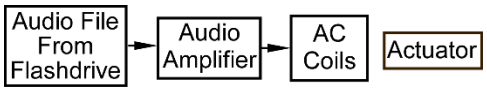

Fig. 2.18: Schematic of a simplified actuation module for in vivo experiments.

This module consists of an audio amplifier that can generate sinusoid voltage signals across inductive coils which in turn will generate the excitation magnetic field. The audio amplifier is controlled by an audio file that contains an audio signal with the frequency of from 2 kHz to 8 kHz since the resonant frequency of actuators is, in general, in this range. A chirp .mp3 file from 2 kHz to 8 kHz was made using Audacity™, and this chirp has 0.2 amplitude at 2 kHz, and this increases linearly with frequency and finally has amplitude 1 at 8 kHz. This linear variation of amplitude with frequency ensures that the current through the coil (and thus the excitation magnetic field) is kept similar for all the frequencies in this frequency range. The sweep takes 30 seconds to complete and can be repeated for more extended excitation sessions. The audio amplifier (Pyle Home PT270AIU 300-Watt) is used to convert this audio file into corresponding voltage signals. This amplifier has four terminals with the specified ideal load impedance of 8 Ω for each. It was experimentally found that ~55 turns coil results in the impedance of 8 Ω in this frequency range. For maximizing the magnetic excitation, four coils are connected to the four terminals of the amplifier, with all coils wound coaxially to superpose the field generated by each.

Considering the clinical utility of the system, it is desirable to have the coil fabricated onto a wand-like structure with handle and with a provision for adjusting the DC bias in order to have

ease of implementation in live animal tests. So, a wand-like structure was modeled and fabricated with a 3D printer (Dimension Elite) out of acrylonitrile butadiene styrene (ABS) plastic. The 3D model of the coil/magnet wand structure is shown in Fig. 2.19.

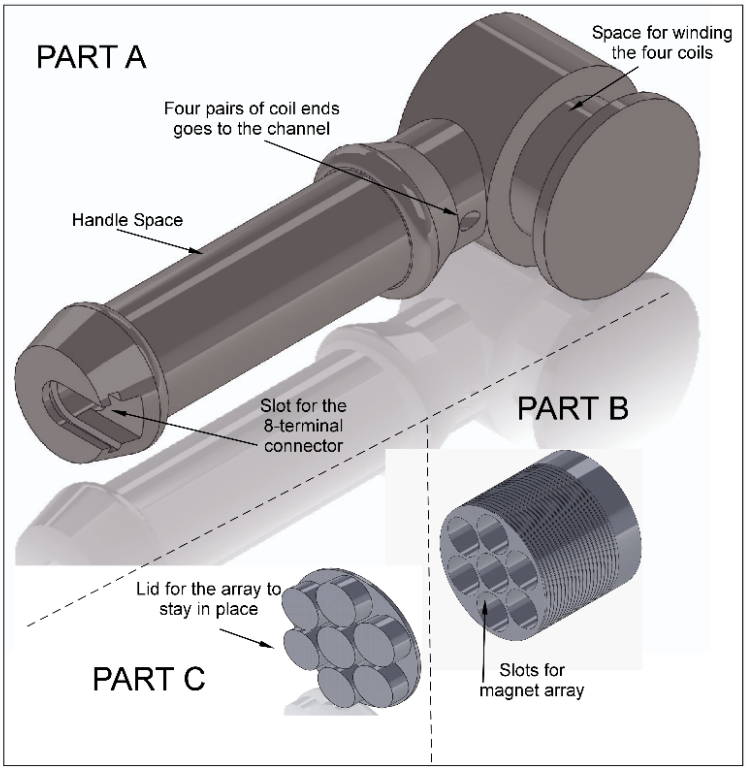

Fig. 2.19: 3D model of the different parts of the coil/magnet wand.

The coil/magnet wand has three parts. Part A consists of the basic structure with a specific slot for winding the AC actuation coils and a handle to hold during *in vivo* experiments. Part A also has a through-hole channel to route out the terminals of the four AC coils to an eight-terminal connector. Part B is where the array of neodymium magnets is placed for providing the required DC bias. Part B is attached to part A via the thread system so that the distance of this magnet array from the actuator can be adjusted in order to change the DC bias as necessary for different implantation depths. Finally, part C is acting as a lid to the part B assembly to keep the array of magnets in place. Detailed illustration and the dimensions of part A are shown in Fig 2.20.

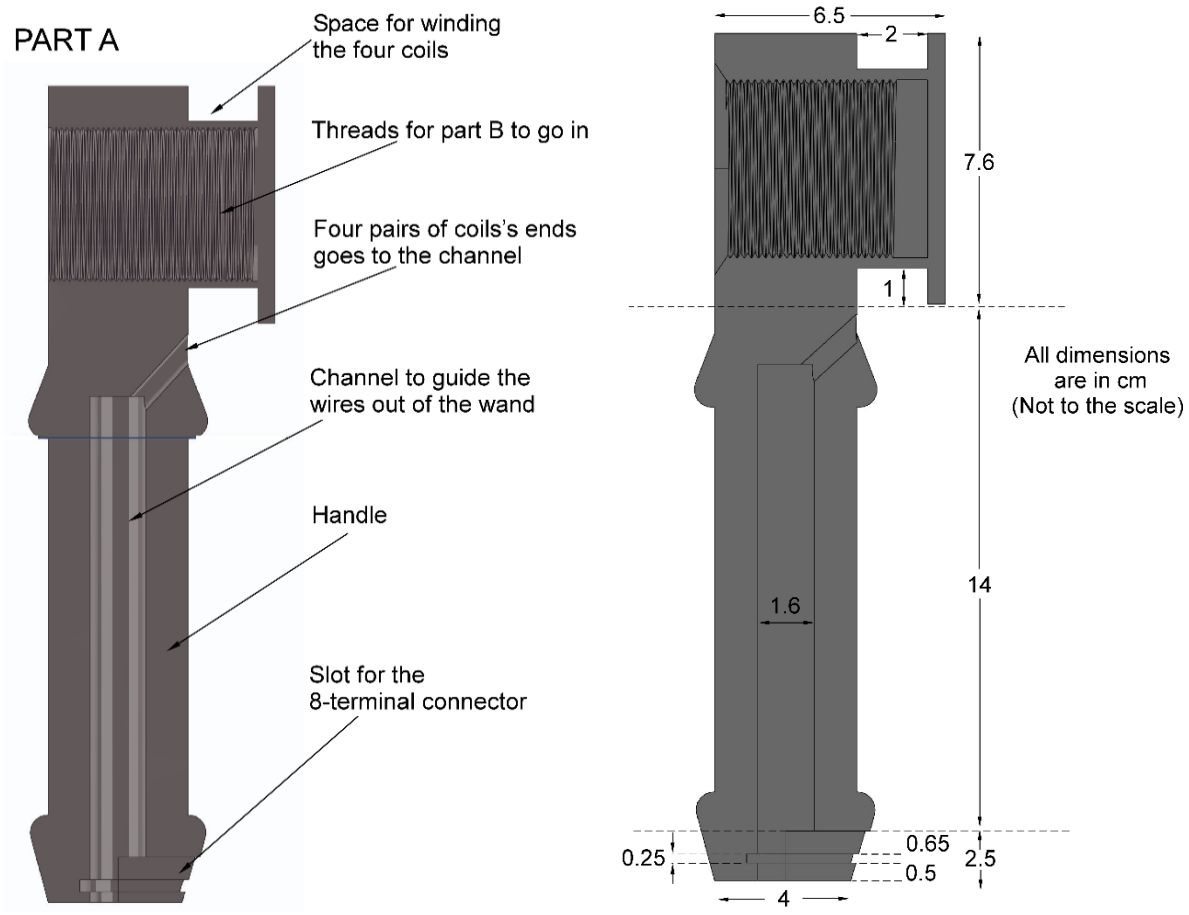

Fig. 2.20: Detailed description of part A of the wand and the dimensions.

The four 50 turns coils (56 mm diameter, 20 mm length) were wound, co-axial, each wrapped in consecutive layers as uniformly as possible in the specified slot in the part A of the coil/magnet wand. The array of disk magnets were also inserted in the corresponding slots with the help of part B and part C.

In vivo experiments: *In vivo* experiments were conducted on live rabbits (New Zealand Rabbit) using the interrogation module developed. The eye size and the composition of the eye of these rabbits are similar to that of humans and hence chosen as subjects for live animal tests. *In vivo* experiments consist of the surgical procedure for implantation of the actuator integrated AGV,

the actuation session with the simplified actuation module and finally the postmortem of the subjects. These steps are detailed in the following sections.

Implantation surgery: The actuator integrated valves were implanted by Dr. Ying Han and Dr. Behzad Amoozgar (University of California, San Fransisco). Surgical procedures started by sanitizing the actuators by spraying with isopropyl alcohol (IPA) and exposing them to ultraviolet (UV) radiation. Epinephrine was injected into the subjects 30 mins before surgical procedures. The intraocular pressure was measured using Tonovet (Icare). The animals were premedicated with subcutaneous injection of buprenorphine by the veterinary staff to provide pre-emptive analgesia. An injectable combination of ketamine and xylazine were administered intramuscularly; then mask anesthesia delivery of isoflurane was applied initially to get the rabbits sufficiently anesthetized, as indicated by lack of muscle tone and loss of gag reflex; the endotracheal tube was then placed by the veterinary staff using standard insertion technique. In order to maintain normovolemia, an intravenous catheter was placed in the rabbit's marginal ear vein to deliver intravenous fluids during anesthesia. After adequate anesthesia was achieved, the right eye of each rabbit was prepared with povidone-iodine. A lid speculum was placed. A 9-0 Vicryl suture was passed through the superotemporal limbus to rotate the eye downward. Conjunctival peritomy was performed at the limbus in the superotemporal quadrant, followed by posterior dissection in the same plane. The actuator integrated valve was placed via micro-forceps on the episcleral surface approximately 6 mm from the limbus. A paracentesis was created via a supersharp blade. Viscoelastic was injected into the anterior chamber. The 23G needle was used to create an entry at 2 mm from the limbus into the anterior chamber. The tube of the AGV was inserted into the anterior chamber via the same track. The tube was handled with care in order to not make contact with the cornea and thus minimize irritation. The conjunctiva was closed to the

limbus with interrupted 8-0 vicryl sutures. At the end of the surgeries, 150 µL of cefazolin was injected subconjunctivally for antimicrobial prophylaxis. The catheter was removed, and hemostasis was achieved by direct pressure over the insertion site. Post-operative treatments were included antibiotics with predforte for the first five days, three times per day (including surgery day). During the second five days predforte was used only twice daily, and in the third five days predforte was used once daily. The visual of the surgery in progress is shown in Fig. 2.21.

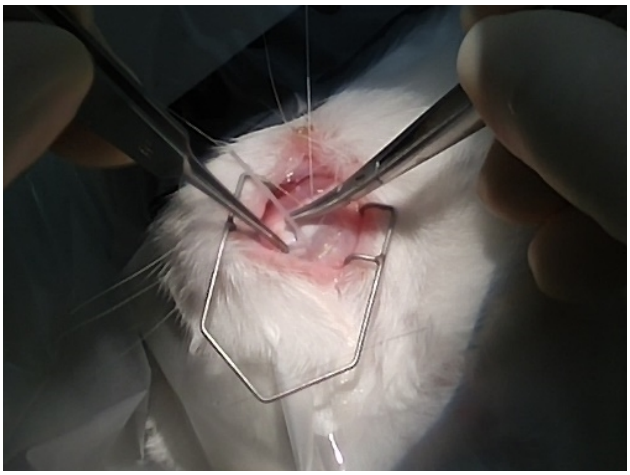

Fig. 2.21: Implantation of magnetoelastic actuator integrated AGV in rabbit T1438. Surgery in progress.

Actuation Sessions: Actuation sessions were carried using the simplified actuation module to excite the implanted actuator. Actuation was done only for the experimental subject (subject I, rabbit T1438). The rabbit was under isoflurane anesthesia for the duration of the actuation process. The coil/magnet wand made of inductive coils and an array of permanent magnets was brought close to the animal, against the fur of the animal, ~1.5 cm away from the implanted actuator, near the eye with the implanted valve. The visual of actuation in progress is shown in Fig. 2.22.

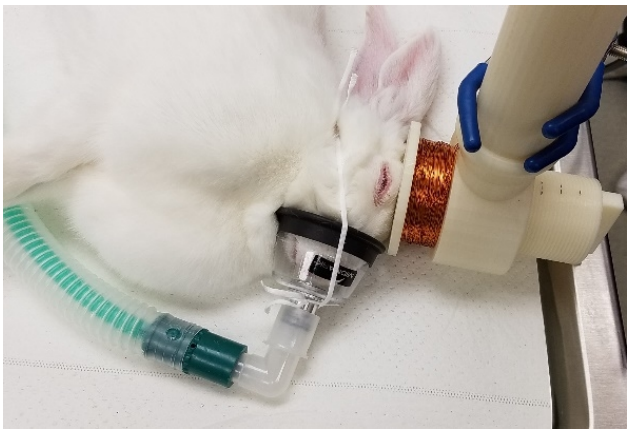

Fig. 2.22: Wireless actuation of the implanted actuator using the coil/magnet wand.

The wand was placed so that the axis of the coil on the wand is aligned to the implanted actuator integrated AGV. The distance of the magnet array from the AGV was adjusted to be ~5.5 cm. The audio file plays for 30 seconds, and then automatically repeated for voltage generation and in turn the magnetic field for exciting the actuator. To verify stable connections, the voltage at the four outputs of the amplifier was measured, while the wand was connected, using the portable oscilloscope (Picoscope). For a volume setting of 20 dB, the peak voltage was measured to be ~200 mV (at ≈7 kHz) from all the terminals and all connections were confirmed to be intact. For actuation purposes, the amplifier volume setting of 50 dB is used, and the AC magnetic field on the axis of the wand at the face of the wand was measured using an axial probe and a gaussmeter (F.W. Bell Model 5170) in AC mode. This was found to be ~10 G (800 A/m). Using these settings and based on these measurements, an estimated AC magnetic field of ~400 A/m (at a frequency swept from 2 kHz up to 8 kHz), along with a steady magnetic field of up to 4 kA/m, was generated at 1.5 cm away from the face of the wand (at the location of the actuator integrated AGV) by the coil/magnet wand. The duration of the actuation was 20 mins and was performed twice a week, for 4 weeks postoperatively. The animals were under observation in a housing facility under proper

veterinary care. There was no health illness observed on the subjects during the whole experiment until the euthanizing.

Postmortem observations: Both the rabbits were euthanized after 4 weeks, and the valves along with actuators were explanted. Explanted valves were then observed under the microscope, and there wasn't any visible sign of corrosion on the actuator. The visuals of the explanted valve are shown in Fig. 2.23. and close-up visuals of the actuator parts are shown in Fig. 2.24 and Fig. 2.25. The actuators were damages during the explanation procedure but not while implanted inside the eye. The bond between the actuator and AGV was intact before explantation, and this indicates success in the valve mounting technique introduced in this work. Photographs of the eyes of the subjects after postmortem and pre-enucleation are shown in Fig. 2.26.

Fig. 2.23: Explanted actuators from the eyes of euthanized test/control rabbits.

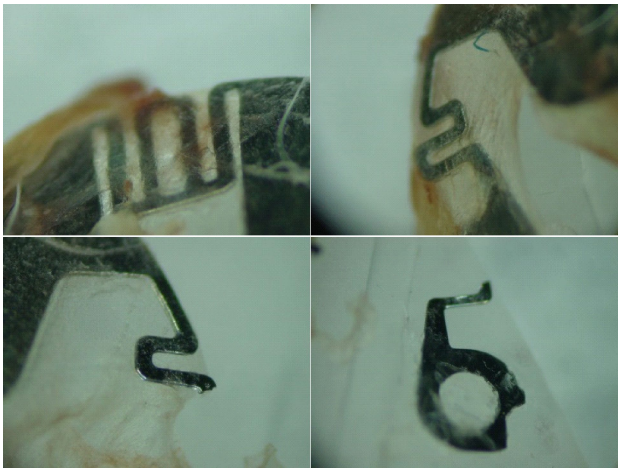

Fig. 2.24: The small parts of the actuator which was implanted inside the test rabbit. There is no clear sign of corrosion on any of these parts.

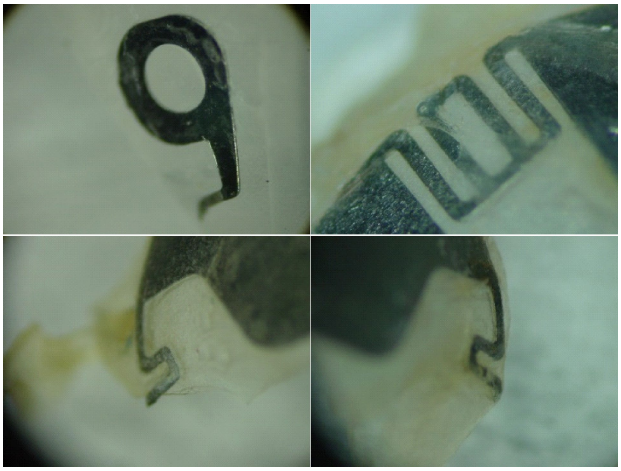

Fig. 2.25: The small parts of the actuator which was implanted inside the control rabbit. There is no clear sign of corrosion on any of these parts.

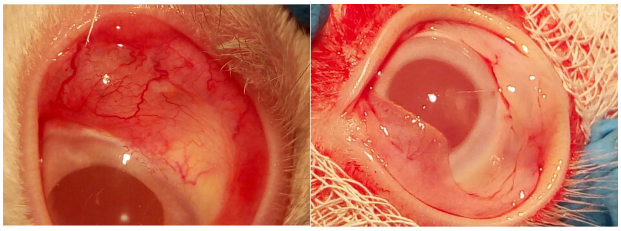

Fig. 2.26: Visuals of the actuator implanted eye of the test rabbit (left) control rabbit (right) after postmortem and pre-enucleation.

Both eyes were preserved in formaldehyde 10% for preserving the tissue for histology. Preliminary observation on the explanted actuators confirms successful corrosion protection techniques of the aluminum oxide coating.

2.9 Summary and Conclusions

In this chapter, a magnetoelastic system for glaucoma valve encapsulation mitigation is discussed, which consists of an actuator and interrogation module for interacting with the actuator. The magnetoelastic actuator was integrated onto an AGV using silicone epoxy, and the actuator was also coated with 100 nm aluminum oxide to prevent corrosion and to provide biocompatibility. Benchtop experiments were conducted to investigate these techniques followed by *in vitro* experiments. The module developed in this work improved the SNR *in vitro* by 20x compared to previous methods [Pep15b]. Further, the actuator integrated AGV was interrogated *in situ* in porcine eyes. Successful signal detection from the excited actuator confirmed that the actuator is functional after implantation inside the eye. These signals from the actuator sensed using the hydrophone are the first acoustic signature received from a magnetoelastic actuator through the tissue. The interrogation module in the feedback loop was not practical in case of *in vivo* experiments, and hence a simplified actuation module was developed minimizing the module to just only actuation without sensing actuator signal. Finally, the actuator integrated AGV was surgically implanted in live rabbit subjects. The simplified actuation module is used to excite the actuator implanted. Preliminary observations showed that the aluminum oxide coating helped in preventing the corrosion and the valve mounting technique introduced in this work is observed to be successful. Also, the *in vivo* results presented indicate that the implanted actuator does not adversely affect the health of the animal.

Chapter 3: Sensor Design and Fabrication for Biliary Stent Monitoring

3.1 Introduction

As discussed in the introduction (1.3.2), one of the significant challenges in the implanted module for biliary stent monitoring is the miniaturization of the magnetoelastic sensor. A miniaturized sensor is especially desirable for implanted applications because it simplifies the implantation procedure, reduces the impact of the implant on the biological systems, and enables applications in smaller internal organs. However, as the sensor size decreases, the signal strength decreases drastically while the resonant frequency increases. This is undesirable, as it limits interrogation at larger wireless ranges. Also, the sensor must be biased with a DC field. An efficient way to bias as well as preserve the resonant frequency at the same time while miniaturizing is to employ targeted mass loading. The sensor was also coated with a hybrid coating for corrosion protection. The schematic of the sensor is shown in Fig. 3.1.

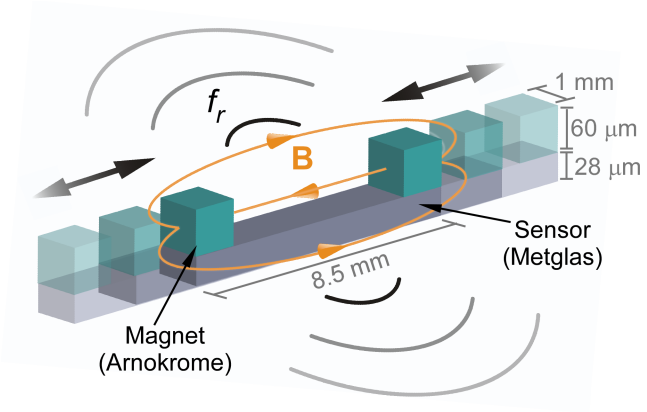

Fig. 3.1: Self-biased mass-loaded magnetoelastic sensor fabricated from Metglas and Arnokrome with Au-In transient liquid phase (TLP) bond.

This chapter discusses the design and fabrication of the sensor, followed by the benchtop and *in vitro* characterization of the sensor, specifically for the application of biliary stent monitoring.

3.2 Design and Fabrication

The sensor has two magnetic mass loads attached at the two longitudinal ends (Fig. 3.1). The sensor structure is made of Metglas™ 2826B, and the mass loads are made of Arnokrome™ 5. As discussed in the previous section, these magnetic mass loads help to preserve the resonant frequency and bias of the sensor. Assuming the longitudinal vibration of a thin uniform beam which has material density ρ, and modulus E, the wave equation is [Ros07]:

$$\frac{\partial^2 u}{\partial t^2} = \frac{1}{c^2}\frac{\partial^2 u}{\partial x^2} \tag{3.1}$$

where $= \sqrt{\frac{E}{\rho}}$, The complete solution to this wave equation is:

$$u = (A\sin\left(\frac{\omega}{c}\right)x + B\cos\left(\frac{\omega}{c}\right)x)(C\sin\omega t + D\cos\omega t) \tag{3.2}$$

For a free-free beam sensor, the strain $\partial u/\,\partial x = 0$ at $x = 0$ and $x = L_0$. The resonant frequency ω can be calculated from (3.2):

$$\omega_0 = \frac{\pi}{L_0}\sqrt{\frac{E}{\rho_s}}\ (rad/s) \tag{3.3}$$

Assuming the mass loaded sensor design to be equivalent to a point-mass load (M) beam, the boundary conditions change such that $u = 0$ at $x = 0$ and $F = SE(\partial u/\,\partial x) = -M(\partial^2 u/\,\partial t^2)$ at $x = \pm\frac{1}{2}L_1$, where S is the cross-sectional area. The resonant frequency ω_1 can be calculated from (3.2):

$$\omega_1 L_1 \sqrt{\frac{\rho_S}{E}} \cdot \tan\left(\frac{\omega_1 L_1}{2}\sqrt{\frac{\rho_S}{E}}\right) = \frac{S\rho_S L_1}{M} \tag{3.4}$$

For the resonant frequency of the mass loaded sensor and the free-free beam sensor to be equal, $\omega_1 = \omega_0$, and from (3.3) and (3.4):

$$\tan\left(\frac{\pi}{L_0}\frac{L_1}{2}\right) = \frac{L_0 S\rho_S}{\pi M} \tag{3.5}$$

For a design with a 28 μm-thick sensor with 60 μm-thick magnets mass loads, M = 0.473 mg, S =0.028 mm^2, ρ_s =7900kg/m^3; utilizing (3.5), this requires $L_0 \approx 1.46\ L_1$. This means that with the mass loads at both ends, the beam can vibrate at the same frequency of the free-free structure while only occupying 68% of the length.

The architecture was simulated in a fully-coupled magnetoelastic finite element model implemented in COMSOL [Pep15b]. The simulated coil was 5 mm in diameter and 30 mm in length, and its surface current density was 22.29 A/m (peak, directed in the azimuthal direction of the coil) to provide a 0.28 G AC peak magnetic flux density. The Metglas is only available in 28 μm-thick foils while Arnokrome is available in 60 μm-thick sheets. As such, a single layer sensor (28 μm Metglas) with single layer mass load (60 μm Arnokrome) and a double layer sensor (56 μm Metglas) with double layer mass loads (120 μm Arnokrome) were simulated. The simulation results (Fig. 3.2) indicate that the desired mode of the sensors is at the resonant frequencies of 180.95 kHz and 182.85 kHz, for a single layer mass load with single layer sensor and double layer mass load with a double layer sensor, respectively. The sensor has a small amount of out-of-plane displacement even when vibrating in its fundamental longitudinal mode due to the mass loads having a center of mass above the neutral axis of the sensor.

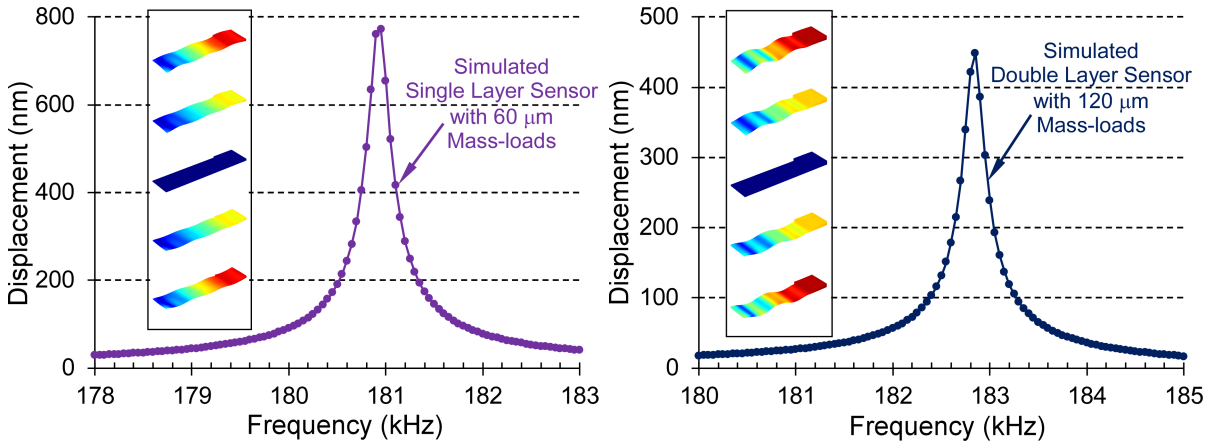

Fig. 3.2: (Left) Simulation of the single layer sensor (30 μm) with a mass-loaded thickness of 60 μm. The resonant frequency is 180.95 kHz with a maximum mass load displacement of 771 nm. (Right) Simulation of the double layer sensor (60 μm) with a mass load thickness of 120 μm. The resonant frequency is 182.85 kHz with a maximum mass load displacement of 448 nm. (Insets) Time lapse of the sensor fundamental mode; red to blue represents maximum displacement to zero displacement.

The mass loads in the sensor are intended to be permanent magnets to provide a DC magnetic field for biasing the sensor which is required for a large amplitude response from the sensor. To estimate the approximate DC magnetic flux density that could be generated in the resonator for such an architecture, finite element analysis in COMSOL was utilized. In the COMSOL simulations, the magnets have a thickness of 120 μm or 60 μm and are set to have a residual flux density of 0.9356 T (along the longitudinal axis of the resonator) and a relative permeability of 23. These are the approximate properties of the Arnokrome 5 material. The non-linear magnetization saturation behavior of the magnetoelastic material was considered in the model by setting the sensor material B-H curve to have a saturation induction of 0.88 T at 14 A/m (50000 DC relative permeability). Including this saturation behavior allows the model to avoid unrealistic shunting of the magnetic field through the highly permeable magnetoelastic material directly beneath the magnetic mass loads. The simulated magnetic flux density was found to be uniform within the active region of the sensor, as shown in Fig. 3.3. The values were 0.56 T and

0.41 T for the 60 µm-thick magnets on the 28 µm-thick sensor and 120 µm-thick magnets on the 56 µm-thick sensor, respectively. The magnetic flux density was 0.88 T (i.e., saturation) for the structure with the 120 µm-thick magnets on the 28 µm-thick sensor. This indicates that the magnet mass loads should provide sufficient DC bias to allow a significantly large sensor response. This work focuses on a 28 µm-thick sensor with 60 µm-thick magnets mass loads because of the simplified assembly process and more robust fabrication yield.

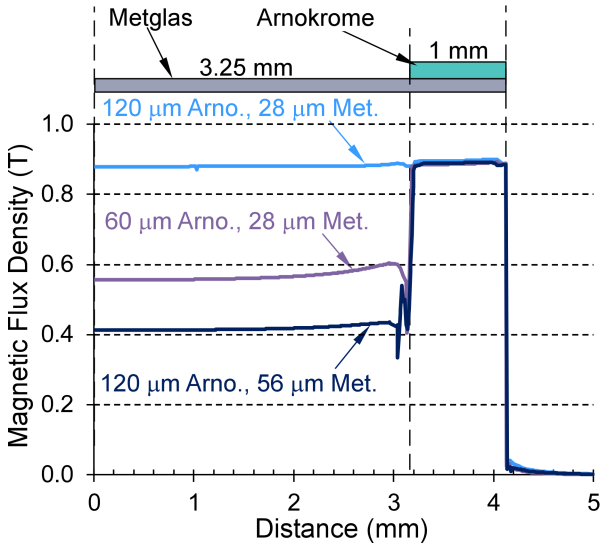

Fig. 3.3: Simulation of magnetic flux densities through Metglas for varying Metglas/Arnokrome thicknesses.

The fabrication of the mass loaded sensor is shown in Fig. 3.4. In the first step, both Metglas and Arnokrome samples were cleaned using O_2 plasma. Then, 0.1 µm Cr and 0.5 µm of Au were deposited on the Arnokrome sheet via e-beam evaporation. Then the sheets were micro-electro-discharge machined (µEDMed) to make a window in the middle. The windowed samples were then electroplated with 6 µm In. Further, 0.1 µm Cr and 0.5 µm of Au were deposited on the Metglas foils, and a transient liquid phase bond was formed between the Metglas/Arnokrome layers by applying a pressure of 1.3 MPa at 200°C for 30 mins. The bonding pressure was applied

by using custom-designed, spring-loaded C-clamps. Two 3" x 1" glass slides were used to distribute pressure along the area of the bonding materials uniformly. A heating ramp rate of 6.03°C min^{-1} and a cooling rate of 0.79°C min^{-1} ensured adequate inter-diffusion and solidification of the mixture to form the Au–In bond (Fig. 3.5). Finally, the sensors were µEDMed from the bonded layers.

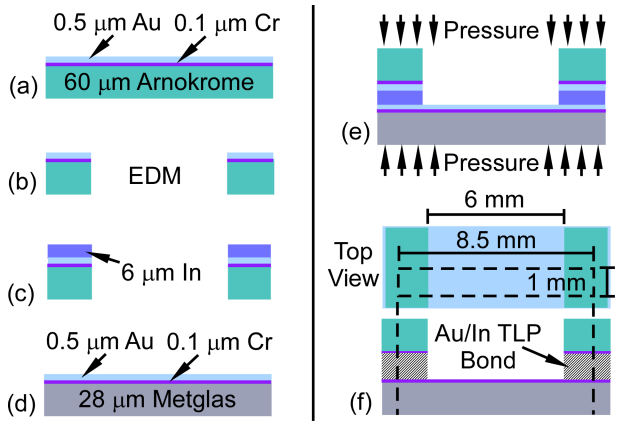

Fig. 3.4: (a) Evaporation of Cr and Au on Arnokrome. (b) Micro-electro-discharge machining (µEDM) of the window (c) Electroplating of In (d) Evaporation of Cr and Au on Metglas. (e) Transient liquid phase bond at 1 MPa and 200°C for 30 minutes in the vacuum (f) µEDM of sensors.

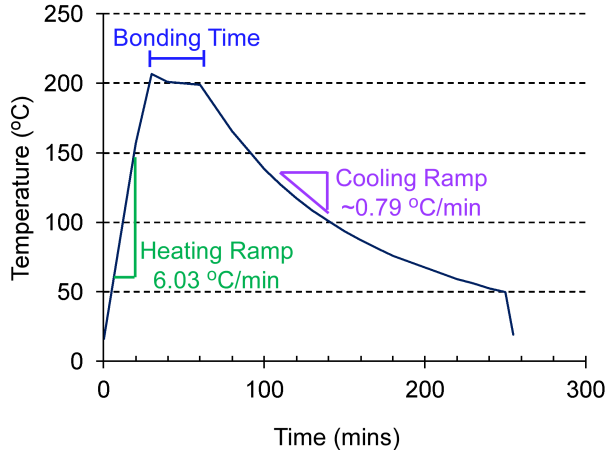

Fig. 3.5: Heating ramp and the cooling ramp for the transient liquid phase bonding process.

In the final configuration (Fig. 3.1), the sensor between the mass loads is 6.25 mm long, 1 mm wide, and 28 µm thick. The mass loads are 1 mm × 1 mm × 67.2 µm (including the Au-In

bonding layer) while the platforms underneath the mass loads are 1 mm × 1 mm × 28 μm (i.e., the total thickness at the mass loads is 95.2 μm). This results in a total sensor length of 8.5 mm. The fabricated sensor is shown in Fig. 3.6.

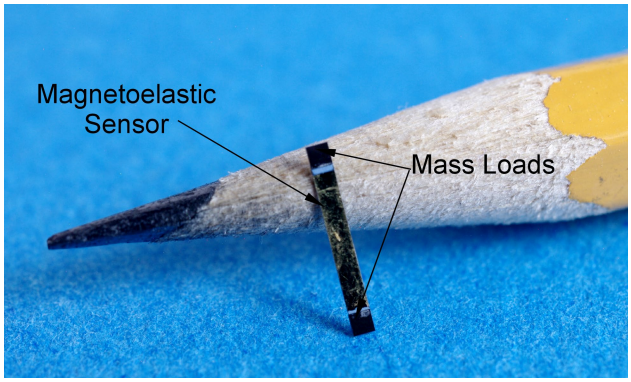

Fig. 3.6: Fabricated self-biased magnetoelastic sensor.

3.3 Experimental Results

Experiments were conducted for characterizing the sensor. First, the sensor was self-biased and compared the performance with an external DC bias. Then, the sensor was coated with a hybrid coating for corrosion protection, and the sensor performance was characterized. Finally, *in vitro*, experiments were performed to mimic occlusion and sensor performance and sensitivity were measured. The interrogation module used to characterize the sensor is shown in Fig. 3.7. The module consisted of inductive coils to excite and detect the sensor magnetically and hardware to improve the acquired signal strength. A transmit coil was used to generate the AC magnetic field for exciting the sensor, and a receive coil was used to detect the sensor signals. A function generator, in conjunction with a buffer amplifier, was used to drive current through the transmit coils. The sensor signal detected by the receive coil was amplified using a low noise amplifier and then acquired to a PC using a data acquisition device. A series of digital signal processing techniques were also used to improve the signal to noise ratio. In this work, the coils had a diameter of 3.5 cm, and the width of each coil was 2.2 cm. The transmitting and receiving coils had 10

turns each. Excitation current amplitude was kept at ≈43 mA (peak to peak) across the transmit coil. More details of the interrogation module are discussed in chapter 5.

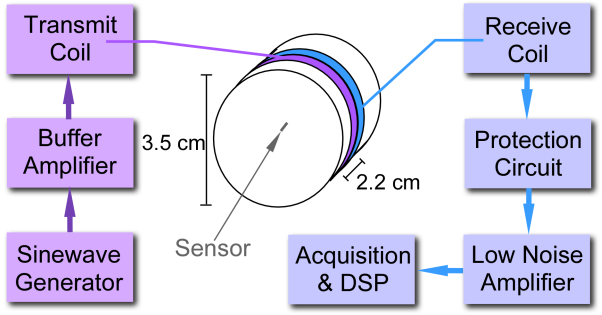

Fig. 3.7: External interrogation module used for characterizing the sensor.

a. Self-biasing

The fabricated sensor was first tested using Helmholtz coils to provide an adjustable DC bias and find the largest signal at the optimal bias point. In subsequent tests, the sensors were biased by the mass loads after magnetizing. The resonant response in each situation is shown in Fig. 3.8. When biasing with the Helmholtz coils with a 796 A/m field strength, the resonant frequency, normalized signal strength, and quality factor were 185.4 kHz, 4.4, and 412, respectively. The magnets were then magnetized using an impulse magnetizer (10 kG peak magnetic flux density). The self-biased sensor was tested and found to have a resonant frequency, normalized signal strength, and quality factor of 183.8 kHz, 3.4, and 229, respectively. Therefore, the self-biasing magnets could provide a near-optimal DC magnetic bias for the sensor.

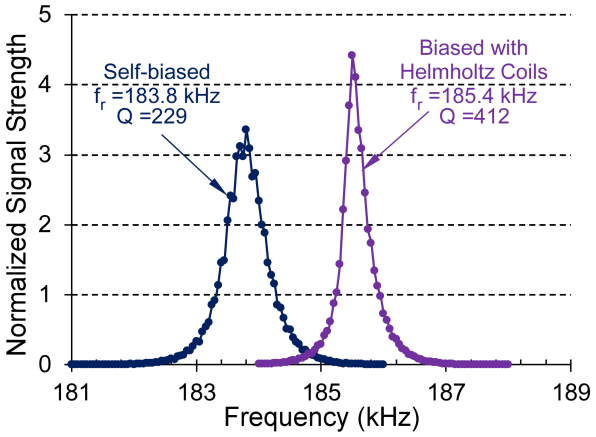

Fig. 3.8: Sensor response biased with Helmholtz coils and self-biased (magnetizing the mass loads on the sensor).

b. Corrosion Protection

The sensor must be protected from corrosion due to exposure to the environment. Especially for implanted applications, the sensor must also be biocompatible. An aluminum oxide coating can be used for these purposes [Gre09a]. The resonant response of the magnetoelastic sensor after aluminum oxide coating (100 nm) is shown in Fig. 3.8. Compared to the performance of the uncoated sensor, the sensor performance is improved after coating. The coated sensor had a resonant frequency of 185.5 kHz with a quality factor of 463 and a normalized strength of ≈19.5 while the uncoated sensor had a resonant frequency of 183.8 kHz with a quality factor of 229 and normalized strength of ≈3.5.

After aluminum oxide coating, the sensor was then immersed in reconstituted ox bile and found to have corroded within two days. The photographs of the rusted sensor are shown in Fig. 3.9.

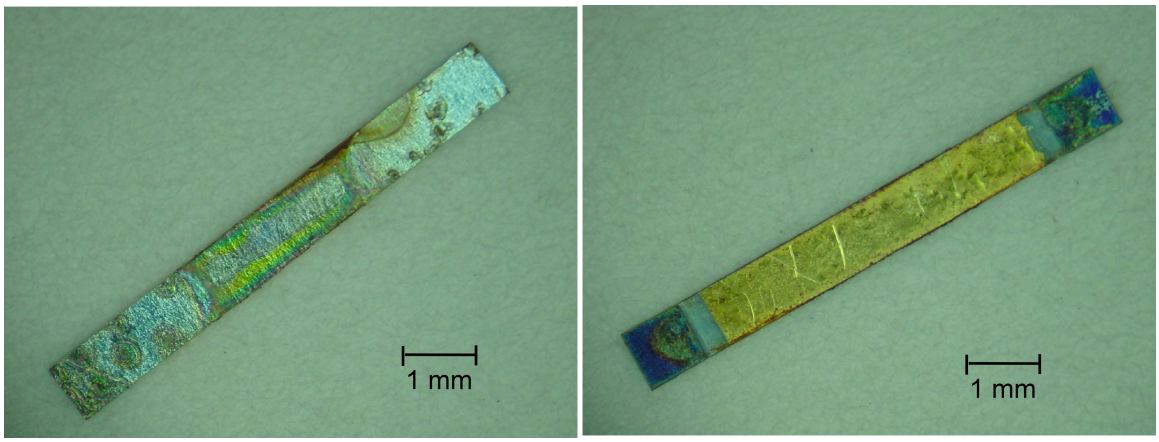

Fig. 3.9: Photographs of the rusted sensor that is only coated with aluminum oxide.

As such, an improved hybrid coating approach was investigated. Parylene is a biocompatible material and has also been used to coat sensors for corrosion protection and to ensure biocompatibility. However, Parylene coating has been found to decrease the signal strength to 20% of the uncoated signal strength after coating [Gre09b]. Thus, a hybrid coating of Aluminum oxide and Parylene is used here to provide biocompatibility and corrosion resistance while also preserving the sensor performance. The sensor response measured after the hybrid coating (Parylene 2 µm and Al_2O_3 100 nm) is shown in Fig. 3.10.

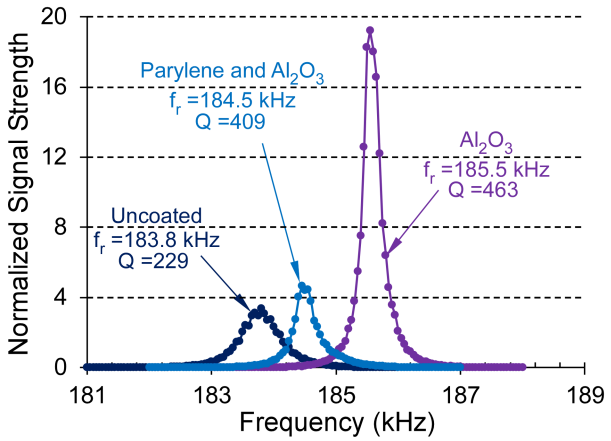

Fig. 3.10: Sensor response before and after Al_2O_3 and Parylene coating compared to the uncoated sensor.

The hybrid coated sensor has a resonant frequency of 184.5 kHz with a quality factor of 409 and a normalized strength of ≈4.5. This hybrid coating was found to protect the sensor while immersed in reconstituted ox bile for at least 7 days. The photographs of the sensor before exposure to bile and after 7 days of exposure are shown in Fig. 3.11.

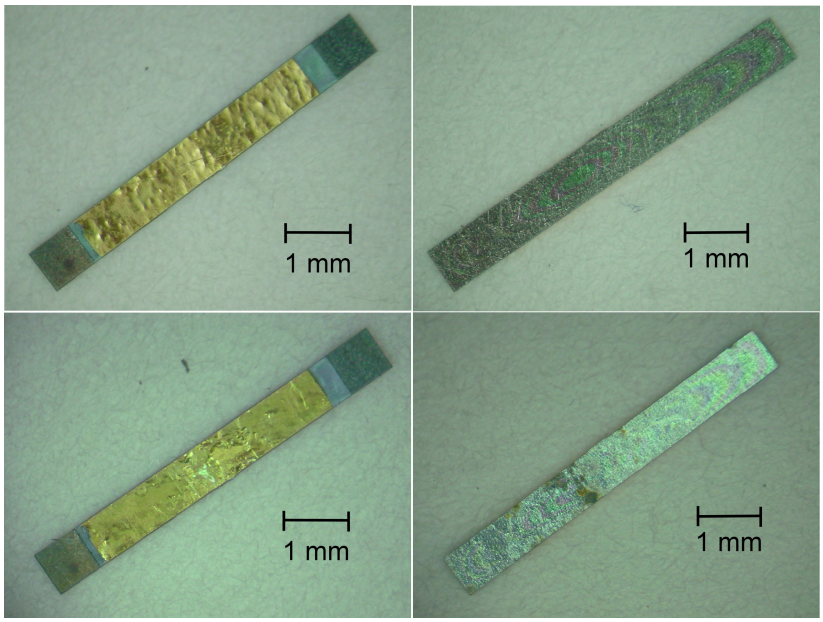

Fig. 3.11: Photographs of the hybrid-coated sensor before (above) and after (below) exposing to bile solution for seven days.

However, longer exposure to the bile deteriorated the sensor performance. The quality factor was found to be decreasing, resonant frequency shifting to lower frequencies and signal strength decreasing drastically. The sensor performance with respect to these parameters is plotted in Fig. 3.12. The sensor was not functional after exposure in bile for 250 days.

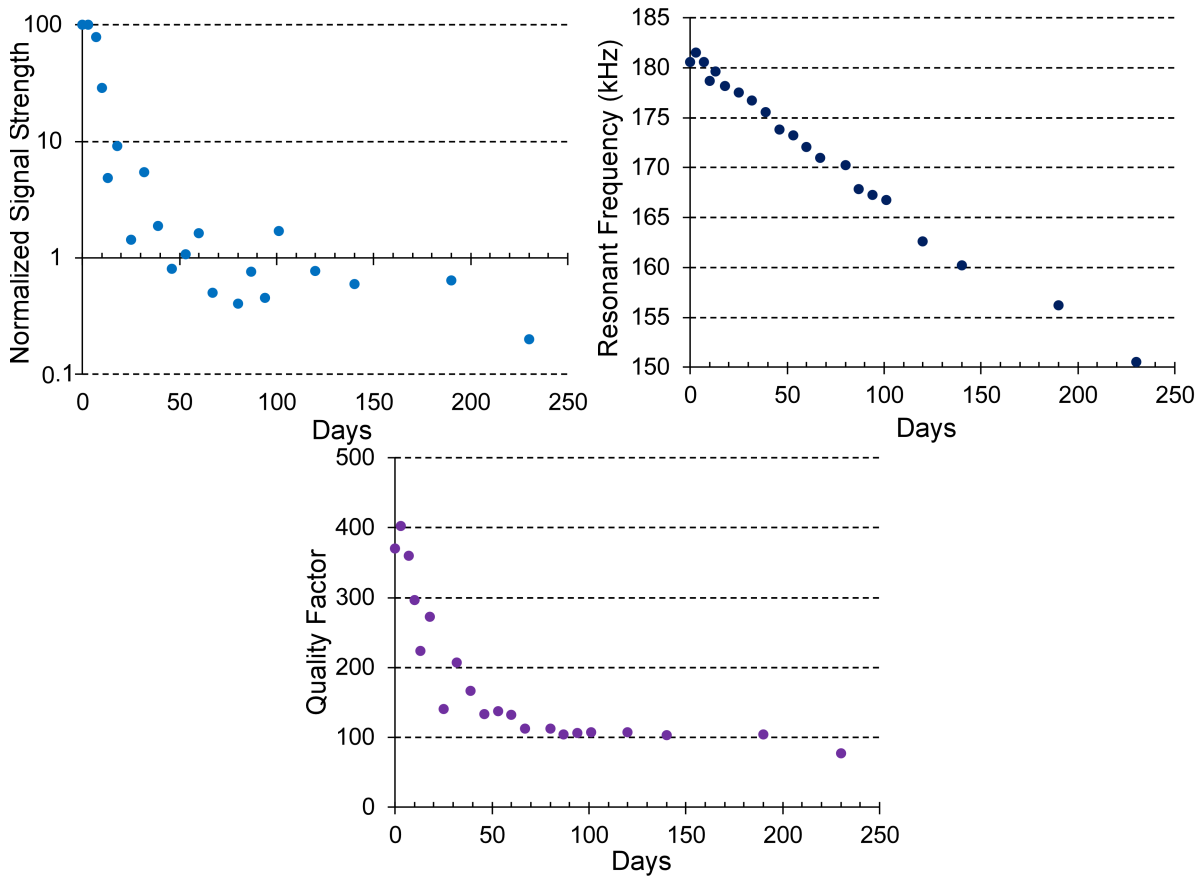

Fig. 3.12: Normalized signal strength (left top), resonant frequency (right top), and quality factor (bottom) of the sensor immersed in bile over several days.

c. In vitro Loading

In vitro experiments were performed to evaluate the sensitivity of the sensor with respect to sludge accumulation inside a plastic biliary stent. The sensor was first placed inside a stent piece (1.5 cm) and both "caged" in place and protected by a custom 3D-printed polymeric package that was stitched into the stent (this package is discussed in detail in Chapter 4). The synthetic sludge was prepared by mixing 1 g of cellulose fiber (90 µm-long, Acros Organics) and 1 g gelatin (Kroger) in 10 mL DI water. The mixture was then injected into the instrumented stent using a syringe and then allowed to cure for 20 minutes at room temperature. This cured mixture has mechanical properties similar to that of bacteria-generated sludge [Sur18]. The "partial occlusion" cases are created by mechanically partially cleaning the fully occluded instrument stent. "No

occlusion" cases were mimicked by thoroughly cleaning the instrumented stent with warm water. The method used to indirectly quantify the occlusion in a stent is to measure the flow rate of water (at 0.5" height) through the stent. By tracking the time and quantity of water collected, the flow rate was calculated. Collection time was kept constant at ≈10 seconds, but in some cases of very low flow rate, the collection time was extended to ≈30 seconds.

The instrumented stent was immersed in water while measuring the sensor response. The normalized signal strength, resonant frequency, and quality factor of the sensor were measured before the flow rate measurement for all the cases. This process was repeated for the same sensor 8 times. The results are tabulated in Table 3.1. The typical sensor responses when the stent is under full/partial/no occlusion cases are shown in Fig. 3.13. The photograph of the instrumented stent fully occluded using the synthetic sludge is shown in Fig. 3.13 inset. The sensor is buried under the synthetic sludge. The normalized signal strength, resonant frequency, and quality factor of the sensor with respect to the flow rate through the stent for all the cases are plotted in Fig. 3.14 and Fig 3.15.

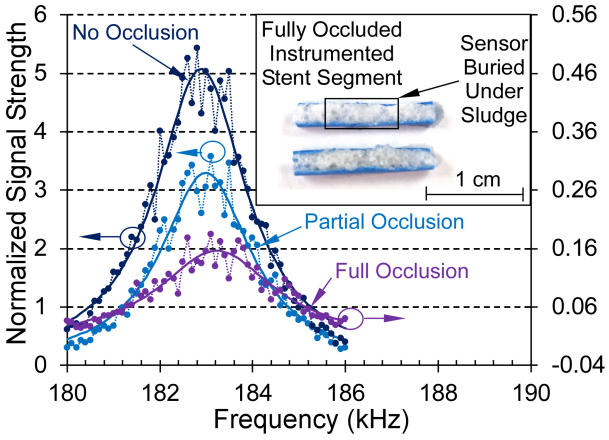

Fig. 3.13: Sensor response when the stent is with no occlusion (V =36.65 mL/min, fr =182.61 kHz, Q =94),partial occlusion (V =13.5 mL/min, f_r =182.99 kHz, Q =68), and full occlusion (V =0 mL/min, f_r=183.22 kHz, Q =50).

Table 3.1: Flow rate measurements and sensor response.

Case	Flow Rate (mL/min)	Normalized Signal Strength	Resonant Frequency	Quality Factor
Fully Occluded	0	0.135	182.74	65.08
	0	0.869	182.75	64.36
	0	0.156	182.83	60.3
	0	0.235	182.88	63.46
	0	0.878	182.9	66.02
	0	0.53	183.22	62.8
	0	0.0127	183.22	50
	0	0.025	183.23	58.3
No Occlusion	35.05	3.72	182.41	86.6
	36.65	3.8	182.61	93.55
	31.35	1.07	182.71	66.6
	31.79	1.88	182.49	66.91
	35.73	2.27	182.76	74.72
	33.46	2.32	182.35	70.18
	32.43	1.79	182.54	75.2
	33.71	1.49	182.67	75.07

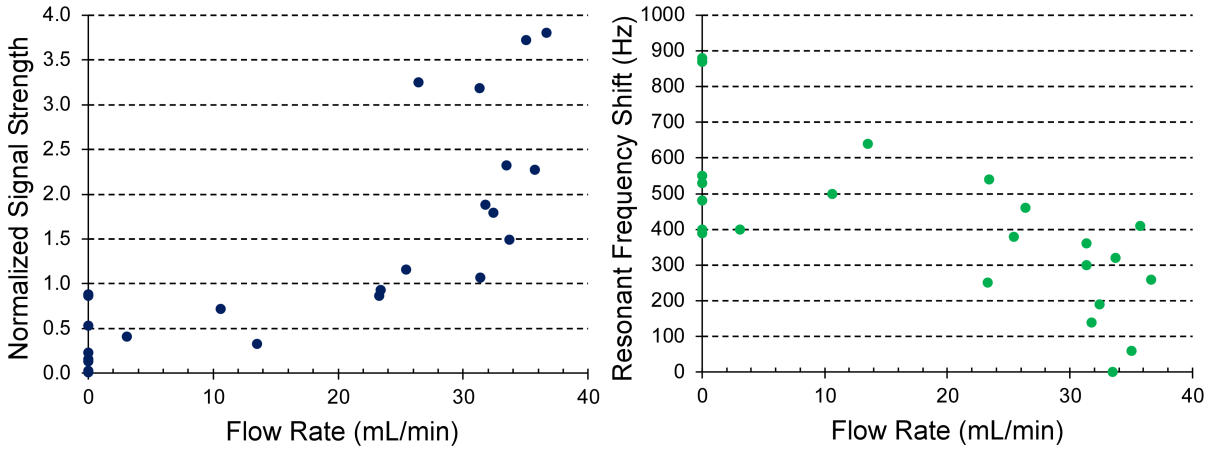

Fig. 3.14: The normalized signal strength (left) and the resonant frequency (right) of the sensor with respect to the flow rate through the stent for all measured cases.

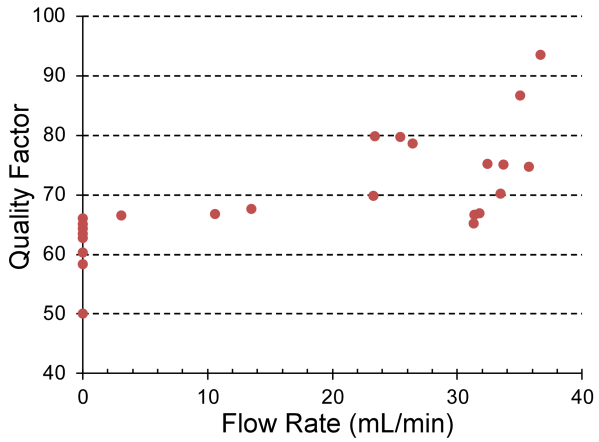

Fig. 3.15: The quality factor of the sensor with respect to the flow rate through the stent for all measured cases.

Although the signal strength shows a good correlation with the flow rate, the signal strength can also be changed by several other external factors like the position of the interrogation coils, sensor, etc. So it is not a reliable parameter to use for diagnosing occlusion. With further analysis, the ratio of the quality factor (Q) and the resonant frequency shift (Δf_r) measured in each case is found to have a reasonable correlation with the flow rate measurements. This ratio is defined as the diagnostic parameter (D_p), and it increases when the flow rate is decreased due to the occlusion in the stent. The measurements are plotted in Fig. 3.16.

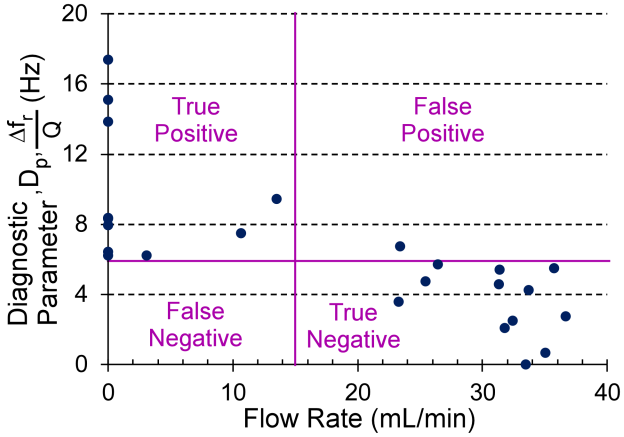

Fig. 3.16: The ratio of the resonant frequency shift to the quality factor (Diagnostic parameter (D_p)) with respect to the flow rate through the stent. A flow rate <15 mL/min is assumed to be the therapeutic threshold with the stent in need of replacement.

The fully occluded cases with flow rate 0 mL/min gave values of D_p as 5.9 Hz^{-1} to 17.4 Hz^{-1} while the zero/partial occlusion cases with flow rates >15 mL /min gave D_p as 0 Hz^{-1} to 6.7 Hz^{-1}.

The clinical performance of the sensor with respect to the diagnostic parameter defined previously can be described in terms of diagnostic accuracy. The receiver operating characteristic (ROC) provides this diagnostic accuracy mathematically [Zwe93]. This is a generally used tool for evaluating the performance of diagnostic methods in the medical field [Par04]. The ROC of the sensor was identified for detecting stent occlusion using the diagnostic parameter, D_p, assuming that occlusions resulting in a flow rate below 15 mL/min should be considered as an occluded stent and must be replaced. The True Positive Rate (TPR), is calculated by:

$$TPR = \frac{\sum True\ Positive}{\sum Condition\ Positive} \tag{3.6}$$

where $\sum Condition\ Positive$ = 11 since the total number of occluded cases is 11 (i.e. the flow rate <15 mL /min). The false positive rate is calculated by:

$$False\ Positive\ Rate = \frac{\sum False\ Positive}{\sum Condition\ Negative} \tag{3.7}$$

where $\sum Condition\ Negative$ = 13 since the total number of non-occluded cases is 13 (i.e. the flow rate >15 mL /min). The ROC curve is plotted in Fig. 3.17. The maximum TPR of 1 is achieved with a false positive rate of only 0.08 for a detection threshold of 50% decrease in flow rate (i.e. 15 mL /min) through the stent due to occlusion. The area under the ROC plot indicates the accuracy of this diagnostic parameter to be 97.84%.

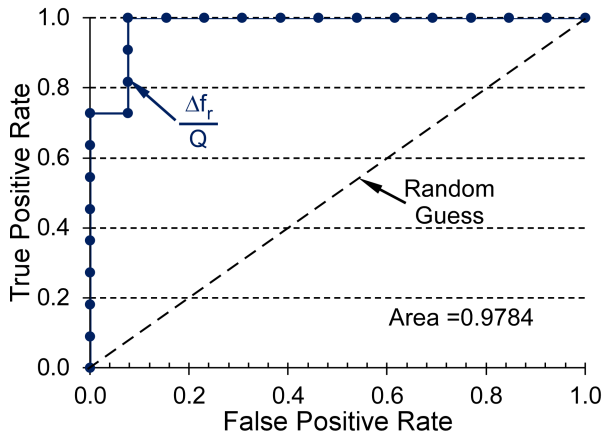

Fig. 3.17: ROC curve utilizing D_p for diagnosing occlusion in a biliary stent.

ROC curves for other parameters are also plotted in Fig. 3.18. Accuracy (given by the area under the curve) when using resonant frequency shift as the indicative parameter for occlusion is 91.55% while that when using quality factor is 95.14%. These are poorer than the previously defined diagnostic parameter which is the ratio of the resonant frequency shift to the quality factor. Note that the normalized signal strength parameter has a very robust ROC with an accuracy of 98.56%, but in a clinical situation – where the interrogation distance and thus the signal strength may vary considerably from test to test – it is not likely to be as useful as the other amplitude-independent parameters.

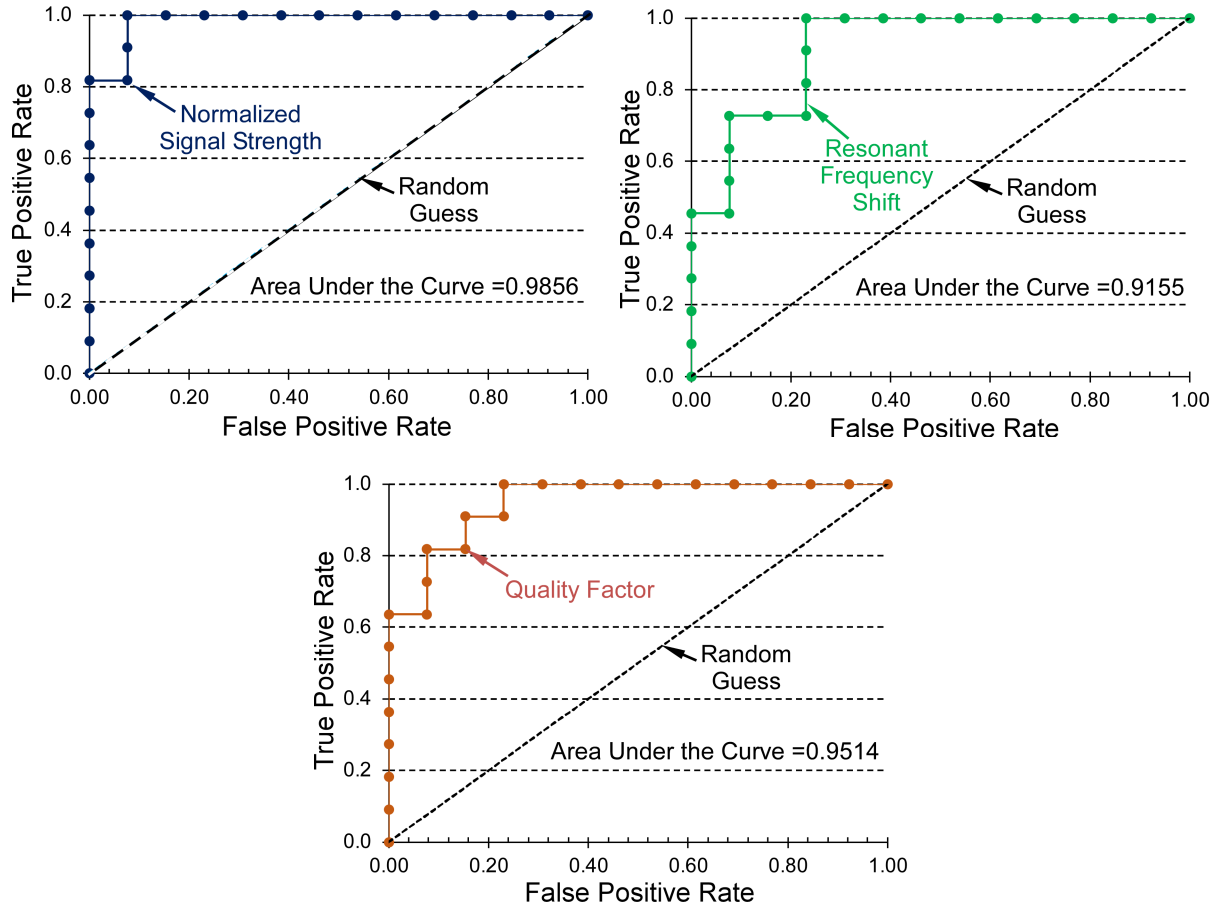

Fig. 3.18: ROC curve for normalized signal strength (left top), resonant frequency shift (right top), and quality factor (bottom) for diagnosing occlusion in a biliary stent.

Phase noise

The physical fluctuations in a resonator subsequently perturb the phase of the oscillation and produce phase fluctuations. These phase fluctuations are converted into noise sidebands around the carrier. For an ideal resonator frequency response, there will be a single peak in the frequency spectrum at the exact resonance frequency of the carrier. In any real resonator, the phase variation generates two sidebands spaced from the carrier on both sides on a frequency spectrum. The upper sideband is identical to the lower sideband in terms of phase noise. This is illustrated in Fig. 3.19.

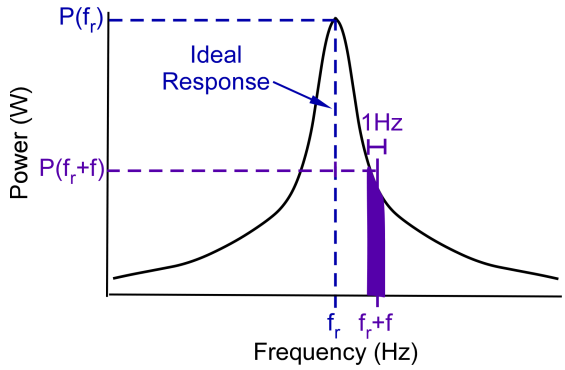

Fig. 3.19: Illustration of phase noise definition.

The generated sideband is conventionally given by the ratio of noise power to carrier power for 1 Hz bandwidth with offset frequency from the carrier. This is defined as phase noise as a function of offset frequency as *L(f)* and given by [Yan06]:

$$L(f) = 10log\frac{P(f_r+f,1\ Hz)}{P(f_r)}\ dBc/Hz \tag{3.8}$$

where $P(f_r)$ is the carrier power (power at the resonant frequency), and $P(f_r+f,\ 1Hz)$ is the single sideband power at frequency offset f from the carrier frequency f_r with the measurement bandwidth of 1 Hz as shown in Fig 1. *L(f)* is thus in units of decibel referred to the carrier power per hertz (dBc/Hz).

An empirical formula for the phase noise of the resonator is given by Leeson's equation [Lee66, Rhe95]:

$$L(f) = 10log\left\{\frac{FKT}{2P(f_r)}\left[1+\frac{f_c}{f}+\left(\frac{f_r}{2fQ}\right)^2\left(1+\frac{f_c}{f}\right)\right]\right\}\ dBc/Hz \tag{3.9}$$

where F is the noise factor (assumed to be 1 for an ideal case), K is the Boltzmann constant (= 1.38 × 10^{-23}), T is the temperature (=300 K), f_r is the resonant frequency (=180.8 kHz, calculated experimentally), $P(f_r)$ is the power at resonant frequency (= 0.1 W, calculated experimentally), f_c is the flicker corner frequency (assumed to be zero for ignoring flicker noise), Q is the quality factor (=507, calculated experimentally) and f is offset frequency at which the phase noise is

calculated. The phase noise is calculated for the resonator designed in this chapter and plotted in Fig. 3.20.

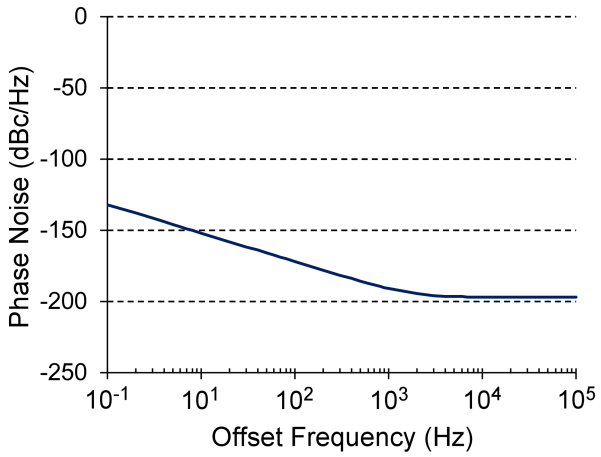

Fig. 3.20: Phase noise of the resonator estimated using Leeson's equation.

The sensor was characterized using the interrogation module shown in Fig. 3.7. The coil was made of 10 turns each for the transmitting coil as well as the receiving coil. The coil diameter was 3.5 cm, and the width of the coil was 2.2 cm for a total 20 turns. Excitation current across transmit coils was 180 mA (peak to peak). Commercial Helmholtz coils were used for DC bias at 1.2 G (with conversion factor 1 A ≈ 1 G).

The phase noise of the entire system is calculated as follows. The resonant response of the sensor in terms of amplitude (extracted from the sensor response experimentally), as well as power from the experiment, is shown in Fig. 3.21.

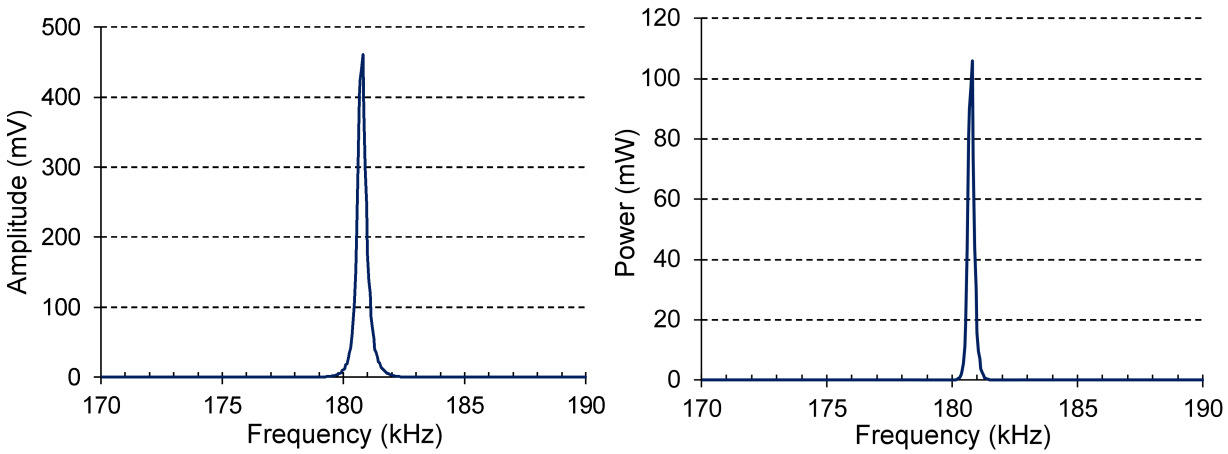

Fig. 3.21: Resonant response of the resonator in terms of amplitude (Left) and power (Right).

The power $P(f)$ at a frequency, f was calculated as:

$$P(f) = \frac{V(f)^2}{2} \; Watts \tag{3.10}$$

where *V(f)* is the amplitude of the detected sensor sine wave signal at the excited frequency *f*. The resistance is assumed to be 1 Ω. Ideally, the response should have been a single impulse at the resonant frequency (180.8 kHz). The noise power spectral density is calculated as follows [Yan06]:

$$Noise\ spectral\ density\ (f) = \sqrt{P(f_r + f, 1\ Hz)} = \sqrt{\frac{V(f_r+f)^2}{2}} \quad {}^{V}/_{\sqrt{Hz}} \tag{3.11}$$

where $P(f_r+f,\ 1Hz)$ *is* the side band power at an offset frequency of *f* in a 1 Hz bandwidth, and this is equal to the square of noise power spectral density. This noise is plotted in Fig. 3.22.

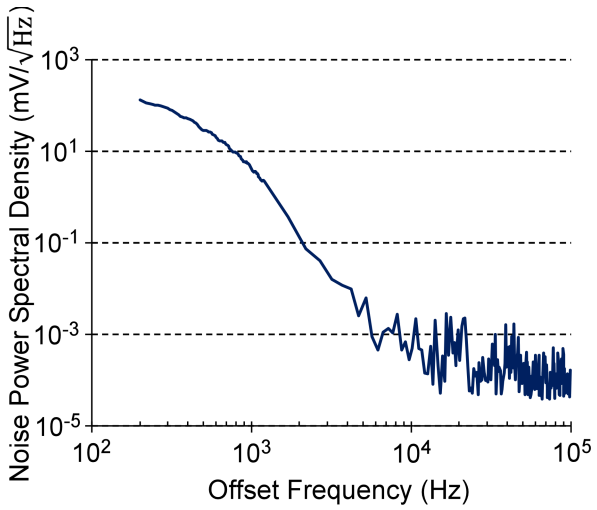

Fig. 3.22: Noise power spectral density with respect to offset frequencies.

The phase noise is calculated using the equation (3.8) and plotted below. $P(f_r)$ is the power at the resonant frequency. Power is calculated by squaring the amplitude value at each frequency. The resulting phase noise plot is shown in Fig. 3.23.

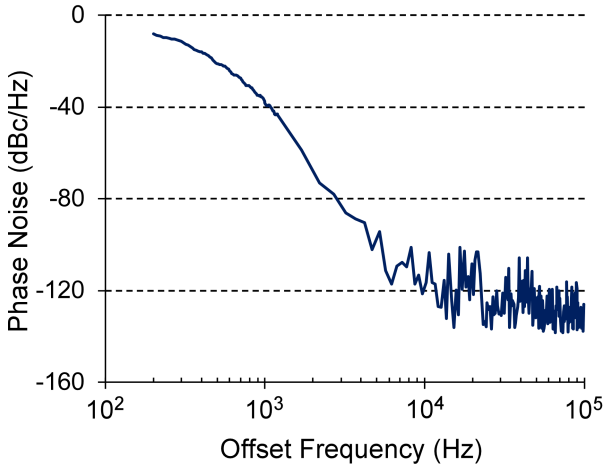

Fig. 3.23: Phase noise with respect to offset frequencies.

Total Noise Equivalent Magnetic Field

Random thermal agitation from the molecules in the environment affects the motion of any resonator. Using Equipartition theorem and Nyquist relation, the spectral density of the fluctuating noise force is given by [Gab93]:

$$F = \sqrt{4K_bTb} \quad N/\sqrt{Hz} \tag{3.12}$$

where K_b is the Boltzmann constant, T is the temperature and b is the damping coefficient. The noise displacement response is given by:

$$|Z_n(f)| = \frac{F\,G(f)}{k} = \frac{G(f)\sqrt{4K_bTb}}{k} \tag{3.13}$$

where k is the equivalent spring constant and $G(f) = 1/\sqrt{[1-(f/f_r)^2]^2 + ((f/f_r)^2/Q^2)}$. For a resonant sensor, $f=f_r$ and thus $G(f) = Q$. This gives:

$$|Z_n(f_r)| = \frac{Q\sqrt{4K_bTb}}{k} = \sqrt{\frac{4QK_bT}{m{\omega_r}^3}}\frac{m}{\sqrt{Hz}} \tag{3.14}$$

where m is the effective mass and $\omega_r = \sqrt{k/m}$.

Using the constitutive relation coupling the applied magnetic field and strain developed described in Chapter 1 equation (1.1)and assuming that for amorphous materials behave isotopically and also considering no external applied stress, equation (1.1) to [Pep15a]:

$$\begin{bmatrix}\varepsilon_{xx}\\ \varepsilon_{yy}\\ \varepsilon_{zz}\\ \varepsilon_{xy}\\ \varepsilon_{yz}\\ \varepsilon_{zx}\end{bmatrix} = \begin{bmatrix} d_{xx} & d_{xy} & d_{xy} \\ d_{xy} & d_{xx} & d_{xy} \\ d_{xy} & d_{xy} & d_{xx} \\ 0 & 0 & 0 \\ 0 & 0 & 0 \\ 0 & 0 & 0 \end{bmatrix} \begin{bmatrix} H_x \\ H_y \\ H_z \end{bmatrix} \tag{3.15}$$

Considering an applied field and strain component only in the x-axis (i.e. strain ε_{xx}) for the longitudinal vibrations of a free-free beam magnetoelastic resonator gives:

$$\varepsilon_{xx} = d_{xx}H_x \tag{3.16}$$

The equivalent force on the beam for generating this strain is given by:

$$F_s = AE\varepsilon_{xx} = AEd_{xx}H_x \tag{3.17}$$

where A is the cross-section area of the resonator and E is the young's modulus. For the equivalent mass damper system, the displacement (signal amplitude) is given by:

$$|Z_s(f_r)| = \frac{F_s}{k} = \frac{G(f)d_{xx}H_xAE}{m{\omega_r}^2} \tag{3.18}$$

For calculation of the total noise equivalent magnetic field (TNEM), the signal to noise ratio is equated to 1. This gives:

$$\sqrt{\frac{4QK_bT}{m{\omega_r}^3}} = \frac{Qd_{xx}H_xAE}{m{\omega_r}^2} \tag{3.19}$$

$$TNEM, H_x = \frac{1}{d_{xx}AE}\sqrt{\frac{4K_bTm\omega_r}{Q}}\ Am^{-1}/\sqrt{Hz} \tag{3.20}$$

For calculating the TNEM for the mass loaded resonator, the effective mass was calculated from COMSOL FEA. The effective mass integral is given by [Com19];

$$m = \int \rho(x)|r(x)|^2 dV \tag{3.21}$$

where $\rho(x)$ is the density of the material and $r(x)$ is the relative displacement. This equation can be integrated using COMSOL (in the derived values->volume integral) as; *solid.rho*(solid.dsp/p)^2* where p is the absolute displacement at the longitudinal endpoint. Using this technique, the effective mass is found to be 2.12×10^{-6} kg. The list of values required for using equation (3.10) is in Table 1.

Table 3.2: List of values used for calculation of TNEM

Parameter	Value	Source
d_{xx}	2.7×10^{-8} m A^{-1}	[Gre09b]
Q	507	Experimentally determined
K_b	1.38×10^{-23} kg m^2 K^{-1} s^{-2}	Constant
T	300 K	Room temperature
m	2.12×10^{-6} kg	Estimated from COMSOL
ω_r	$2\pi \times 180{,}800$ s^{-1}	Estimated from COMSOL
A	1.5×10^{-8} m^2	Resonator dimension
E	10^{11} kg m^{-1} s^{-2}	Metglas datasheet

Inserting the values from Table 1 in equation (10) gives $TNEM = 0.275\ \mathrm{p}T/\sqrt{Hz}$. The total noise equivalent magnetic field (equation 3.20) can also be found by directly taking ratios of the noise force (equation 3.12) and the magnetoelastic force generated (equation 3.17). This noise is

relatively low and will not limit the performance because the noise from interface circuit dominates. The resolvable frequency shift from the whole system including interface circuits and related calculations are discussed in the following paragraph.

Minimum Detectable Mass Load

Two resonant peaks will be distinguishable only if they are apart by at least half power bandwidth. So, the minimum detectable frequency shift (δf) is given by [Bou16]:

$$\delta f = \frac{f_r}{2Q} \tag{3.22}$$

where f_r (180.8 kHz) is the resonant frequency and Q (=507) is the quality factor. The loaded mass (Δm) and the frequency shift are related by [Gre09a, Bou16]:

$$\left(\frac{f_r}{f_r - \delta \mathrm{f}}\right)^2 - 1 = \frac{\Delta \mathrm{m}}{M} \tag{3.23}$$

where M is the effective mass of the resonator. Using equation (1) and (2), Minimum detectable mass load is given by:

$$M\left[\left(\frac{f_r}{f_r - \frac{f_r}{2Q}}\right)^2 - 1\right] = \Delta \mathrm{m} \tag{3.24}$$

The effective mass of the mass loaded resonator is 2.12×10^{-6} kg. This gives the minimum detectable mass load to be 4.24×10^{-9} kg.

3.4 Summary and Conclusions

A novel self-biased mass-loaded magnetoelastic sensor was designed, fabricated and tested. The sensor structure has two mass loads, one on each longitudinal end, which act as magnets

to bias the sensor while also preserving a low resonant frequency of the sensor despite its miniaturized footprint. The sensor was fabricated by bonding the sensor layer to the mass loads via an Au/In transient liquid phase bond. A hybrid coating approach using aluminum oxide followed by Parylene was used to ensure biocompatibility and corrosion protection after implantation. The sensor performance is evaluated by *in vitro* tests targeting the biomedical implant application of biliary stent monitoring. The sensor could detect synthetic occlusion in the stent with an accuracy of 97.84%.

Chapter 4: Hybrid In-stent Package for Biliary Stent Monitoring

4.1 Introduction

As discussed in Chapter 1 (1.3.2), one of the significant challenges in the implanted module for the biliary stent monitoring system is the mechanical protection of the sensor during and after implantation. As such, a package is required and the package must be both elastic enough to pass through the tight curvature during endoscopic deployment without experiencing permanent deformation and at the same time stiff enough to keep the sensor straight after implantation.

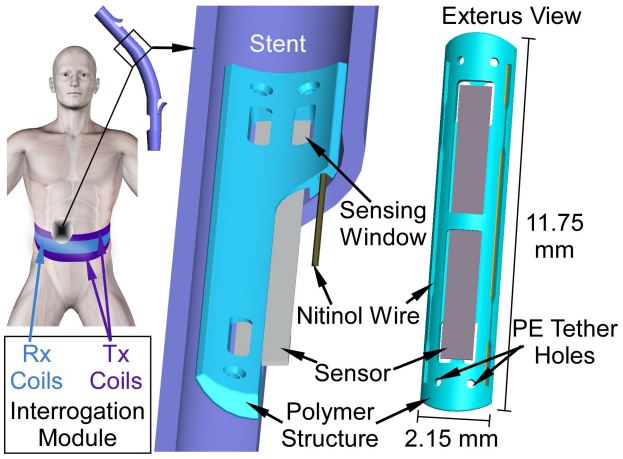

Fig. 4.1: The biliary stent monitoring system consists of an interrogation module and the instrumented stent. The magnetoelastic sensor in a Nitinol-reinforced-polymer hybrid package mounted into a plastic stent.

The hybrid package comprising a polymer structure reinforced by Nitinol wire is illustrated in Fig. 4.1. The polymer structure will hold the sensor in place while assembled in a stent and can be patterned with excellent resolution for very small sensors. Both the polymer (M3 crystal resin) and Nitinol are biocompatible and electromagnetically transparent. The highly elastic Nitinol

reinforcements in this hybrid package provide the required flexibility to pass through the tight curvature of the endoscope, and also provide the elastic shape recovery to keep the sensor straight within the curved bile duct anatomy. The polymer structure provides a smooth surface that protects the resonator while the introducer is passed through the stent. The hybrid package also includes features that allow the sensor to detect sludge deposition. The sensing window enables the sludge to accumulate on the sensor directly, allowing the sensor frequency response to be affected as intended. The polyethylene (PE) tether holes are for integrating and assembling the package onto the inner wall of the stent. The package also has a dedicated cavity in which to insert the sensor and keep the sensor secured in place, while also allowing the sensor to vibrate as necessary. This chapter describes the design and fabrication of the hybrid package, as well as its assembly into stent followed by benchtop and *in vitro* experimental methods, results, and conclusions.

4.2 Design, Fabrication and Assembly

Integrating the hybrid package into the stent increases the local bending stiffness of the stent. The change in stiffness is evaluated using the finite element analysis (FEA) tool COMSOL Multiphysics™. The model used consists of a segment of a 10 Fr (3.3 mm) diameter stent with the hybrid package attached to the inner side wall. A cross-sectional view of this is illustrated in Fig. 4.2(a). The Nitinol wires are inserted into the designated channels in the polymer portion, and for the purposes of simplifying the model assumed to be "bonded" to the adjacent polymer structure. The material properties used for the stent are those of polyethylene (E = 0.7 GPa ρ = 0.95 g/cm^3, v = 0.42) and for the polymer part of the package are those of M3 crystal resin (E = 1.46 GPa, ρ = 1.02 g/cm^3, v = 0.42) and for the wires those of Nitinol (E = 80 GPa, ρ = 6.45 g/cm3, v = 0.33). The classical "three-point bending test" is replicated when defining the load and boundary conditions. Points *a* and *b* have zero displacement along the y-axis to prevent rolling while point

c is fixed in all directions. The point *d* has zero displacement in y and z directions but can move along the x-axis. The external force is applied on a 1 mm length at the center of the stent segment. The force applied in the negative z-direction increases from 0 to 10 N. Nonlinear large deformations were allowed when solving the model. Fig. 4.2(b) shows the deformed hybrid package when the applied force is 10 N. (The deformed stent is not shown in this view). The maximum deformation of the package is 0.56 mm. The deformation against the applied force is plotted in Fig. 4.3. As expected, the bending stiffness of the stent is increased with the attachment of the hybrid package. The initial bending stiffness without a hybrid package is 15.5 N/mm and is increased by 12.79% to 17.78 N/mm with the attachment of the hybrid package.

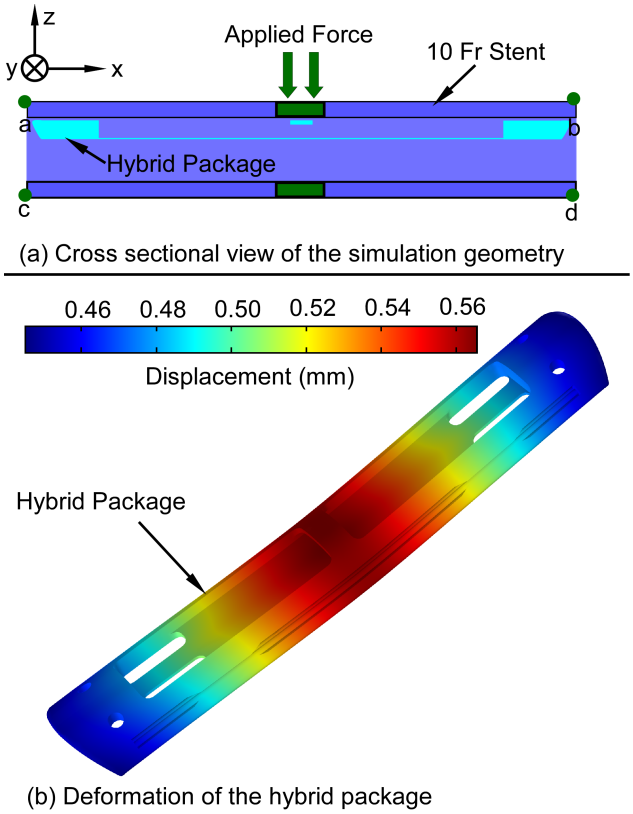

Fig. 4.2: (a) Cross-sectional view of a stent segment with the hybrid package used in the simulation. The stent segment length is 12 mm. The external force is applied on the green surface of the stent.(b) FEA simulation result showing the deformation of the hybrid package under an applied load of 10 N.

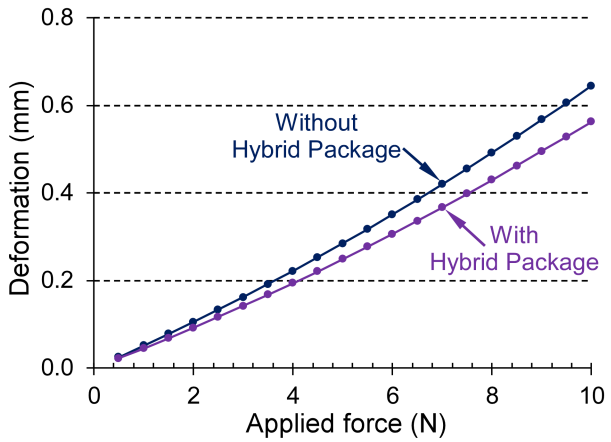

Fig. 4.3: Simulated displacement of the stent segment with and without the hybrid package due to the externally applied force.The bending stiffness increased from 15.5 N/mm to 17.78 N/mm (12.79%) after integrating the hybrid package.

The polymer structure in the hybrid package was fabricated using 3D printing technology. A high-resolution multi-jet 3D printer (ProJet 3500 HD Max) with a resolution of 16 µm was used to print this structure using M3 crystal resin. This resin is USP class VI biocompatible rated and ideal for printing highly detailed features within tight tolerances. The Nitinol wires (superelastic condition) with a diameter of 125 µm were acquired from Small Parts and cut to ~10 mm using a shear tool. A photograph of a fabricated polymer structure along with Nitinol wires is shown in Fig. 4.4. Photograph of the sensor packaged in the polymer package reinforced with the Nitinol wires is shown in Fig. 4.5.

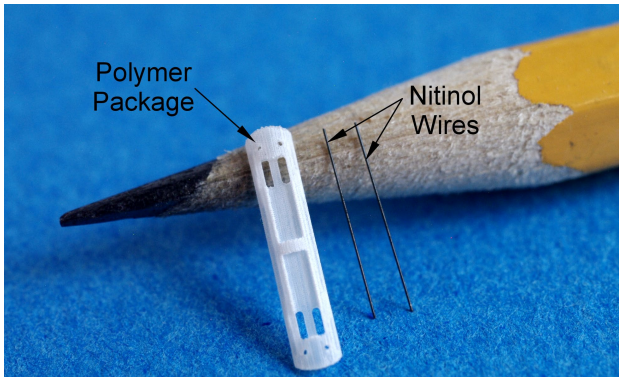

Fig. 4.4: 3D printed polymer package and 125 µm diameter Nitinol wires.

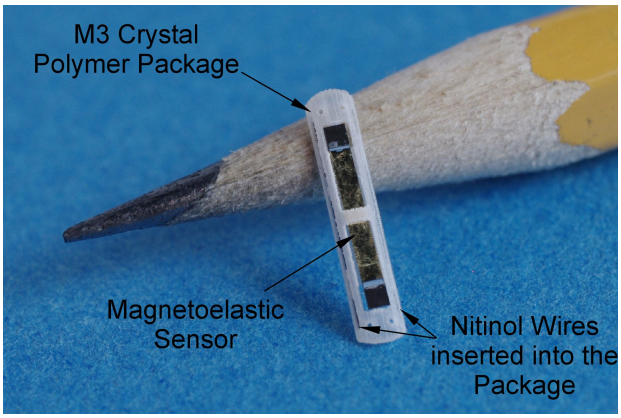

Fig. 4.5: Sensor in the hybrid nitinol reinforced hybrid package.

The sensor is packaged by inserting into the designated slot in the polymer structure of the hybrid package; the package is reinforced with Nitinol wires inserted into the channels on the sides. The packaged sensor is then integrated into an 8 cm, 10 Fr plastic stent (Cook Cotton-Leung Biliary Stent, CLSO-10-8). A small incision was made on one side of the stent, and the flap was peeled back partially. Then, the packaged sensor was inserted into the stent. Polyethylene (PE) tethers were passed through the holes on the package through the stents. PE threads were tightened and then melted onto the outer stent wall to conform to the smooth surface of the stent. Partially peeled stent flaps were placed back into their original position and then re-melted into the nearby stent material. The assembly process is illustrated in Fig. 4.6. The stent instrumented with the packaged sensor is shown in Fig. 4.7.

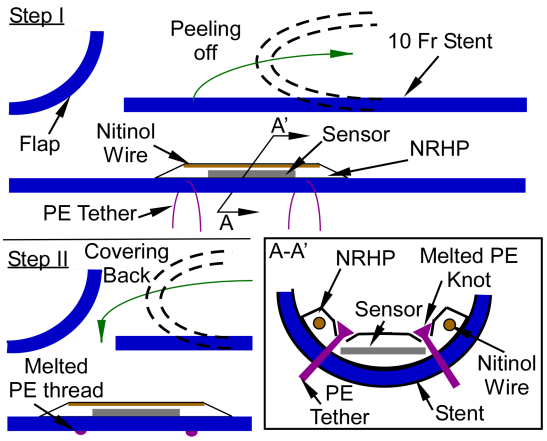

Fig. 4.6: Steps involved in assembling a packaged sensor to a commercial stent. Step I: Upper part of the stent is peeled off partially,and the hybrid packaged sensor was placed inside with PE tethers through the holes of the package as well as the holes made on the stent. Step II is sealing back the peeled part of the stent and melting the PE tethers to the outer wall of the stent. The cross-sectional view of the stent/package after step I (Inset)

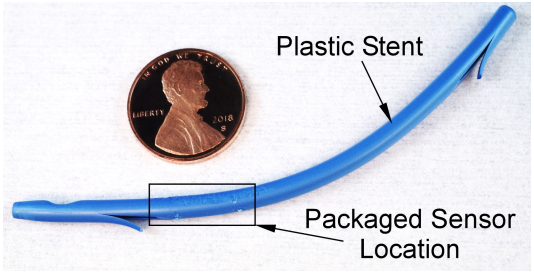

Fig. 4.7: Packaged sensor assembled in a commercial 10 Fr stent.

4.3 Experimental Results

Bending experiments

Bending tests were performed on instrumented stents, in which various radii of curvature (ROCs) were imparted to the stent, and the sensor was simultaneously interrogated to evaluate signal attenuation. The instrumented stents were also passed through an endoscope as in a typical delivery process, passing through the tightest curvature achievable (~2 cm) with the endoscope. Afterward, each sensor was interrogated, and any mechanical damage was visually evaluated. The goal of these tests was to ensure that the sensor signal is not significantly affected while the stent

is curved inside the bile duct and also to ensure that the sensor/package is not damaged while passing through the endoscope.

The first sets of bending tests were focused on evaluating the ability of the package to keep the sensor straight if implanted in an inherently curved bile. The stent was placed inside a polymer tube, which was fixed on one end. The other end of the tube was deflected to impose various radii of curvature onto the stent, reducing from 10 cm to 4 cm (Fig. 4.8).

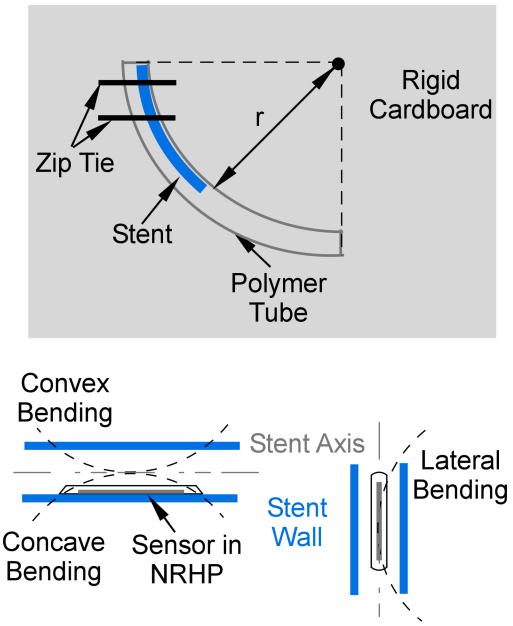

Fig. 4.8: Bending tests performed on the instrumented stent involves a fixture used to bend the stent to a required curvature 'r' (Top). The instrumented stent was bent in all three directions (Bottom).

The sensor was interrogated while the stent was bent. Typical acquired frequency responses for convex bending are shown in Fig. 4.9, 4.10 and 4.11. For the convex bent cases, the maximum shift in the resonant frequency was only by 0.02% (R_C of 6 cm) and the maximum decrease in the quality factor was by 12.5% (R_C of 8 cm). For the concave bent cases, the maximum shift in the resonant frequency was only by 1.01% (R_C of 4 cm). For the lateral bent cases, the maximum shift in the resonant frequency was only by 0.03% (R_C of 10 cm).

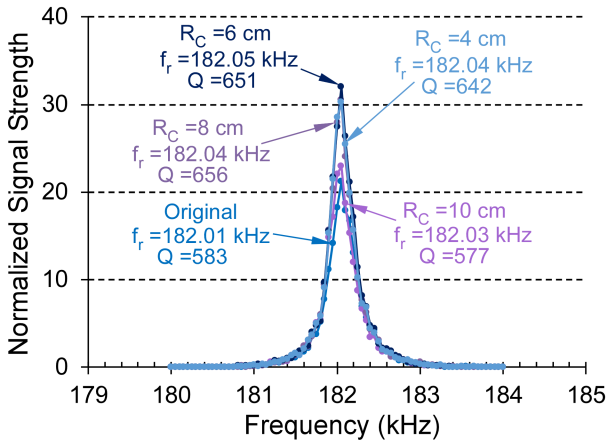

Fig. 4.9: Typical frequency responses when the instrumented stent was bent in various radii of convex curvature.

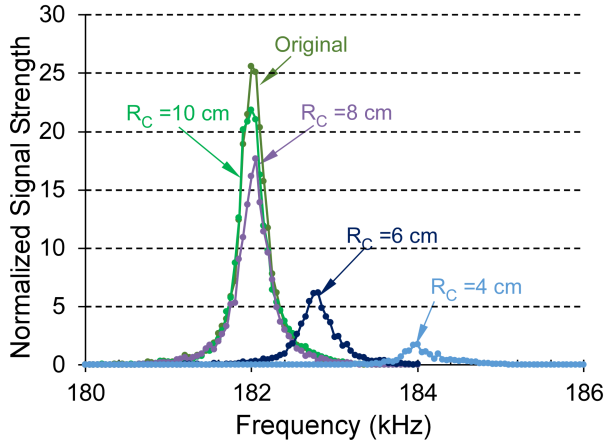

Fig. 4.10: Frequency response when the instrumented stent is bent in the concave direction.

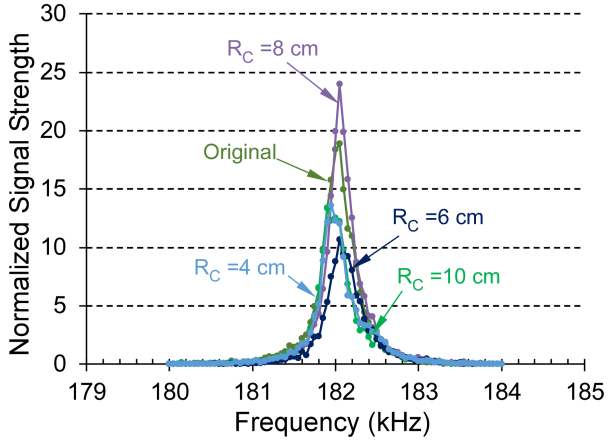

Fig. 4.11: Frequency response when the instrumented stent is bent in the lateral direction.

The signal strength decreased for some bent cases, but there were no cases exhibiting total signal loss. These results indicate that there will not be any noticeable effect on the signal response when

the instrumented stent is bent by an inherently curved anatomical bile duct. The package is practically stiff enough to keep the sensor straight under the expected externally applied stress.

The next set of bending tests were performed in order to evaluate the ability of the package to pass through the tight curvature at the end of the endoscope when the elevator is raised, resulting in a R_c of ~2 cm. For this, the stent was passed through the endoscope in a full deployment process (Endoscope I). The endoscopic procedure was repeated twice more (Endoscope II, Endoscope III). The results of these tests are plotted in Fig. 4.12. The maximum shift in resonant frequency was only by 0.14% (Endoscope III), and the maximum decrease in the quality factor was by 26% (Endoscope III). The signal strength was reduced to as low as 40% of the original value. The package was inspected after all these experiments. There was no damage to the sensor as well as the package. These experiments show that the hybrid package is flexible enough to go through this intense radius of curvature and still elastically recover its original shape without getting damaged. A reasonable signal was observed for all the test cases. This indicates that the integrity of the sensor, as well as the package, is maintained.

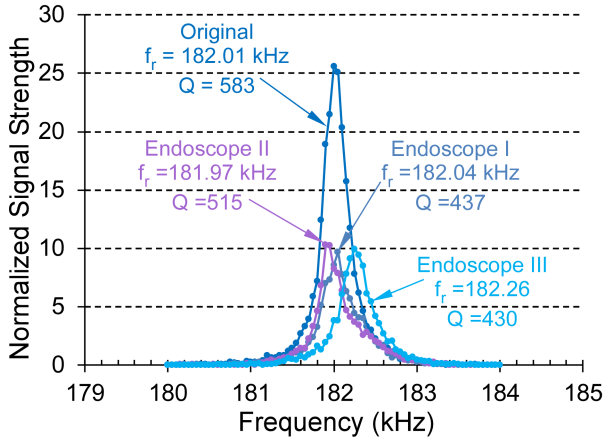

Fig. 4.12: Frequency responses after the instrumented stent is passed through an endoscope multiple times.

In vitro experiments

In vitro experiments were conducted to evaluate the effect of the presence of the package (with sensor) in the stent with respect to biomass deposition and occlusion development. An accelerated *in vitro* model created sludge deposition inside the stent using fiber-rich bile inoculated with *Escherichia Coli* [Sur18]. Nutrient media for culturing the bacteria was prepared by adding dextrose (100 mg), ammonium sulfate (100 mg), potassium phosphate dibasic (700 mg), potassium phosphate monobasic (200 mg), magnesium sulfate heptahydrate (50 mg), and sodium citrate (10 mg), to 100 mL distilled water. The components were mixed well, and 10% bile powder (Oxgall, US Biological) was added to the media. The media was then autoclaved to ensure sterility. *Escherichia Coli* (ATCC 25922) was cultured in this solution and then allowed 10 passages in order to make the bacteria bile resistant. The bile-resistant bacteria were stocked with 20% glycerol at -20°C for future use.

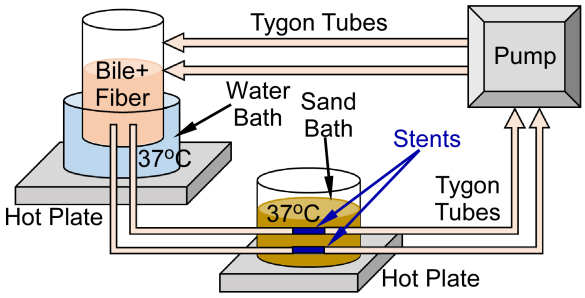

Fig. 4.13: The in vitro experimental set-up.

The schematic of the flow set-up is shown in Fig. 4.13. A dual-channel peristaltic pump, in combination with a network of tubes, was used to mimic the bile flow. Each experimental set consisted of two stents: one instrumented and the other non-instrumented. The stents were connected to the flow system in separate channels. The bile reservoir contained 90 mL of 10% bile with bacteria cultured to an optical density of 0.4 - 0.8. Fiber (0.5 g, CreaFibe SC90) was added to

the reservoir to mimic dietary fiber in the bile. The reservoir was kept at 36ºC - 38ºC via a heated water bath, which helped to keep the bile solution at a uniform temperature. The temperature was measured intermittently using a probe, and the reservoir was kept closed at all other times to reduce evaporation. A magnetic mixer inside the inoculated bile reservoir was used to mix at 600 rpm; this kept the fiber suspended in the bile rather than settling to the bottom of the reservoir. Then, the bile was pumped through the channels and the stents at a flow rate of ≈0.5 mL/min. The section of the channels where the stents were located was immersed in a heated sand bath, which was kept at a constant temperature of 37 ºC. Once the stents became occluded, they were removed from the test-setup and interrogated. Full occlusion is defined when the flow through the channel was observed to have stopped, and occlusion was confirmed by applying 0.5-inch height water pressure to the stent (~124 Pa) and observing no water flow. Experiments on five sets of stents were conducted. Photos of a representative set of occluded stents are shown in Fig. 4.14. The stents were primarily occluded in the inlet of the stents. The times taken for occlusion of the stents are listed in Table 4.1.

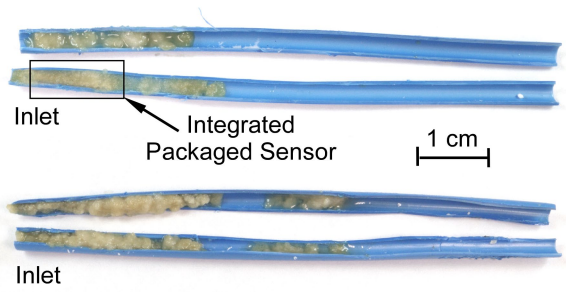

Fig. 4.14: Photographs of the occluded instrumented and non-instrumented stents.

Table 4.1: *In vitro* results, stent occlusion time for instrumented, non-instrumented 8 cm stents. sensor performance, RF – resonant frequency, QF – quality factor.

Exp #	Occlusion Time (Hrs)	
	Instr. (t_i)	Non-instr. (t_n)
1	6.5	8
2	7	5
3	6.5	5.5
4	6	6.5
5	7	5
6	8	6.5
7	6.5	5.5

There is no clear or obvious acceleration of occlusion due to the presence of the sensor/package from these experiments. A non-inferiority test was done on these results and discussed in the next section. The sensor resonant characteristics before and after occlusion in the instrumented stents are listed in Table 4.2.

Table 4.2: *In vitro* results, resonant frequency (RF), quality factor (QF).

Exp. #	Before Occlusion		After Occlusion		Shift in RF (kHz)	Decrease in QF
	RF (kHz)	QF	RF (kHz)	QF		
1	259.7	130	261.2	98	1.5	32
2	256.8	135	258.1	109	0.7	26
3	256.3	114	257.8	102	1.5	12
4	260.4	161	259.8	125	0.6	36
5	259.7	120	261	94	1.3	26
6	256.8	118	257.3	99	0.5	19
7	257.2	115	259.2	90	2	25

There is a noticeable resonant response change after the occlusion. There is a shift in the resonant frequency by at least 0.6 kHz up to 2 kHz after occlusion. Also, the quality factor

decreases by at least 12 and as much as 36 after occlusion. This indicates that the sensor can be utilized to discern full occlusion in the instrumented stents.

Non-inferiority Test

Randomized controlled trials (RCT) are carried out to compare a new experimental procedure/treatment/medicine to an existing procedure/treatment/medicine [Les08]. The RCT is called a superiority test when the trial is to prove that the new treatment is superior to the existing one. If the objective is to show that they are equivalent, it is called an equivalency test. Finally, a non-inferiority (NI) test is used to evaluate whether the new treatment is not unacceptably less effective than the existing treatment [Hah12]. These tests use the outcome of the trials to determine the superiority/equivalence/non-inferiority. If all the outcomes from the new treatment are better than the existing one, the new treatment is superior. If all the outcomes of the new method are close to the existing method within a predefined margin of δ, they are equivalent. Finally, if the new treatment outcomes are not worse than the existing method with at least a margin of δ, the new method is found non-inferior to the existing method. These concepts are illustrated in Fig. 4.15.

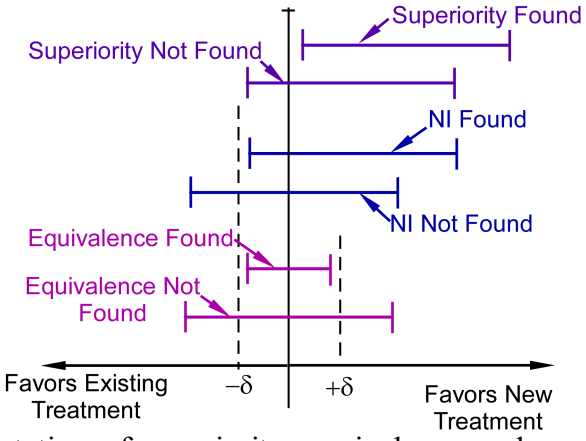

Fig. 4.15: Graphical representation of superiority, equivalency and non-inferiority tests and outcomes.

A student t-test using the test statistic t-score can be used to further quantify the outcome of these tests. Calculation of the t-score and corresponding p-value (i.e. marginal significance) helps to determine the significance of the results [Mas11].

A non-inferiority test RCT is chosen here. This test determines whether the new intervention is clinically non-inferior, but still beneficial for patients in terms of other advantages like less-intensive treatment, lower cost or fewer side effects [Reh16, Las03]. Here, the instrumented stent offers the advantage of occlusion detection but could be inferior in terms of the stent occlusion time, due to the presence of the sensor and package. The NI test is utilized to demonstrate that the instrumented stent is not inferior to the non-instrumented stents in terms of occlusion time. The null hypothesis is that the instrumented stent occludes faster than non-instrumented stents by at least δ hrs. Mathematically, the mean of occlusion time for instrumented stents (μ_i) is worse than occlusion time for non-instrumented stents (μ_s) by at least δ hrs:

$$H_0: \mu_i - \mu_s \leq -\delta \tag{4.1}$$

The alternative hypothesis is that the instrument stent does not occlude faster than non-instrumented stents or occludes faster but not worse than a difference in occlusion time of δ hrs. Mathematically:

$$H_a: \mu_i - \mu_s > -\delta \tag{4.2}$$

The test statistic, t-score for the test for samples with unequal variances and sample sizes is given by [Mas11]:

$$t = \frac{\mu_i - \mu_s + \delta}{\sqrt{{S_p}^2 (\frac{1}{n_i} + \frac{1}{n_s})}} \tag{4.3}$$

where n_i and n_s are the sample sizes of the instrumented stents and non-instrumented stents, respectively. Further:

$$S_p = \sqrt{\frac{(n_i-1){S_i}^2+(n_s-1){S_s}^2}{(n_i+n_s-2)}} \tag{4.4}$$

where S_i and S_s are the observed standard deviation of the set of instrumented stents and non-instrumented stents, respectively. For $n_i = n_s = n$, (4.3) reduces to:

$$t = \frac{\mu_i-\mu_s+\delta}{\sqrt{\frac{{S_i}^2+{S_s}^2}{n}}} \tag{4.5}$$

For the observations in Table 4.1, $\mu_i = 6.79, \mu_s = 6, S_i = 0.40, S_s = 1.17, n = 7$. The NI margin is chosen so that the $\delta = 0.1\mu_s = 0.6$. This margin is a 90% fraction of μ_s which is generally used in the field of antibiotics [Alt17]. For this NI margin, the t-score calculated from (4.4) is 2.92. The corresponding p-value at a significance level of 0.05 (95%) is 0.0133 (one-tailed test, calculated using a p-value calculator [Soc19]). The result is significant since p <0.05**.** The result is graphically shown in Fig. 4.16.

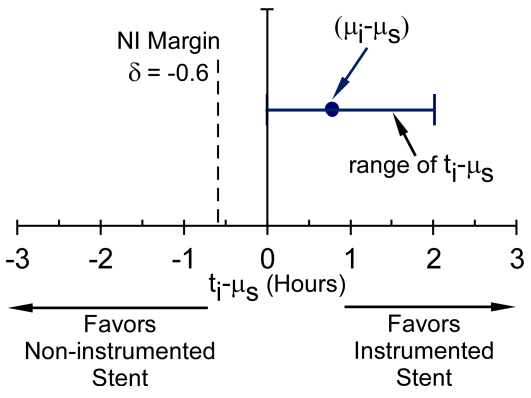

Fig. 4.16: Graphical representation of non-inferiority of occlusion time of instrumented 8 cm stents to the occlusion time of non-instrumented stents.

Long stents were not available for more experiments, hence shorter 3 cm stent pieces were used to gather more data on occlusion dynamics. The times taken for occlusion of the stent pieces are listed in Table 4.3. The sensor performance is listed in Table 4.4.

Table 4.3: *In vitro* results, stent occlusion time for instrumented, non-instrumented 3 cm stents. sensor performance, RF – resonant frequency, QF – quality factor (Shorter Stents).

Exp. #	Occlusion Time (Hrs)	
	Instr.	Non-instr.
1	6	7
2	6.5	6
3	6	5.5
4	7	7
5	5	5.5
6	5.5	6

Table 4.4: *In vitro* results, resonant frequency (RF), quality factor (QF) (Shorter Stents).

Exp. #	Before Occlusion		After Occlusion		Shift in RF (kHz)	Decrease in QF
	RF (kHz)	QF	RF (kHz)	QF		
1	259.9	138	260.2	115	0.3	23
2	252.0	105	255.0	85	3	20
3	260.8	123	261.4	84	0.6	39
4	259.0	115	259.9	93	0.9	22
5	257.6	116	258.4	98	0.8	18
6	255.5	127	257.5	103	2	24

Experiments with shorter stents also showed that the sensor could detect occlusion in terms of a shift in resonant frequency and a decrease in quality factor. Further, there is no obvious acceleration in occlusion time for the instrumented stent pieces compared non-instrumented stent pieces. This experimental data leads to the conclusion that the presence of packaged sensor does not have any meaningful negative impact on the occlusion dynamics.

4.4 Summary and Conclusions

A hybrid metal-polymer package is designed to protect magnetoelastic sensors used in a wireless biliary stent monitoring system. The hybrid package is made of a polymer structure reinforced with highly elastic Nitinol wires. Bending tests were conducted on the package-integrated stents and found that the package is flexible enough to pass through the endoscopic procedure and protect the sensor without any damage. In addition, experiments show the package aids in maintaining local stent straightness while the stent is deployed inside the inherently curved bile duct to minimize the signal attenuation due to sensor bending. Finally, *in vitro,* experiments were conducted to evaluate the effect of the presence of the package in terms of occlusion time. An accelerated stent occlusion model utilized cultured bacteria to create the sludge development and occlusion inside both instrumented and non-instrumented (control) stents. Using a statistical non-inferiority test, it was found that the instrumented stents are not inferior to the non-instrumented stents in terms of the occlusion time.

Chapter 5: Interrogation Module for Biliary Stent Monitoring

5.1 Introduction

A magnetoelastic system for biliary stent monitoring consists of a magnetoelastic sensor and an external interrogation module for remotely interacting with the implanted sensor. Typically, the sensor is excited with a magnetic field, but the sensor response can be detected via magnetic, acoustic, or optical means [Gri11]. Optical means that require phototransistor/laser are not feasible in an implanted situation as an implanted sensor is obscured from illumination by tissue. Acoustic approaches have yet to demonstrate a substantial wireless range [Nam17]. As such, the system developed in this work excites the sensor and detects the sensor response in the magnetic domain. The system consists of a set of inductive coils to generate the magnetic field for exciting the sensor and for detecting the magnetic field generated by the sensor, along with various hardware components. Also, to be considered are the application specific challenges facing biliary stent monitoring, including (i) signal feedthrough, (ii) wireless range, and (iii) clinical utility. These are discussed in detail in a previous chapter (Section 1.2.3). Along with the packaged sensor, the complete magnetoelastic system is illustrated in Fig. 5.1. This chapter discusses the design and implementation of the interrogation module and demonstration of the module in benchtop experiments, *in vitro*, *in situ* and *in vivo*. The approach used in developing this module can also be applied for interrogating magnetoelastic sensors for other applications.

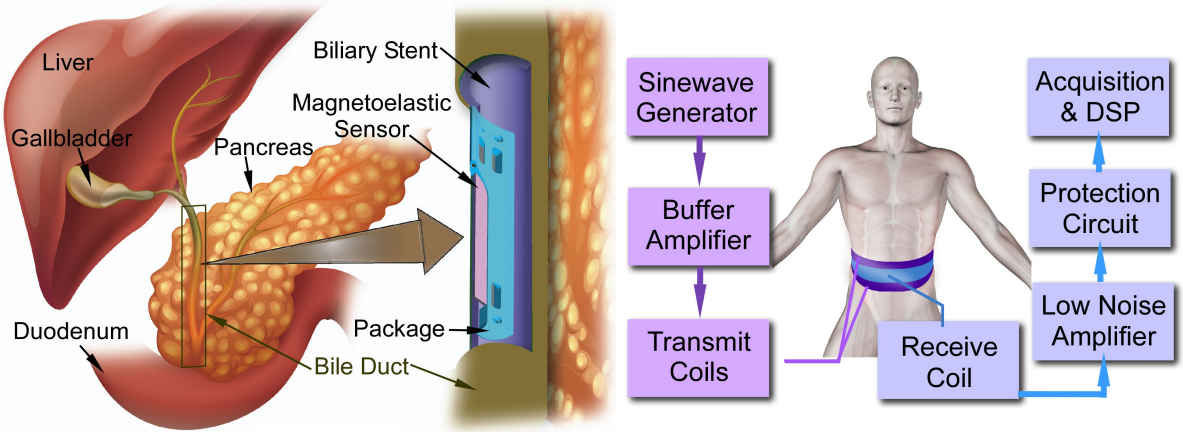

Fig. 5.1: The biliary stent monitoring system consists of a magnetoelastic sensor integrated with the biliary stent for detecting occlusion (left) and the interrogation module (right).

The interrogation module consists of transmit coils for exciting the sensor magnetically and a receive coil for sensing the magnetic field produced by the vibrating sensor. The waveform generator (National Instruments, NI-5412) along with the buffer amplifier (Texas Instruments, TI BUF634P) delivers the required sinusoidal voltage across and current through the transmit coil. As indicated in a previous chapter (Section 1.2.3), a time domain decoupling approach is used here to minimize the signal feedthrough. Hence, the interrogation cycle consists of a transmit part which is a burst sinusoid and a receive part where no voltage is generated and instead the sensor ringdown is detected. The magnetic field generated by the transmit coil as a result of the sinusoidal current excites the sensor, and the sensor responds with its own magnetic field while it vibrates. This sensor-generated magnetic field will create a current through the receive coil, and this is amplified and converted to a voltage using a low noise amplifier (LNA) (Stanford Research Systems, SR-570) and acquired to a data acquisition device (NI-6115) for further processing. The protection circuit blocks and shunts large input currents away from the low noise amplifier; these currents would otherwise arrive at the low noise amplifier input during the transmit portions of the interrogation cycle due to mutual induction between the transmit and receive coils.

The following sections describe the hardware implementation of the interrogation module and the details of the digital signal processing steps implemented. Further, *in vitro* experimental results as well as *in situ* experimental results are detailed, followed by conclusions.

5.2 Hardware Implementation

As indicated previously, the major challenges focused on in developing the interrogation module are (i) signal feedthrough (ii) wireless range (iii) clinical utility. The hardware used in the interrogation module is carefully selected and designed to overcome these challenges. These hardware consists of transmit/receive coils; the waveform generator and buffer amplifier on the transmit side; and the LNA, protection circuit and data acquisition device on the receiving side. The specific purpose of these hardware components in achieving the goal of signal feedthrough elimination, wireless range improvement and clinical utility is detailed in the following sections.

Transmit/Receive Coils: The receive coil and the transmit coils were fabricated considering the clinical utility and matching their impedance with specifications of the next instrument in the system for the improved efficiency. For the transmit coils, the generated magnetic field is maximized by optimizing the number of turns of the coil and the current through them. The impedance of the coils must be matched to the buffer amplifier for this optimization. The transmit coil can be modeled as a multi-turn coil with radius r_c and width a_c as shown in Fig. 5.2.

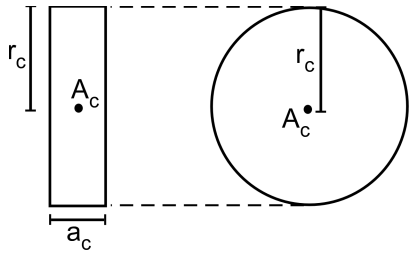

Fig. 5.2: Transmit coil modeled as a simple multi-turn cylindrical coil with radius r_c and width a_c.

Using the Biot-Savart law, the magnetic field at the center (position A_c in Fig. 5.2) is given by:

$$B = \frac{\mu_0 NI}{2r_c} \tag{5.1}$$

where, μ_0 is the permeability in vacuum, I is the RMS current, r is the radius of the coil, and N is the number of turns. For this coil design, the inductance is given by [Whe28]:

$$L = \frac{N^2 {r_c}^2}{25.4(8r_c+11a)} mH \tag{5.2}$$

where r_c (~0.1 m) is the radius, a is the width of the coil and N is the number of turns in the coil. This equation is valid for $2r_c > a_c > 0.2r_c$. For the wire used, the width per turn is measured to be 1.25×10^{-3} m, resulting in total width, a_c, of $N \times 1.25 \times 10^{-3}$ m. The resistance of the coils is relatively small compared to the reactance presented by the inductance and thus is neglected in the total impedance calculations. The effective coil impedance is thus given by:

$$Z = \frac{N^2 {r_c}^2 \omega}{25.4(8r_c+0.00125N)} m\Omega \tag{5.3}$$

where ω (= $2\pi f$, f = 155 kHz – the expected resonant frequency of the resonator) is the radial frequency of the signal. Equating the coil impedance to 50 Ω and using equation (5.3), it is found that two parallel coils with 14 turns in each will be the optimum for maximizing the generated magnetic field at the expected sensor frequency. A current of 0.125 A through each of these coils will result in a magnetic field of ≈0.2 G.

The sensing side of the interrogation module consists of the receive coil connected in series with the protection circuit, LNA, and data acquisition device. The number of turns of the receive coil is optimized for maximum current generation for a given magnetic flux density, as the LNA is a transimpedance amplifier. In this case, the receive coil is connected in series with a switch, protection circuit, and the LNA. The equivalent resistance of these circuit elements is estimated

to be 365 Ω. The receive coil acts as a voltage source while the magnetic field generated by the magnetoelastic sensor couples with it. This can be modeled as the circuit shown in Fig. 5.3.

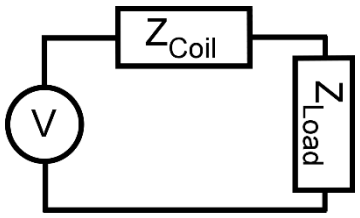

Fig. 5.3: Receiving circuit modeled with a voltage source for illustrating impedance matching.

The voltage V generated across the coil by varying magnetic field is given by Faraday's law of electromagnetism:

$$V = -N\frac{d\Phi}{dt} = -N\omega\Phi \tag{5.4}$$

where Φ is the magnetic field, ω is the frequency and t is the time. The current generated through the circuit is given by:

$$I_c = \frac{V}{Z_{Coil}+Z_{Load}} \tag{5.5}$$

where Z_{coil} is the impedance of the coil and Z_{Load} is the impedance of the load (365 Ω). Since this is a multi-turn coil, we can use Eq. (5.3) to estimate the coil impedance. Simplifying Eq. (5.3) shows that the Z_{coil} is approximately proportional to the square of N. This gives:

$$Z_{Coil} = mN^2\omega \tag{5.6}$$

where m is a constant of proportionality. Equations (5.4), (5.5) and (5.6) gives the current through the coil as:

$$I_c = \frac{N\omega\Phi}{mN^2\omega+Z_{Load}} \tag{5.7}$$

From this, it is clear that for a given frequency, the highest current magnitude is generated when N is chosen such that Z_{Coil} is equal to Z_{Load}. Using equation (5.7), it is found that a single coil with 28 turns is expected to provide optimum sensitivity.

Considering clinical utility, rigid cylindrical coils are not ideal for use on patients of various sizes, so the coils have been reimagined in the style of a belt. The belt can be first disconnected at the ends, then wrapped around the midsection of the patient, then reconnected (Fig. 5.4). The transmit and receive coils have been fabricated from standard ribbon cables, with the connectors offset so as to form a continuous coil as shown in Fig. 5.4. All the coils are enclosed in nylon fabric as an added layer of structural integrity and electrical isolation. The position of the coils is maintained within the nylon fabric by stitching between each coil. Hook and loop connectors (Velcro) are used for form-fitting placement of the coil module around the midsection of the patient while allowing the dimensions of the resulting inductive loop to be adjusted within a useful range. This belt can be placed around a patient and formed into a coil using the standard snap-together ribbon cable connectors. These coils will be positioned on the body of the patient so that the sensor-integrated stent will be in the middle of the coil as shown in Fig. 5.4.

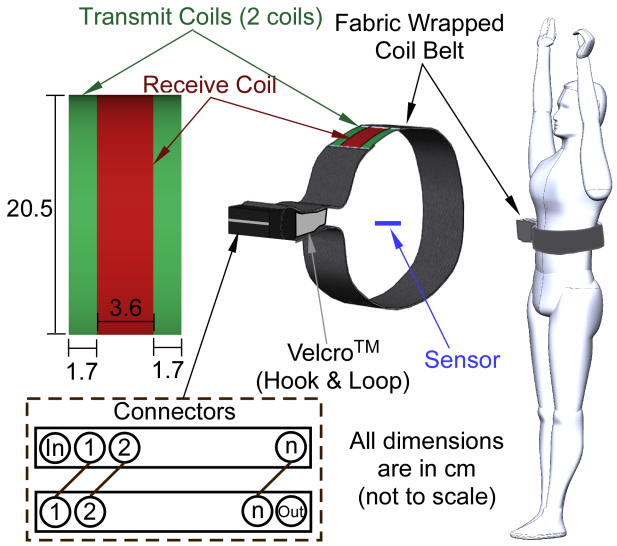

Fig. 5.4: Coil structure and clinical utility. The offset connection for the fabrication of a continuous coil from ribbon cable is also illustrated in the lower left.

Waveform generator and buffer amplifier: The waveform generator and buffer amplifier circuit are used to generate the burst sinusoid voltage across the transmit coils. The waveform generator is programmed in LabVIEW to generate the burst sinusoidal signal with the specified transmit and receive time. Transmit time corresponds to the duration of time in which the sensor is excited and receive time corresponds to the time where there is no transmit signal, but the sensor signals are acquired. In short, the waveform generator along with the buffer amplifier enables the implementation of time domain decoupling for signal feedthrough elimination.

The buffer amplifier acts as a buffer between the waveform generator and the coils. The buffer amplifier circuit also includes a metal oxide varistor (MOV) (Littlefuse V18ZA2P) as shown in Fig. 5.5.

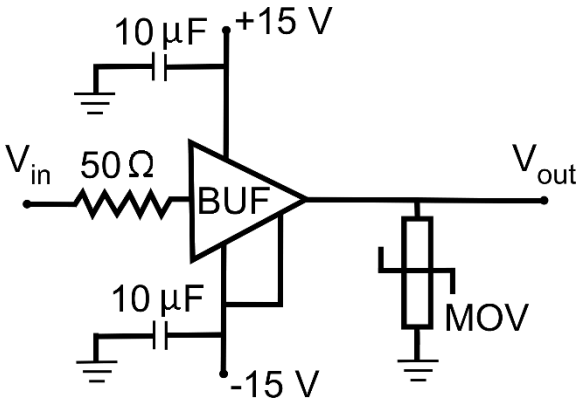

Fig. 5.5: Buffer circuit with the MOV for flyback voltage protection for the sine wave generator.

The MOV is used to protect the buffer amplifier from flyback voltage across the transmit coils as they are switched off. A MOV has a nonlinear current-voltage characteristic that is similar to that of a diode. The I-V characteristic of the MOV was measured experimentally and is shown in Fig. 5.6. This protects the amplifier from any flyback voltage of more than +/-12 V.

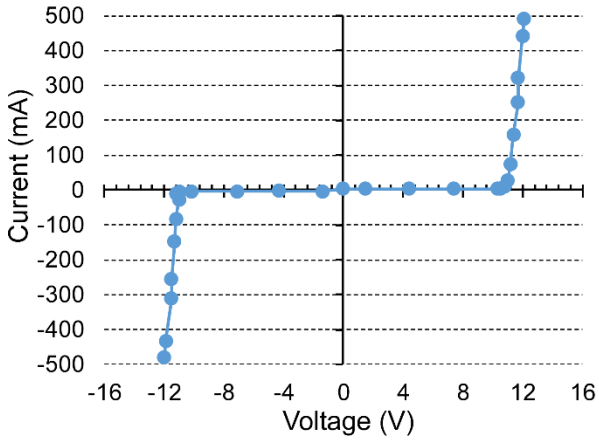

Fig. 5.6: I-V characteristics of the MOV.

Low noise amplifier, protection circuit and data acquisition device: The hardware components at the sensor signal reception side are the LNA, protection circuit and data acquisition device. The LNA amplifies the received signal while introducing minimal noise, which helps in improving the SNR which will subsequently improve the wireless range. The protection circuit is

for protecting the LNA from overdrive. Finally, the received signal is collected to a PC using a data acquisition device.

The selection of various settings on the LNA – including the passband of onboard filters, sensitivity, and high-bandwidth or low noise mode – determine its response. The passband for the LNA is set after estimating the sensor resonance frequency. The sensor resonance frequency f_r, can be calculated from the analytical equation for longitudinal vibration of an elastic beam [Nil15]:

$$f_r = \frac{1}{4l}\sqrt{\frac{Y}{\rho}} \tag{5.8}$$

where l is the length of the sensor, Y is the elastic modulus of the sensor, and ρ is the mass density of the sensor. This is experimentally found to be ≈160 kHz. Thus, the LNA is set to have a bandpass filter with passband 10 kHz - 300 kHz for rejecting the higher and lower frequency noise. The sensitivity is optimized experimentally at 20 μA/V for the best signal to noise ratio while avoiding overload of the LNA input or output. The high-bandwidth mode is utilized to ensure the LNA can capture signals near 100 kHz. The noise specification for the LNA with these sensitivity and mode settings is 60 $\text{pA}/\sqrt{\text{Hz}}$.

The protection circuit, placed between the output of the receive coils and the input of the LNA, is used to avoid overloading of the LNA. The protection circuit (Fig. 5.7) consists of an analog CMOS switch and antiparallel Schottky diodes (Vishay BAT46-TR).

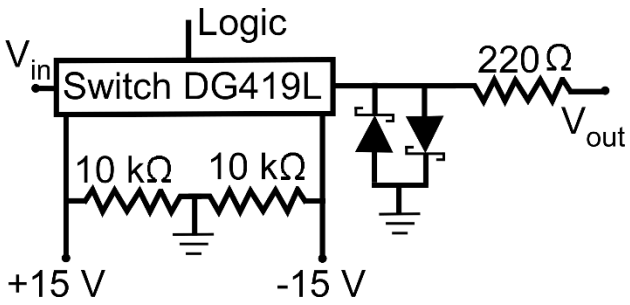

Fig. 5.7: Protection circuit for LNA with Schottky diodes.

The switch in the protection circuit is used to avoid overloading of the LNA input due to the mutual induction between the transmit coils and the receive coil during the transmit period. The switch logic is programmed in LabVIEW so that it is "off" during the transmit period and "on" during the receiving period. The Schottky diodes turn on limiting the maximum current to the LNA even if the switch fails in a short condition. A blank signal at the LNA was also used to avoid output overloading during the transmit period. This blank signal keeps the gain of the amplifier at 0 dB during the transmit phase and back to the 20 µA/V gain during the receiving phase.

A typical timing diagram for the transmit signal, switch logic and the blank signal is shown in Fig. 5.8. The transmit time and receive time utilized is chosen from 4 ms to 12 ms depending on the time constant of the received ringdown signal.

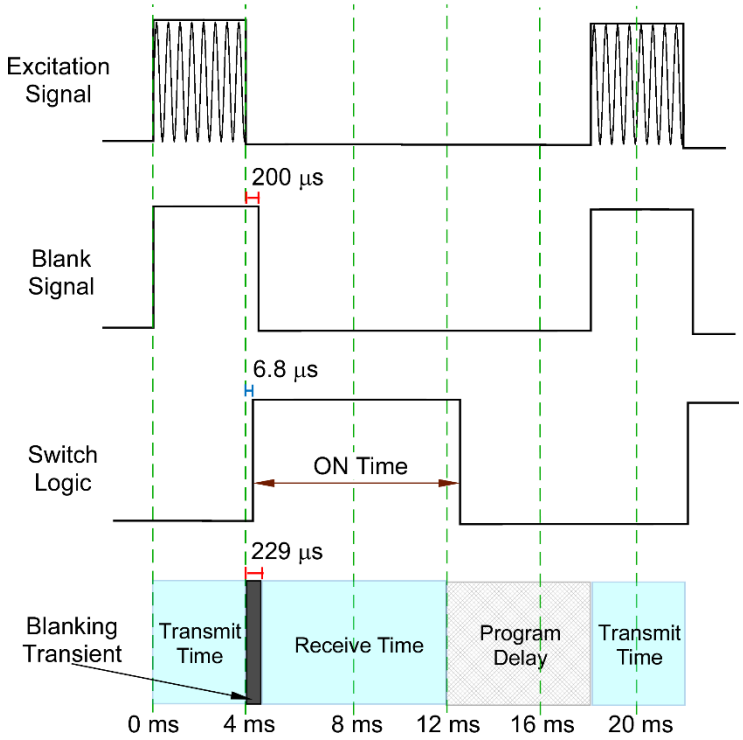

Fig. 5.8: Timing diagram for the signals generated.

The blank signal is delayed by 200 µs in order to avoid overload at the output of the LNA due to the ringdown of the transmit signal itself and the switching transients. The switch logic is delayed by 68 µs to avoid overload at the input of the LNA due to the ringdown of transmit signal that couples through the receive coil. These values are determined experimentally. The ON time of the switch logic varies from 8 ms to 10 ms and the program delay varies from 12 ms to 16 ms depending on the execution time of the LabVIEW code.

Finally, the amplified signal from the LNA is collected to a PC using a data acquisition device for further digital signal processing and display of results. This device collects the voltage data from the LNA at a 1 MHz sampling rate during the receive period. The collection of all the voltage data after the LNA helps to apply several signal processing techniques to improve the SNR and subsequently the wireless range. The signal processing steps are detailed in the next section.

5.3 Digital Signal Processing

The signal after the LNA is still noisy and extraction of any useful information requires further processing. A series of digital signal processing techniques were used to minimize the noise and recover the sensor signal. These techniques help to improve the SNR and an improved SNR allows improvement of the wireless range. The flow diagram of these techniques is illustrated in Fig. 5.9.

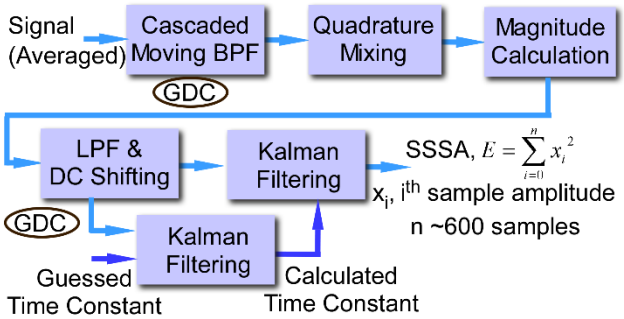

Fig. 5.9: Schematic of digital signal processing techniques implemented. SSSA is the Summed Squared Signal Amplitude and GDC is Group Delay Compensation.

The data acquired into the PC is divided into two segments of time. The first half, during which the ringdown signal will be the strongest, represents the sensor "signal"; while the second half is considered as the background "noise". This helps to evaluate the SNR by taking the real-time, frequency specific noise signature into account. For instance, Fig. 5.10 shows a typical signal response from the sensor during the measurement time. The first 12 ms represents the sensor signal while the remaining 12 ms represents the real-time noise in the system. Since the measurement is taken for 24 ms of time at a sampling rate of 1 million samples per second, each half of the data trace consists of 12,000 data points. The steps involved in the digital signal processing are listed in Table 5.1.

Table 5.1: Steps involved in digital signal processing.

Step 1	Averaging
Step 2	Switch peak removal
Step 3	Cascading moving bandpass filter
Step 4	Quadrature mixing and magnitude calculation
Step 5	Lowpass filter
Step 6	Selective Kalman filtering

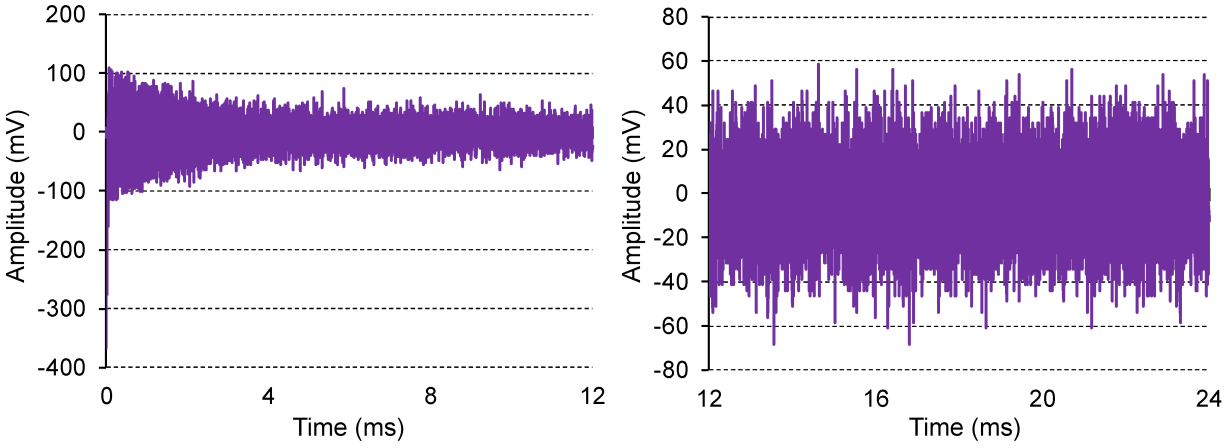

Fig. 5.10: Left – "Signal" data. Right – "Noise" data of the raw signal before DSP.

Step 1 - Averaging

The strength of white noise present in the signal can be reduced by taking an average of several data traces of the signal. In this step, 10 data traces are averaged over time in order to

reduce random white noise. This is illustrated in Fig. 5.11. More traces can be averaged to further reduce noise at the cost of total interrogation time.

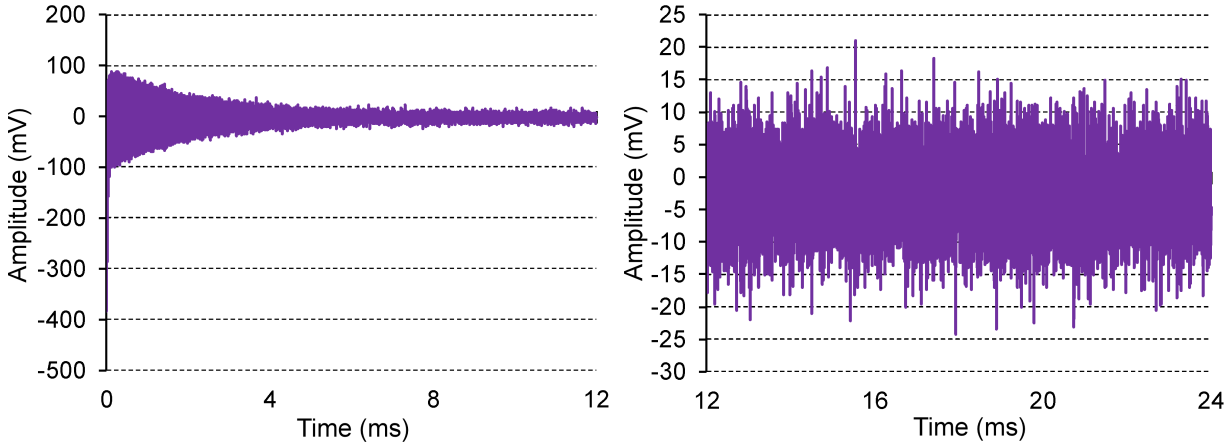

Fig. 5.11: Left – "Signal" data after step 1, averaging. Right – "Noise" data after step 1, averaging.

Step 2 – Switch peak removal

The distinct peak of amplitude 0.4 V (negative going) at the beginning of the signal is due to the switching that happens in the LNA when the blanking signal is toggled. This specific pulse lasts only for approximately 29 μs, and hence, 29 initial samples are removed from the data trace. This is illustrated in Fig. 5.12.

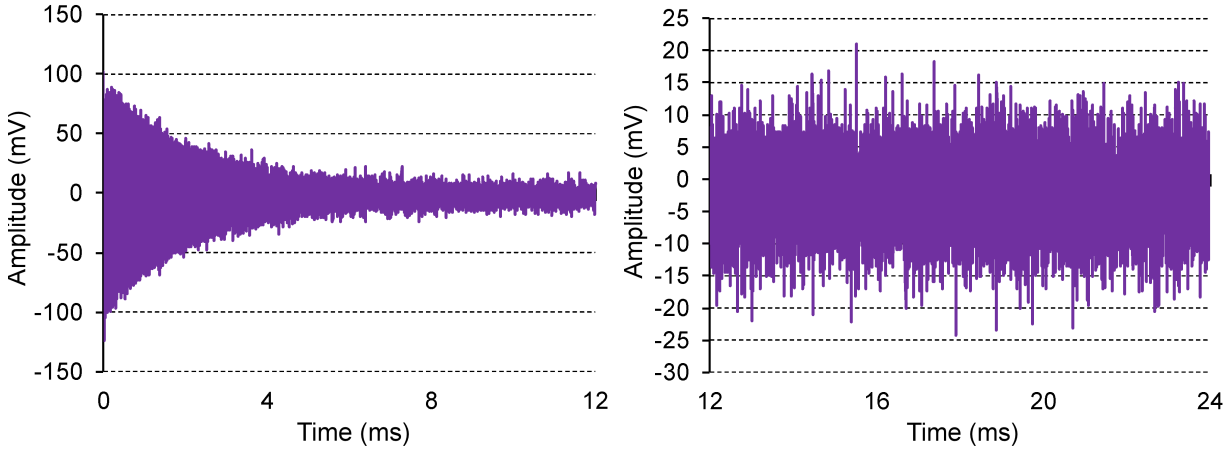

Fig. 5.12: Left – "Signal" data after step 2, removal of LNA gain toggling. Right – "Noise" data after step 2, removal of the peak from LNA gain toggling.

Step 3 – Cascaded moving bandpass filter

This step filters out high and low noise frequency – compared to the center frequency at each point in the sweep – using a narrow digital bandpass filter. The bandpass filter designed is a finite impulse response (FIR) filter. An FIR filter is a filter which has an impulse response of finite duration while an Infinite Impulse Response (IIR) filter continues to respond indefinitely. Because of this inherent nature, an FIR filter has guaranteed stability and an exactly linear phase. [Lit00, Eli13]. Hence, an FIR filter is chosen over an IIR filter. This property of having linear phase results in constant group delay for all frequency components of the signal while filtering. This is an important advantage in group delay compensation and for avoiding distortion of the signal. A linear phase FIR filter is designed using the Remez exchange algorithm to minimize the maximum error between the target frequency response and the designed filter frequency response. This error specification yields filters with equi-ripple or Chebyshev error behavior [Cet97].

A cascaded filter approach is used here by cascading two bandpass filters. Two bandpass filters with slightly offset bandpass frequencies are cascaded in order to achieve a narrow filter with the central frequency, C_f. The specifications of the bandpass/ stopband frequencies of these filters are listed in Table 5.2. The resulting number of taps, or filter coefficients, that are required to meet the bandpass filter specifications below is approximately 500.

Table 5.2. Frequency details of the filters implemented

	Bandpass Filter I	Bandpass Filter II	Cascaded Filter
Central frequency	$C_{f1}=C_f - 600$ Hz	$C_{f2}=C_f + 600$ Hz	C_f
Passband frequency 1	$C_{f1} - 1000$ Hz	$C_{f2} - 1000$ Hz	$C_f - 300$ Hz
Passband frequency 2	$C_{f1} + 1000$ Hz	$C_{f2} + 1000$ Hz	$C_f + 300$ Hz
Stopband frequency 1	$C_{f1} - 2000$ Hz	$C_{f2} - 2000$ Hz	$C_f - 1400$ Hz
Stopband frequency 2	$C_{f1} + 2000$ Hz	$C_{f2} + 2000$ Hz	$C_f + 1400$ Hz

The filters used in this step are moving filters, in the sense that the filter specifications are varied with respect to excitation frequency in real time. The central frequency (C_f) of the cascaded filter will be the excitation frequency. The magnitude response of these filters for one C_f is shown in Fig. 5.13, 5.14 and 5.15. The filtered "signal" and "noise" data is shown in Fig. 5.16.

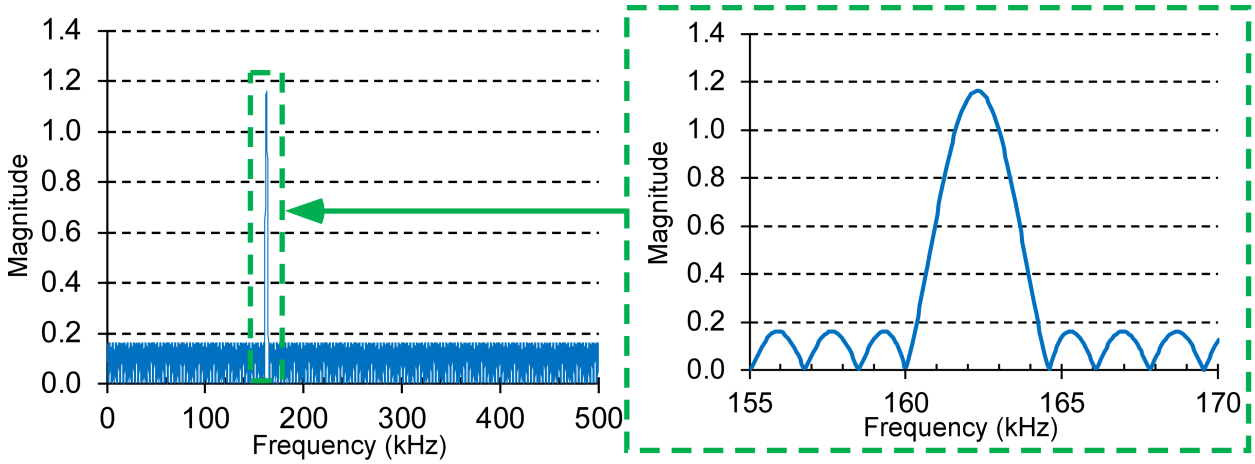

Fig. 5.13: Magnitude Response of BPF I (C_{f1} =162.3 kHz).

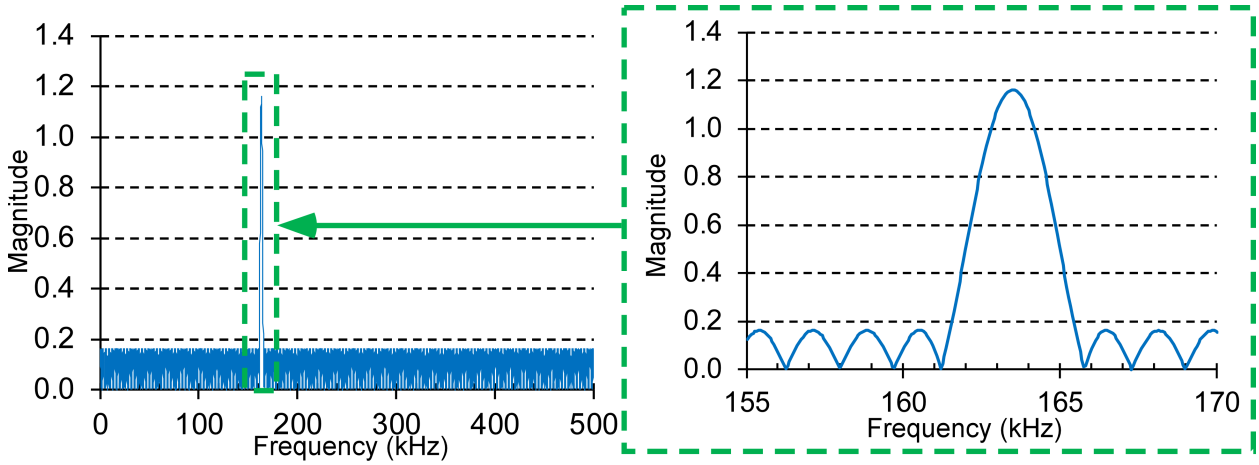

Fig. 5.14: Magnitude Response of BPF II (C_{f2} =163.5 kHz).

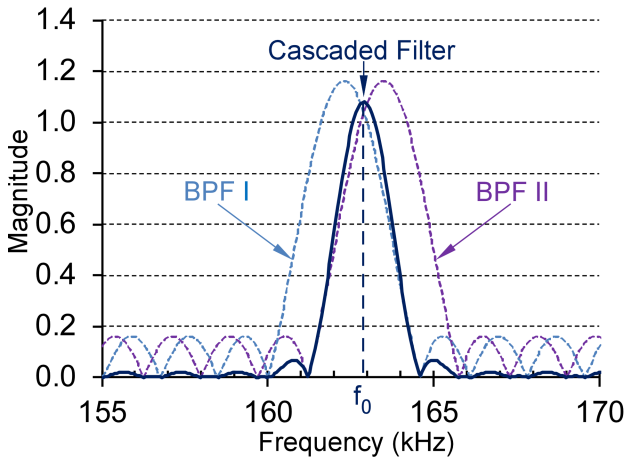

Fig. 5.15: Cascaded FIR filter magnitude response at (C_f=162.9 kHz).

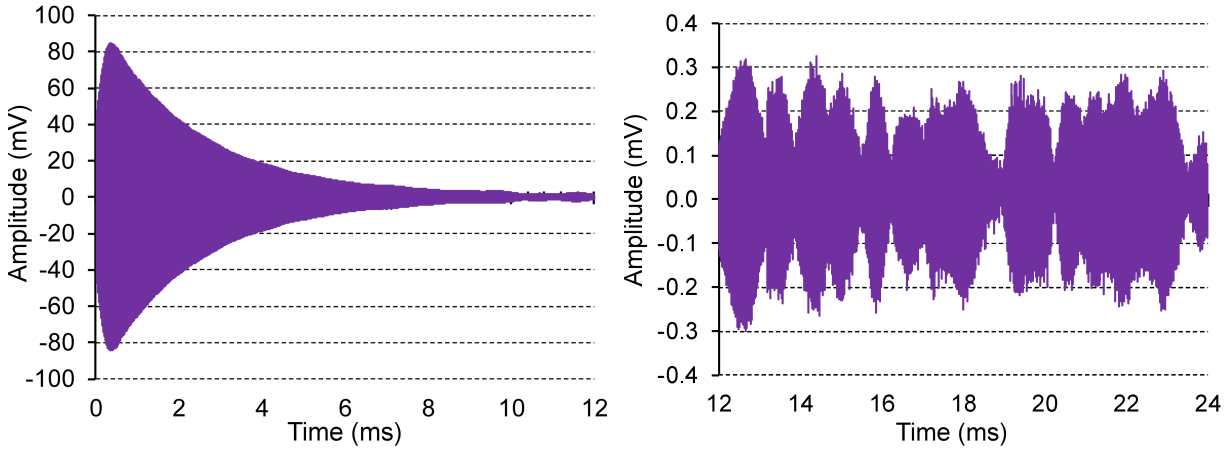

Fig. 5.16: Left – "Signal" data after step 3, cascaded band pass filtering. Right – "Noise" data after step 3.

Step 4 – Quadrature mixing and magnitude calculation

The filtered signal from the bandpass filter is then quadrature mixed by multiplying with two sinusoid signals in quadrature phase relation at the excitation frequency and magnitude of the mixed signals are calculated in order to isolate the frequency component of interest as shown in Fig. 5.17. If V_r is the filtered signal with sensor resonant frequency ω_r and V_s is the excitation signal at frequency ω_s:

$$V_r = v(t)\sin(\omega_r t) \tag{5.9}$$

$$V_s = v_a \sin(\omega_s t) \tag{5.10}$$

After mixing the signals will be:

$$X = 0.5v(t)v_a \cos(\omega_r - \omega_s)t - \cos(\omega_r + \omega_s)t \tag{5.11}$$

$$Y = 0.5v(t)v_a \sin(\omega_r - \omega_s)t + \sin(\omega_r + \omega_s)t \tag{5.12}$$

Magnitude *M*, is calculated by:

$$M = \sqrt{X^2 + Y^2} \tag{5.13}$$

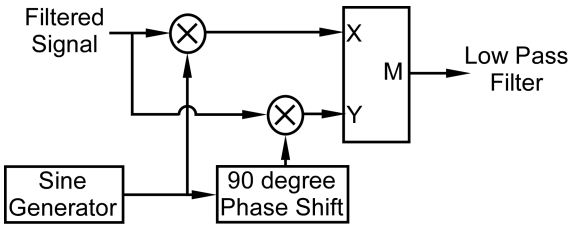

Fig. 5.17: Quadrature mixing and calculation of magnitude.

The magnitude of the quadrature mixed signals is shown in Fig. 5.18.

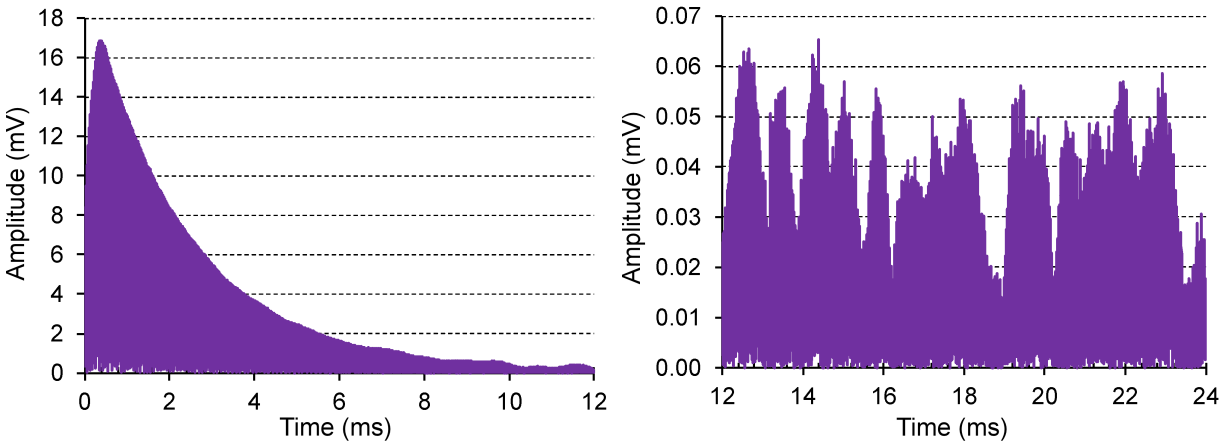

Fig. 5.18: Left – "Signal" data after step 4, quadrature mixing (amplitude). Right – "Noise" data after step 4, quadrature mixing (amplitude).

Step 5 – Lowpass filter

In this step, high-frequency components after the quadrature mixing are removed by using a low pass filter. This process isolates the signal "envelope". This low pass filter is also an equiripple filter designed using the Remez exchange algorithm with passband frequency of 1 kHz and stopband frequency of 3 kHz. The magnitude response of the filter is shown in Fig. 5.19. The traces after this step are shown in Fig. 5.20.

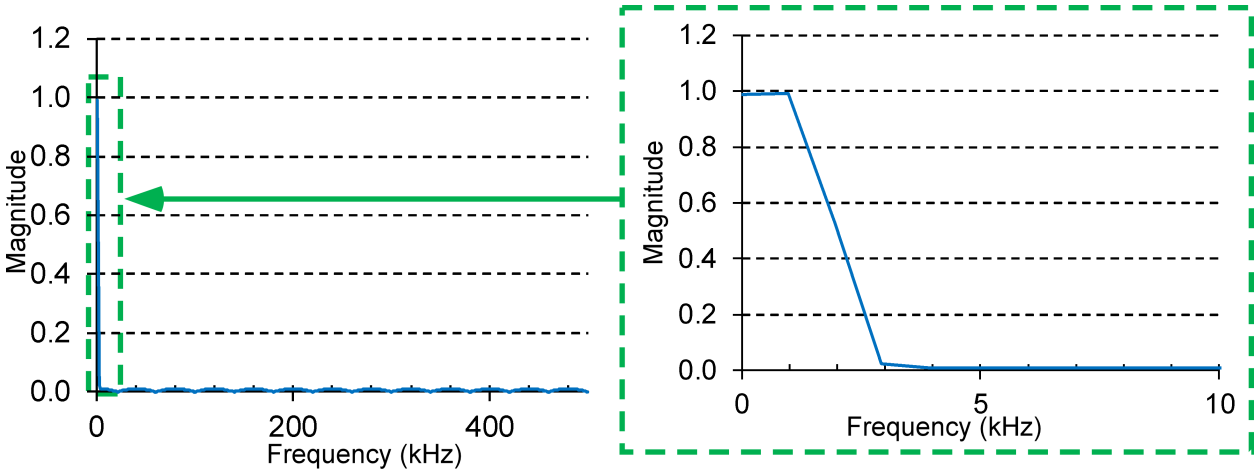

Fig. 5.19: Magnitude response of the Lowpass FIR filter used in step 5.

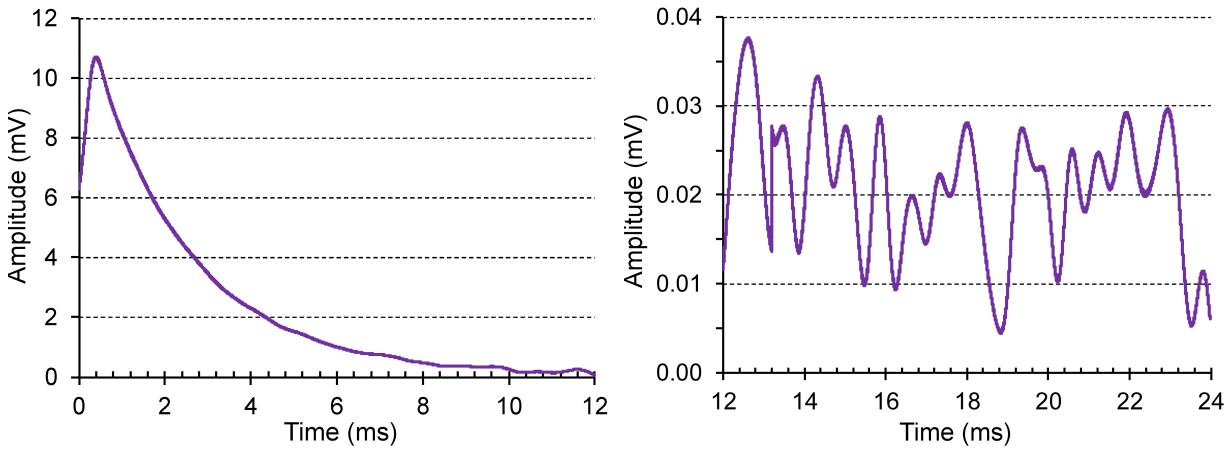

Fig. 5.20: Left – "Signal" data after step 5, low pass filtering. Right – "Noise" data after step 5.

Group Delay Compensation: Implementation of the filters in step 3 and step 5 results in an inherent group delay. It is important to compensate for this effect in order to recover the signal efficiently. Group delay (GD) is defined as [She05]:

$$\tau = -\frac{d\theta}{d\omega} = -\frac{1}{2\pi}\frac{d\theta}{df} \tag{5.14}$$

where θ is the phase response of the filter and *(dθ/df)* is the slope of the unwrapped phase response of the filter. For a filter with a linear phase response, the slope will be constant and thus the group delay is constant. Flow diagram for calculation of GD is shown in Fig. 5.21.

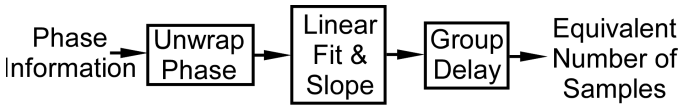

Fig. 5.21: Flow diagram on the calculation of group delay.

Unwrapping the phase response followed by linear fitting and calculation of slope is illustrated in Fig. 5.22 for the LPF used in step 5.

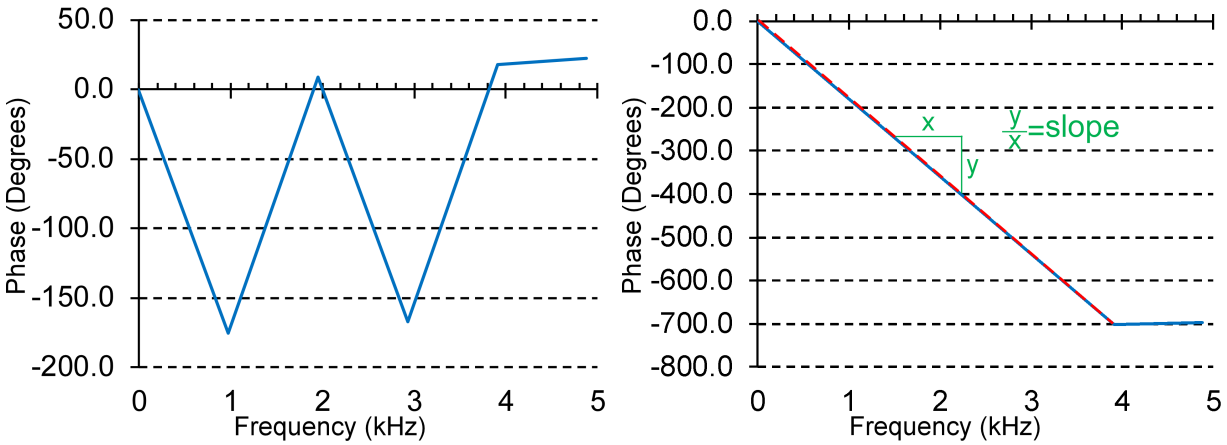

Fig. 5.22: Phase response of the LPF (Left). Unwrapped phase response (Right) to facilitate calculation of group delay.

The number of samples delayed due to the group delay can be calculated by multiplying group delay with the sampling rate. Group delay compensation is achieved by zero padding the same number of samples at the end of original signal before filtering and deleting the same number of

samples from the beginning of filtered signal [Bor10]. This is illustrated in Fig. 5.23, 2.24 and 5.25 for a typical case for BPF II.

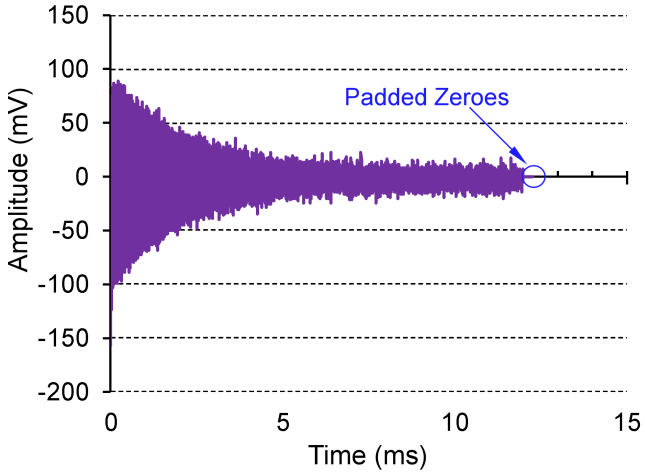

Fig. 5.23: Signal with zero padded data at the end of the data trace.

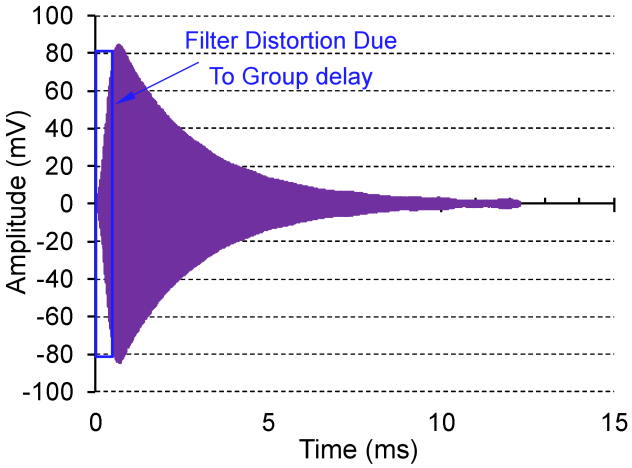

Fig. 5.24: Filtered data using BPF II after zero padding.

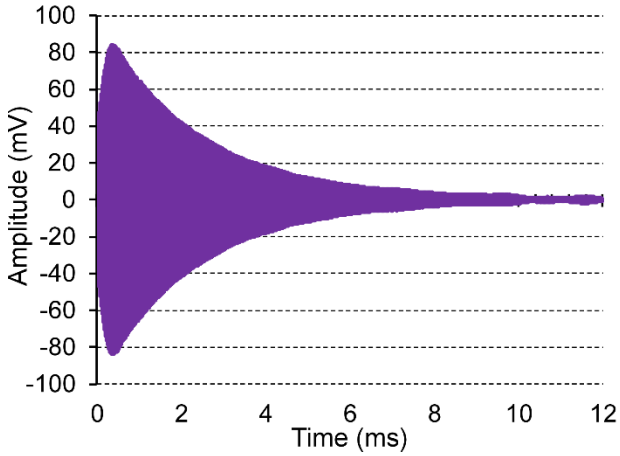

Fig. 5.25: GD compensated data after removing the initial samples.

In the case of the LPF, padding a constant value can also help to minimize the distortion due to filtering. Constant padding similar to the zero padding and in this case extra data points are added at the beginning of the data trace. In this data trace, the first element 6.4 is duplicated and padded in the beginning. The data trace is also padded with zeroes at the end as shown in Fig. 5.26. It was experimentally found that this constant padding along with the zero padding helps in minimizing the distortion of the signal while using the filter and helps to recover the sensor signal more efficiently.

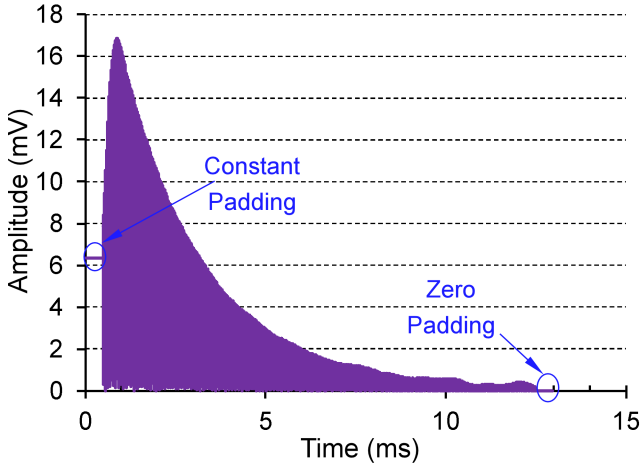

Fig. 5.26: Constant padding along with zero padding for LPF.

Step 6 - Selective Kalman Filtering

By using a Kalman filter (KF), the state of a process (system) can be estimated by using the observation, knowledge of the system behavior and noise, and a set of mathematical equations [Kal60, Grw11, Chu89]. This technique helps to reduce the error in the measurements of the system by predicting the expected response. Good knowledge of the expected response of the sensor signal measured, as well as an ability to characterize the noise at every frequency (by measuring over a longer period of time than the ringdown signal is substantial), helps to implement the KF efficiently. The KF is used allowing the noisy ringdown signal to be smoothed and noise to be suppressed substantially. The response of a magnetoelastic sensor excited via a time domain decoupled signal – and after the envelope extraction described in the processing steps 1 through 5 – is a first order exponentially decaying signal. This known fact that the system response is a ringdown signal is exploited here in implementing the KF. Based on the general Kalman filtering principle explained in the appendix, it is implemented here for one-dimensional data.

A couple of steps are performed before implementing the KF to ensure its efficient usage. First, there is a DC component, equivalent to the average noise amplitude, is present in the observed measurements after quadrature mixing. This is eliminated by subtracting the average noise value from the "signal" and "noise" data sets. This brings the noise to randomly oscillate around zero instead of a constant value. The signal and noise after this DC shifting are shown in Fig. 5.27.

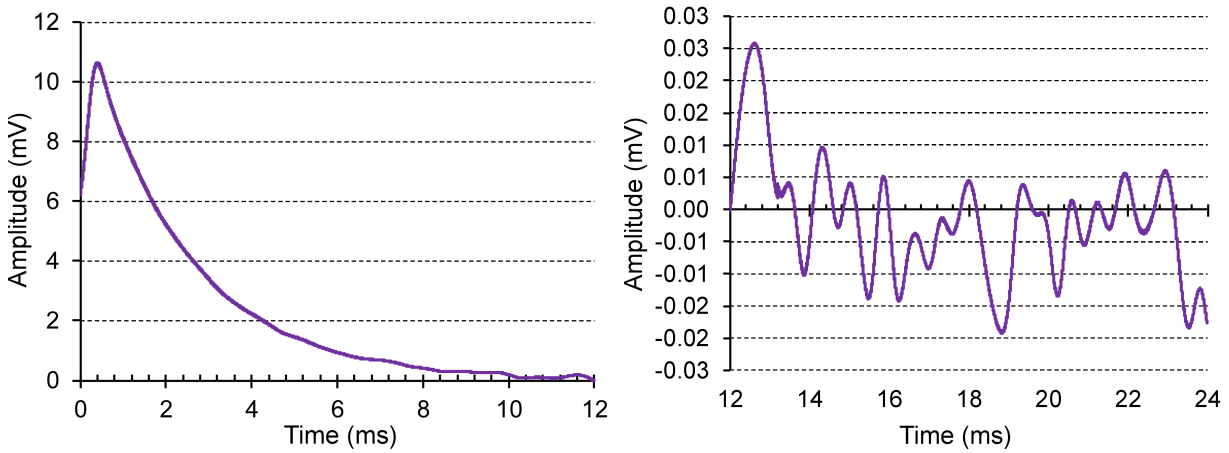

Fig. 5.27: Results of DC shifting. Left – Signal data. Right- Noise data.

Secondly, the ringdown envelope before Kalman filtering has distortion due to filter transients from the previously implemented bandpass cascaded filter and low pass filter. The response in this portion of the signal is not well matched with a first order ringdown, so the Kalman filtering is not advantageously applied to this portion of the signal. Distorted initial samples were set aside prior to the execution of the Kalman filter as shown in Fig. 5.28. The number of samples over which this transient distortion takes place is consistent from measurement to measurement and is a characteristic of the digital filters used.

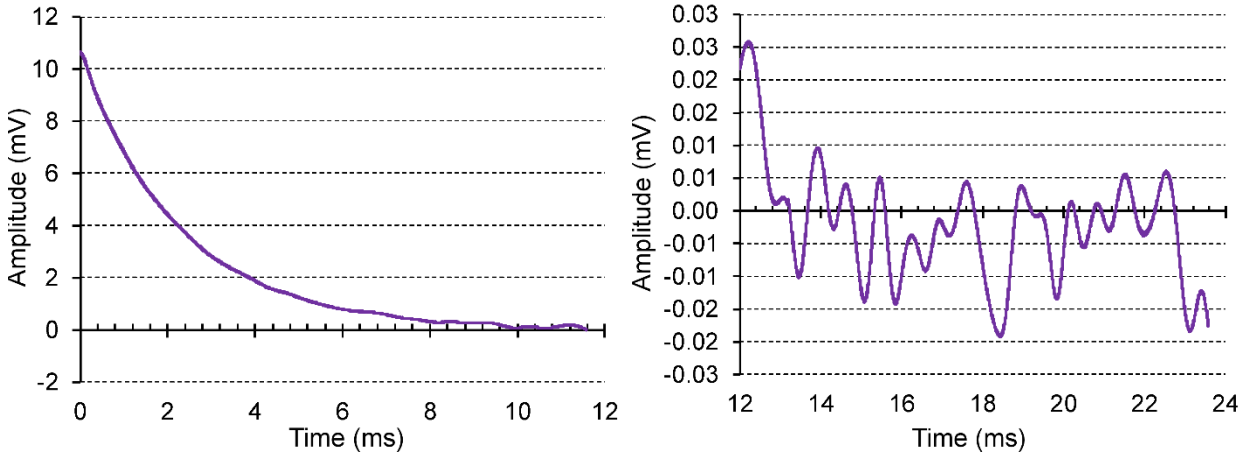

Fig. 5.28: Distorted initial samples were set aside prior to Kalman filtering. Left – Signal data. Right- Noise data.

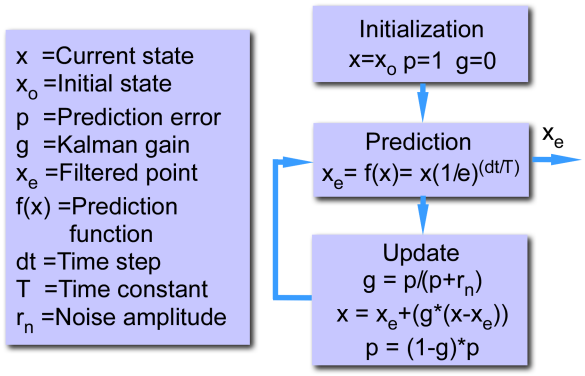

Fig. 5.29: The flowchart illustrating the Kalman filter.

The flow diagram of the KF implemented is illustrated in Fig. 5.29. The current state *x* for the first point is initialized as the first point of the envelope after step 6. The state covariance and Kalman gain are initialized as one and zero respectively, representing full confidence in the prediction function. The filtered point x_e predicted using the prediction function *f(x)* which represents typical exponential decay. The time step, *dt*, is 1 µs since it is the sampling interval used in the data acquisition. *T* is the time constant of the exponential decay of the envelope of the ringdown. *T* is guessed initially from experience and then calculated from an extra Kalman filtering step as shown in Fig. 5.9 and used in real time. Measurement noise covariance r_n is calculated as the variance of the noise signal around its average value. This is calculated for each frequency during the sweep. This is included in the LabVIEW code via Mathscript TR module. These steps are repeated for all the data points to obtain the filtered signal. The Kalman filtered signal and noise are shown in Fig. 5.30.

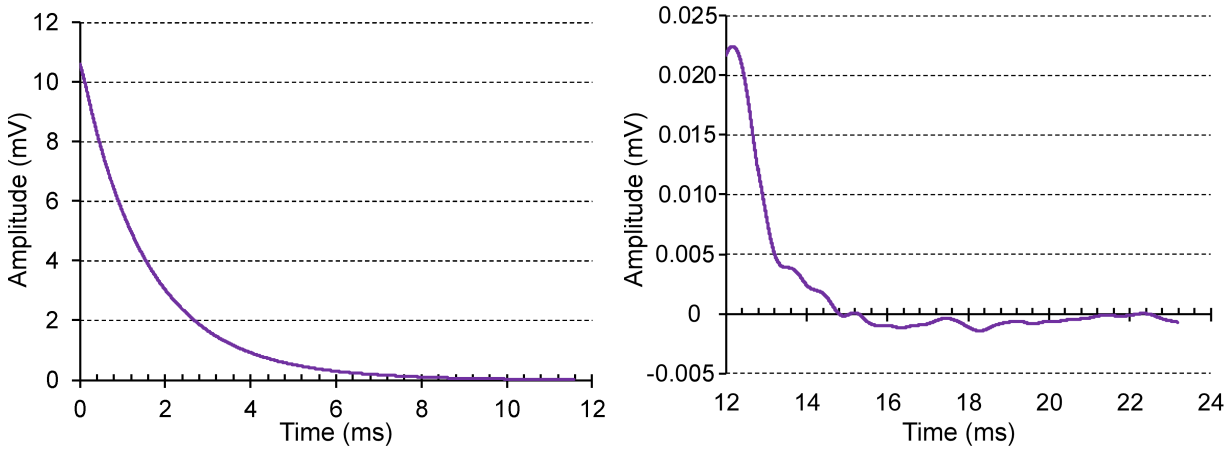

Fig. 5.30: Left – Signal data after step 6, Kalman filtering. Right – Noise data after Kalman filtering.

Summed squared signal amplitude (SSSA): Since the receiving signal is ringing down in nature, the signal strength is predominant in initial cycles and the signal strength will be well above the noise. To benefit from all the time that signal is above the noise, the total energy is calculated instead of just the maximum amplitude of the ring-down signal. Using Parseval's theorem [Agr93], the summed squared amplitude, E is defined as:

$$E = \sum_{t=0}^{n} |x_t|^2 \tag{5.15}$$

where x_t = amplitude of the signal at sample t after DSP. The summed squared signal amplitude, E_s is calculated for the ring down signal for each frequency as:

$$E_s = \sum_{p=0}^{n} |x_p|^2 \tag{5.16}$$

where x_p are the samples (after DSP) taken when the sensor is excited. The summed squared noise amplitude, E_n is also measured for noise by not exciting the sensor for real-time noise signature:

$$E_n = \sum_{q=0}^{n} |x_q|^2 \tag{5.17}$$

where x_q are the samples (after DSP) taken when the sensor is not excited. Signal to noise ratio (SNR) is defined as:

$$SNR = \frac{E_s}{E_n} \tag{5.18}$$

This is illustrated in Fig. 5.31.

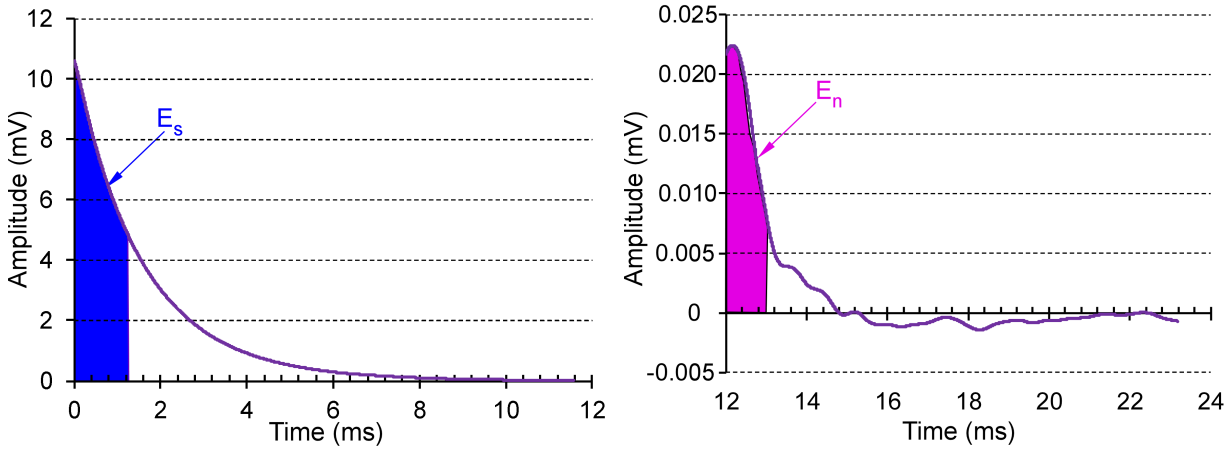

Fig. 5.31: Illustration of calculation of summed squared signal amplitude.

The value of n is optimized by calculating the E_s and E_n for all possible values of n at the resonant frequency and then evaluating which value of n results in the highest SNR. This helps to evaluate the SNR by taking real-time noise signature into account.

5.4 Experimental Results

Experiments were conducted using the interrogation module to demonstrate the effectiveness of the module in overcoming the challenges focused on this work. A ribbon sensor is interrogated using the module on benchtop, *in vitro*, and *in situ*. The ribbon sensor (12 mm × 1 mm) is fabricated from 28 µm thick Ni/Fe foil (MetglasTM 2826MB) and assembled in a biliary stent using custom-made 3D package. Magnets (Arnokrome 5, 60 µm thick) were integrated onto the 3D package for required DC bias.

Benchtop experiments

The benchtop experiments were conducted to demonstrate the utility of the interrogation module for interrogating a magnetoelastic sensor. In real situations, after the implantation of sensor integrated stent in a patient, the stent position and orientation can vary according to the position and orientation of the bile duct which can differ from patient to patient. So, these benchtop experiments investigate the dependence of the signal strength on the angle between the longitudinal axis of the sensor and the AC excitation field and the dependence of the sensor position relative to the transmit/receive coil. For these experiments, the belt coil (transmit and receive coils) was wound around a 20 cm diameter cardboard barrel, and the sensor packaged in a stent was placed at the center of the belt coil in air.

For the first set of experiments, the angle between the longitudinal axis and the exciting AC field was varied, and the change in signal strength was observed as shown in Fig. 5.32.

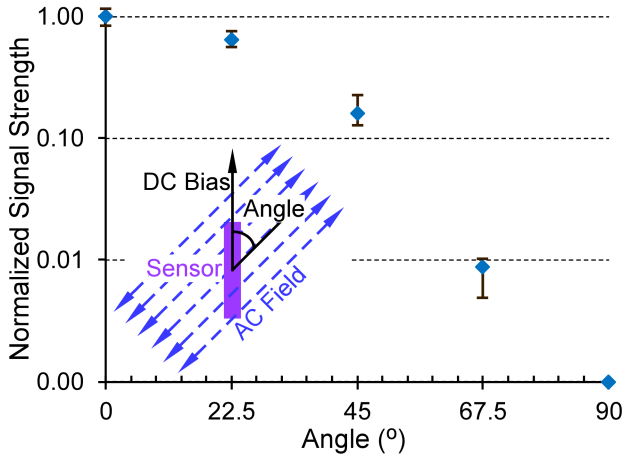

Fig. 5.32: Change in signal strength with the angle of the sensor with respect to the axis of the coil.

The signal strength was reduced significantly to 12% for the case where the sensor was inclined 45° with respect to the axis of the interrogation coils. For the 67.5° inclined case, the signal was reduced to 1%. The decrease in the signal strength is close to an exponential with the increase in

angle between the sensor axis and the transmit/receive coil axis. These results indicate that the magnetic field generated by the sensor is mostly in the direction of the axis of the coil and hence any deviation from it reduces the signal strength considerably. This indicates the importance of having the longitudinal axis of the sensor aligned with the axis of the belt coil.

In the next set of experiments, the position of the sensor was varied for several axial/radial distances from the center of the belt coil and the variation in signal strength was noted as shown in Fig. 5.33. For this test, the longitudinal axis of the sensor and the axis of the barrel were parallel.

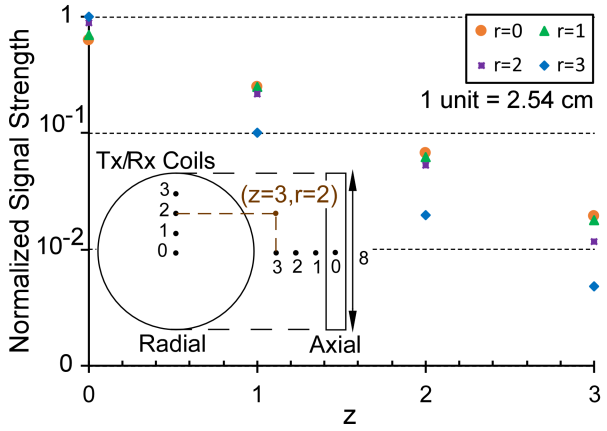

Fig. 5.33: Change in signal strength with the position of the sensor with respect to transmit/receive coil. *r*, and *z* represents the radial and axial distance respectively from the center of the coil (similar to the cylindrical coordinate system).

For r =0 and z =3, the signal dropped 1.5% compared to r =0 and z =0. Similarly, as the sensor position is moved away from the center of the coil along the axis of the coil, the signal strength reduced exponentially. At the same time, radial position of the sensor shows higher signal strength when it is closer to the transmit/receive coil for the case z =0 but vice versa in other cases. Also signal strength reduced to 4% when the coil size is increased from 8" (20 cm) to 12" (30 cm). This is illustrated in Fig. 5.34.

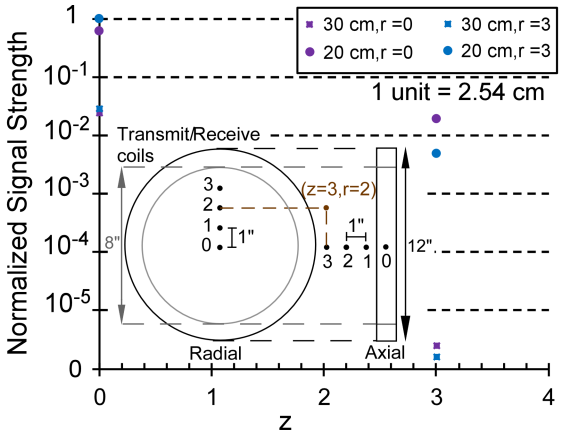

Fig. 5.34: Change in signal strength when 30 cm diameter transmit/receive coils are used instead of 20 cm diameter coils. The signal strength with the position of the sensor with respect to transmit/receive coil is also showed. r, and z represents the radial and axial distance respectively from the center of the coil (similar to the cylindrical coordinate system).

That is a 25-fold decrease in signal strength for 1.5-fold increase in wireless range. In summary, the sensitivity of the interrogation module depends on the characteristic pattern of the excitation field as well as the sensor field. More excitation results in more signal strength but at the same time, the sensor signal needs to be coupled with the receive coil to detect the signal. The best-case scenario here is to have the sensor close to the transmit/receive coils in the same plane of the coil, i.e. no axial distance.

In vitro experiments

In vitro experiments were conducted to demonstrate the utility of the interrogation module in the scenarios similar to the clinical situation that can be imitated in the lab. These experiments were focused on immersing the sensor packaged in the stent in fluids with varied viscosity and imitating the stent occlusion.

The sensor integrated stent was immersed successively in water, oil, and then occlusion of the stent was imitated using gelatin. For the fully occluded case, the sensor integrated stent was immersed in a gelatin mix. Gelatin mix is prepared by mixing the gelatin powder with water (7 g in 72 mL DI water) and allowed to cure in the refrigerator (4ºC) for 30 mins. This imitates a fully

occluded stent case. The partially occluded stent is simulated by partially cleaning the gelatin out of the stent mechanically using a metal rod of 1.5 mm diameter. The frequency response in each case is shown in Fig. 5.35. The resonant frequency and the quality factor for various cases from the *in vitro* experiments are illustrated in Fig. 5.36.

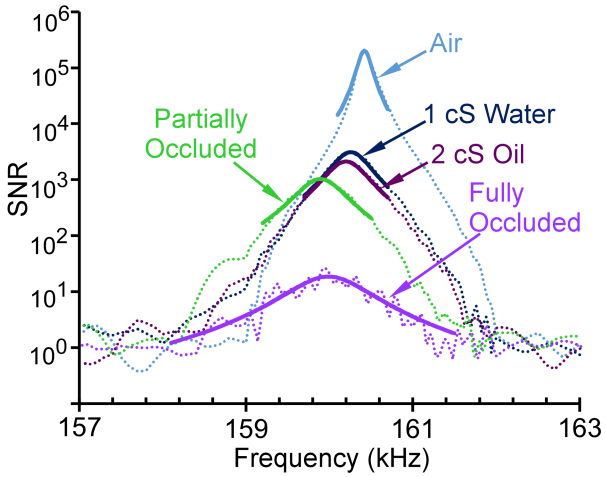

Fig. 5.35: Frequency response from the *in vitro* experiments in air, in 1 cS water, in 2 cS oil, partially occluded with gelatin, fully occluded with gelatin.

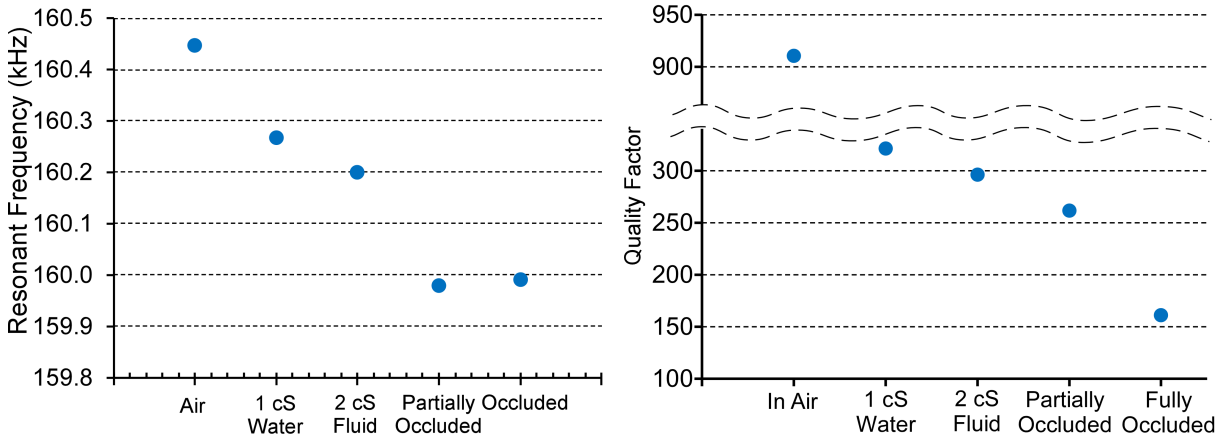

Fig. 5.36: Resonant frequency and quality factor for various cases from the in vitro experiments.

The SNR, the resonant frequency and the quality factor of the sensor depends on the viscosity of the medium as well as the mass deposition on the sensor. The SNR decreased drastically by 99.5% while immersed in water compared to signal strength in air due to the drastic

change in the viscosity of the medium. However, the reduction in SNR from 1 cS water to 2 cS fluid was 34%. In the implanted situation, the sensor in stent will be immersed in bile solution. Bile majorly constitutes water and the viscosity is closer to 1 cS [Jia18b]. The interrogation module could detect the signal from the sensor with an SNR of 3020 at a wireless range of 10 cm for the case of 1 cS water.

The immersion in the fluid was also manifested in a shift in resonant frequency and a drop in quality factor. The resonant frequency in air ≈160.44 kHz is shifted by ≈180 Hz when the sensor packaged in stent was immersed in 1 cS DI water. The resonant frequency was shifted by ≈240 Hz when the sensor integrated stent was immersed in 2 cS oil. For a partially occluded stent, the resonant frequency was shifted by ≈460 Hz while it was ≈480 Hz for the fully occluded case. These results indicate that the resonant frequency shifts with respect to mass loading as well as the viscosity of the medium. The quality factor drops by ≈520 from air to 1 cS water and ≈18 from 1 cS water to 2 cS oil. When the stent was fully occluded with the gelatin the quality factor dropped by ≈150, the SNR dropped by 99.67% and the resonant frequency was shifted by ≈450 Hz compared to case where the sensor is in 1 cS water. This significant change in quality factor and the shift in frequency illustrates that the sensor can indicate occlusion in the stent clearly.

In situ experiments

In situ experiments were conducted to demonstrate the utility of the interrogation module *in situ*. For *in situ tests*, a laparotomy was performed on a euthanized swine, and the bile duct was located. A sensor integrated stent was placed into the bile duct, and bile was injected into the stent to mimic the real environment. Interrogation coils were placed around the porcine carcass as shown in Fig. 5.37. The coil had an approximate elliptical shape with minor and major diameters of 18 cm and 23 cm, respectively. The frequency response in terms of SNR from the *in situ*

experiment is shown in Fig. 5.38.

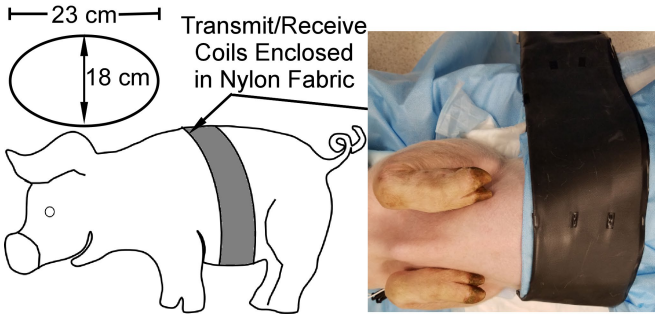

Fig. 5.37: Schematic of the coil set-up in situ and the photo of the coil belt around the porcine subject.

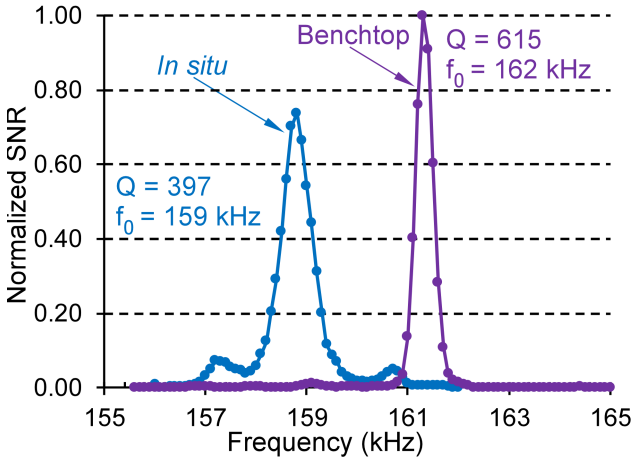

Fig. 5.38: Comparison of frequency response from benchtop experiment in the air and in situ experiment. The normalization factor is 508.

The resonant response was detected successfully using this interrogation module with an implanted wireless range of ≈10 cm with an SNR of 376. Compared to previous interrogation systems reported, these results represent a 1.3-fold increase in wireless range and a 54-fold increase in SNR for a 40% reduction in sensor length.

In vivo experiment

The magnetoelastic sensor (8.25 mm × 1 mm footprint) was fabricated by bonding one 28 μm thick Metglas 2826MB layer with two 60 μm Arnokrome 5 mass loads. The bond was achieved with an Au/In transient liquid phase approach (From Chapter 3). The mass loads were magnetized to provide the required DC bias**.** The sensor was then coated with Aluminum Oxide and Parylene for corrosion protection and biocompatibility. The sensor must be packaged for protection during endoscopic deployment. A custom-made 3D-printed polymer-metal package (M3 crystal resin reinforced by Nitinol wires) was used for protection and for integrating the sensor to the stent (see Chapter 4).

The test protocol was approved by the University of Michigan IACUC (protocol #6901). The subject of the *in vivo* test was a female domestic swine (25 kg). Before implantation, the swine was sedated, and an intravenous catheter was placed into an accessible vein on the ear. Pre-operative analgesia was administered through this catheter. After that, the swine was intubated and placed on isoflurane anesthesia. Vitals of the subject were continuously monitored using temperature monitor, pulse oximetry, and electrocardiogram. A heat source (water-circulated heating pad) was also used to keep the vitals normal.

The biliary stent was implanted in the bile duct by a standard endoscopic procedure. The endoscope (Olympus TJF Type Q180V side-viewing duodenoscope), was guided through the mouth and esophagus of the subject, to the stomach, and finally to the duodenum. The side viewing camera at the end of the endoscope was used to locate the position of the biliary orifice. Saline was injected through the endoscope to clear the camera view as necessary. Once the biliary orifice was located, a guidewire along with the catheter was placed through the bile duct. A radiographic dye was injected through the catheter into the bile duct. The dye allows the internal structures to be

observed via radiogram (X-ray, fluoroscopy) to confirm the cannulation of the bile duct. The introducer assembly, along with the loaded stent, was then loaded onto the back end of the guidewire and fed through the endoscope. Once the proximal end of the stent was aimed at the biliary orifice, the introducer assembly is used to push the stent into the bile duct. The fluoroscopic image after implantation is shown in Fig. 5.39.

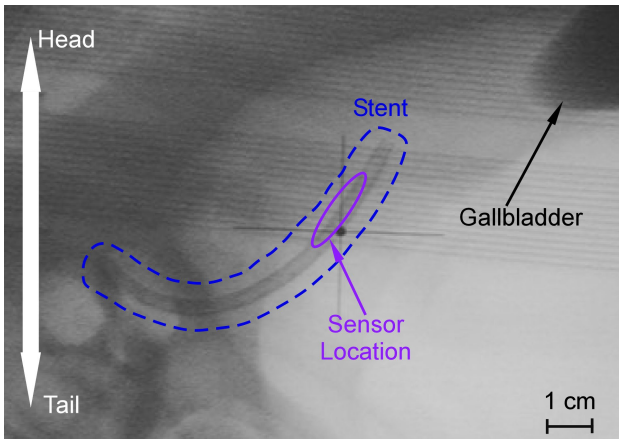

Fig. 5.39: Fluoroscopic image of the stent after implantation in the swine.

Next, for the interrogation, the transmit/receive coils were wrapped around the subject, as shown in Fig. 5.40. The frequency response of the sensor *in vivo* compared to the response acquired on the benchtop is illustrated in Fig. 5.41.

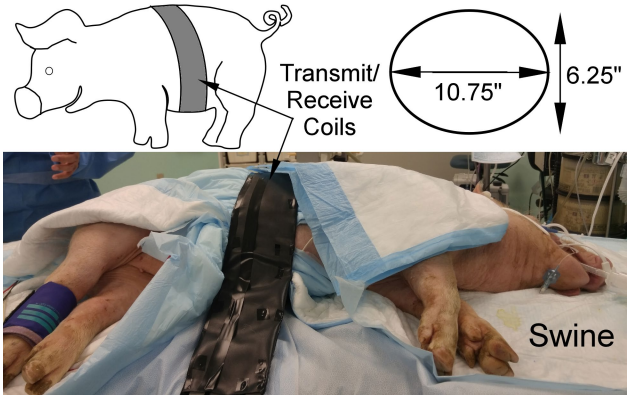

Fig. 5.40: Interrogation in progress. Interrogation coils are wound around like a belt on the swine subject *in vivo*.

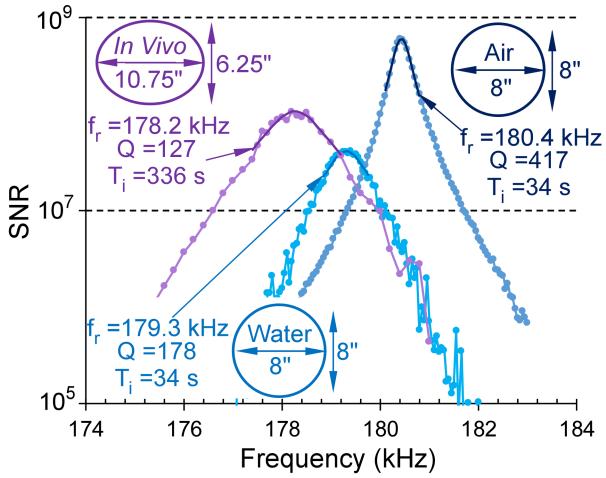

Fig. 5.41: Sensor response *in vivo*, benchtop in air and water.

The quality factor decreased from 178 (in water) to 127 (*in situ*), and the resonant frequency shifted from 179.3 kHz (in water) to 178.2 kHz (*in situ*). The SNR of this measurement was ≈10^8. The coil dimensions *in vivo* were slightly different from benchtop experiments due to the swine anatomy. The interrogation times (T_i) for benchtop tests were ≈34 s, while that of the *in vivo* was ≈336 s. The decrease in quality factor and the resonant frequency is due to the sensor being immersed in bile rather than water; bile is more viscous than water. These results indicate the sensitivity of the sensor with respect to the medium in which the sensor is immersed.

The coils were then placed with an axial offset of ~5 cm with respect to the sensor position to mimic the clinical situation where the coils could be misplaced with respect to the position of the sensor. The sensor response, in this case, is plotted in Fig. 5.42.

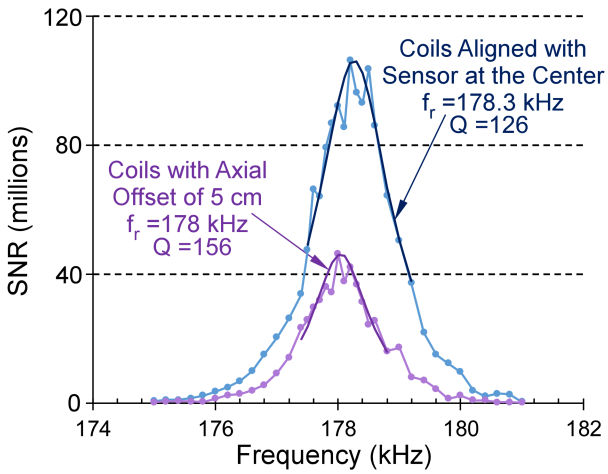

Fig. 5.42: Sensor response in vivo with aligned coils and with an axial offset ~5 cm, interrogation time ≈340 s.

The measured resonant frequency only changed by 0.3 kHz (0.17%) while the quality factor changed by 30. The interrogation time was ≈340 s. Even the misaligned coils could detect the signal with an SNR of ~4×10^7.

Next, the interrogation coil size was increased to mimic the increased waistline of a larger patient. The coil size was increased by inserting an inflated airbag between the subject and the coil as shown in Fig. 5.43. The frequency response in these cases is also shown in Fig. 5.44.

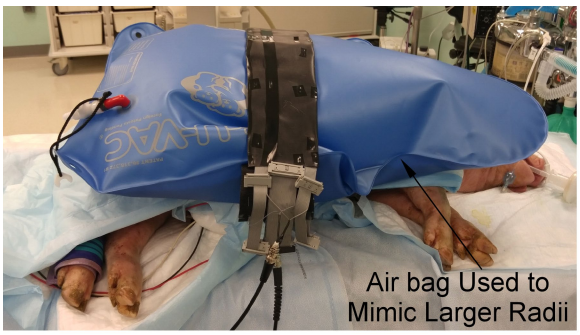

Fig. 5.43: Inflated airbag is inserted between the subject and the coils for mimicking larger waist patients.

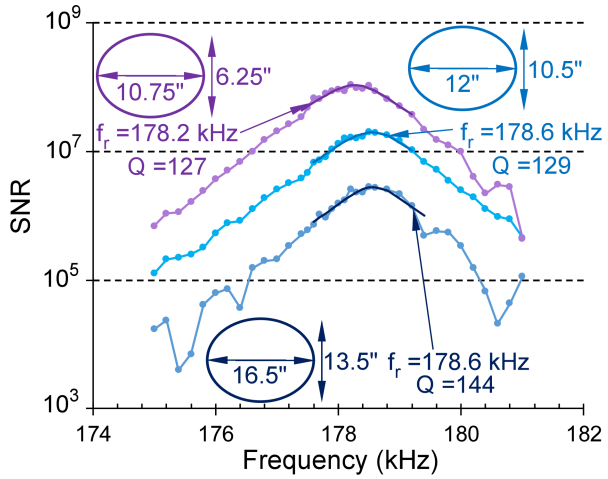

Fig. 5.44: Sensor response for increased coil diameters mimicking patients with a larger abdomen, interrogation time ≈336 s.

Increasing the coil dimensions from 10.75” × 6.25” (major and minor elliptical diameters, 27.3 cm × 15.9 cm) to 12” × 10.5” (30.5 cm × 26.7 cm) decreased the SNR to 25% of the previously measured value, but the resonant frequency stayed within 0.4 kHz with a change in the quality factor of only 2. A further coil dimension increase to 16.5” × 13.5” (41.9 cm × 34.3 cm) resulted in a decrease of SNR to 15% of that measured with the initial coil dimensions. The shift in resonant frequency was only 0.4 kHz with a change in the quality factor of 15. The interrogation time was ≈336 s. The system could characterize the sensor with an error of ±0.17% in resonant frequency and ±10.6% in quality factor. This indicates the consistency in the results measured using this interrogation system, despite shifts in orientation and size of the coils.

5.5 Summary and Conclusions

In this chapter an interrogation module for the application of magnetoelastic sensor for biliary stent monitoring is discussed. Experiments were conducted to demonstrate the utility of this module on the benchtop, *in vitro, in situ* and *in vivo*. The benchtop experiments investigate the effects of sensor alignment as well as position with respect to the transmit/receive coils in the

interrogation module. It was found that the sensor must be aligned axially as well as positioned closer to the coils for maximum sensitivity. Further *in vitro* were conducted mimicking the real scenario of occlusion of the stent. Sensor signals from these experiments indicated that the occlusion of the stent could feasibly be related to frequency shift and change in quality factor and SNR. Finally, successful *in vivo* experiments were conducted detecting signals from a magnetoelastic sensor implanted in a live animal. The system could detect the signal at a wireless range of ≈17.1 cm, and a signal to noise ratio of $\approx 10^6$ was achieved with an interrogation time of 336 s. These are the first reported signals from a magnetoelastic stent-integrated sensor implanted in a live animal. Successful *in vivo* interrogations with this system indicate the clinical utility.

Chapter 6: Conclusions and Future Work

This chapter summarizes the conclusions drawn from the efforts in the development of the two magnetoelastic systems in this work: (i) a magnetoelastic system for mitigation of glaucoma valve encapsulation and (ii) a magnetoelastic system for biliary stent monitoring. Major contributions to the general field of knowledge from these efforts are also summarized here. Finally, potential improvements for these systems are identified as future work.

6.1 Summary of This Work

Two magnetoelastic systems were developed for implantable biomedical applications, and they were investigated in detail and demonstrated *in vitro*, *in situ,* and *in vivo.* The challenges in the implanted module were identified and addressed to improve the implant robustness – both in terms of mechanical structure and signal strength. The interrogation challenges for these implanted devices were surmounted, resulting in enhanced performance of these systems in their respective applications. The *in vitro*, *in situ* and *in vivo* experiments proved the robustness of the systems and their clinical utility.

6.1.1 Magnetoelastic system for mitigation of glaucoma valve encapsulation

The development and demonstration of the magnetoelastic system for mitigation of glaucoma valve encapsulation included investigation of the actuator-mounted glaucoma valve (implanted module) as well as the interrogation module. Regarding the implanted module, the challenges in terms of mounting the actuator on to the valve and corrosion protection were tackled.

The interrogation module was developed utilizing a physical domain decoupling approach and optimized hardware implementation for improved signal acquisition from the implanted device. *In vitro* experiments performed with the system demonstrate a signal-to-noise ratio of ≈140. *In situ* experiments, performed with the actuator-integrated valves implanted in porcine eyes, achieve a signal to noise ratio of 3-6. These are the first recorded acoustic signatures through tissue from a magnetoelastic device in an implanted environment. *In vivo* experiments were performed and the results combined with the *in situ* results indicated that the magnetoelastic system does not adversely affect the health of the animal and can feasibly provide sufficient wireless range after implantation.

6.1.2 Magnetoelastic system for biliary stent monitoring

The development and demonstration of the magnetoelastic system for biliary stent monitoring included investigation of the sensor/package design and fabrication and its integration to the stent (implanted module) as well as the interrogation module. The challenges tackled in terms of the implanted module include sensor miniaturization to reduce the implant footprint considerably by a novel sensor design. The challenges towards packaging the stent for protection during deployment were also overcome and a novel hybrid sensor package was designed and fabricated. Finally, the challenges in terms of interrogation for improved signal acquisition were addressed, and a module was developed with careful hardware integration and implementation of several signal processing techniques.

One of the challenges for the implanted module was sensor miniaturization. A novel miniaturized, self-biased sensor with preserved frequency was designed and fabricated. The sensor structure employed targeted mass-loading to achieve these features. The sensor was characterized *in vitro* for detection of the sludge accumulation, and sensor sensitivity was analyzed. The ratio

of the shift in resonant frequency to the quality factor was found to be well-correlated to the occlusion. The receiver-operator characteristic for this parameter indicated an accuracy of 97.84% for zero false positive rates, with a detectable threshold of 50% decrease in flow rate through the stent.

The implanted module was also tailored to provide sensor protection during deployment. The introducer used during endoscopic deployment can damage the sensor; hence, protective packaging is a must. Also, the stent undergoes tight curvature during deployment, which can damage the sensor, and the implanted stent is also under curvature imparted by the inherently curved bile duct. These challenges were addressed using a hybrid package which consisted of a polymer structure reinforced with highly elastic Nitinol wires. The bending tests carried out on the packaged-sensor-instrumented stent proved that this hybrid package overcomes these challenges.

The effect of the packaged sensor itself on the occlusion dynamics was also investigated by carrying out *in vitro* tests, including culturing of bacteria in bile and flowing the mixture through both package-instrumented stents and normal stents. Non-inferiority statistical tests conducted on these results indicated that the instrumented stent is non-inferior to the normal stent in terms of the occlusion time for a p-value <0.05.

The interrogation module for biliary stent monitoring was developed to include a time domain decoupling approach along with careful hardware implementation and a series of digital signal processing techniques. These features addressed the challenges of signal feedthrough, wireless range, and clinical utility. Finally, the complete magnetoelastic system was successfully implemented in an *in vivo* demonstration. The instrumented stent was implanted in the bile duct of a live pig via endoscopy. At a wireless range of $\approx$17.15 cm, a signal to noise ratio of $\approx 10^6$ was achieved with an interrogation time of 336 s. These are the first reported signals from a

magnetoelastic stent-integrated sensor implanted in a live animal via endoscopy.

6.2 General Contributions to the Field of Knowledge

Several techniques developed in this work can be potentially extended to other general applications as well. The techniques used in developing the implanted module for these systems and also the interrogation modules can be extended to improving the system-level performance of any transducer-based systems.

The novel magnetoelastic sensor introduced in this work can potentially be used in any applications that require a miniaturized wireless sensor for sensing mass loading/viscosity. A functionalized sensor can extend its potential to immunosensing applications and sensing of other physical parameters. Specifically, the concept of targeted mass loading for self-biasing the sensors while preserving the resonant frequency is attractive for miniaturized wireless sensor applications. The preservation of resonant frequency despite miniaturization may also enable new anti-theft tags that can tag smaller items or be applied more discretely while leveraging the same 58 kHz interrogation infrastructure already in place. The fabrication technique of In-rich transient liquid phase bonding can also be extended for bonding materials in general. The hybrid package developed in this work introduces the use of a combination of materials with different mechanical properties in the context of applications requiring challenging deployment demands.

With respect to the development of interrogation modules, the optimized hardware implementation and the associated signal processing techniques can be extended to test/characterization modules in general for characterizing various types of transducers. For example, the interrogation module developed for the mitigation of glaucoma valve encapsulation can be used in part for characterizing any transducer that emits acoustic signals. Also, the

interrogation module developed for biliary stent monitoring can be used for communicating with any magnetoelastic transducer at a greater wireless range. The signal processing techniques like Kalman filtering used in this work can be extended to any signal data set for improving the signal to noise ratio.

In vitro experimental method mimicking the occlusion in stent along with the sensor characterization results are reported for the first time. This type of approach could enable more rapid stent technology development in general.

6.3 Future Work

6.3.1 Magnetoelastic system for mitigation of glaucoma valve encapsulation

Improvement in interrogation performance of the acoustomagnetic module introduced in this work (Chapter 2) in terms of wireless range is a possible future endeavor. This will allow extending the use of the same interrogation module for *in vivo* experiments as well with a better controlled feed-back method. This feedback enabled module will allow better understanding of the encapsulation dynamics and potential improvements in the system. Also, more *in vivo* experiments in the future can give more information about the effect of the liquid actuation and subsequent mitigation of the encapsulation.

6.3.2 Magnetoelastic sensor for biliary stent monitoring

The sensor introduced in this work performed with a signal to noise ratio of $\approx 10^6$ at a wireless range of ≈17.15 cm. This indicates that there is a huge potential for further sensor miniaturization. Several miniaturized sensors, each with a different resonant frequency, can be deployed at critical locations along the inner surface of the stent, and this will allow for the detection of sludge build-up and occlusion locally. Adjusting the mass loading carefully also

allows for controlling the resonant frequency. A combination of these can potentially result in development of a sensor array for measuring the entire inner lumen of the stent. The development of miniaturized sensors tailored to specific operating frequency ranges as well as an array of these sensors integrated with the stent will be a part of future work. The hybrid coating investigated in this work could protect the sensor upto a week or so without any obvious performance decline. But the signal performance declined for longer period of time due to corrosion. An improved coating method must be explored based on the reported results for corrosion protection for extend time period.

6.3.3 The in-stent hybrid package for biliary stent monitoring

The in-stent hybrid package could protect the sensor during deployment, but still the signal was attenuated due to the transfer of stresses during deployment to the sensor. Further modifications to the hybrid package in terms of improving its performance is a potential area for future work. A network of packages for the array of sensors mentioned in the previous section can also be investigated. Another prospect is in completely avoiding the need for a package by modifying the stent itself. A smart stent that has a network of sensors mechanically embedded could avoid the use of the package altogether and simplify the implanted module.

6.3.4 The interrogation module for biliary stent monitoring

The interrogation module developed in this work for biliary stent monitoring could improve the performance compared to previous modules used for this application. However, there is still room for further performance enhancement in terms of customizing the hardware and including advanced signal processing techniques. The development of a custom magnetoelastic interrogation system, including both analog/digital parts replacing the research-grade hardware used in this work is a potential future work.

The analog part will mainly include a PCB, consisting of voltage regulators, a buffer amplifier, a buffer inverter IC switch, and a low noise amplifier. The PCB will replace the existing buffer amplifier, switch/protection circuit, and the LNA. This will effectively reduce the complexity and cost of the analog circuitry and associated power supplies while increasing the robustness and potentially the performance. The design will enable a single device to replace several previously used components, thus reducing the usage of cables and increasing the usability and potentially the signal clarity due to enhanced power supply regulation and band-specific analog filtering.

The digital portion of the hardware will focus on digital signal processing program and hardware implementation with a single-board computer, Direct Digital Synthesizer (DDS), and analog-to-digital converter (ADC). The digital signal processing program written in LabVIEW can be translated to other languages as necessary, including advanced digital signal processing techniques. The single-board computer will run on its specific language, the DDS will act as a sine wave generator, and the ADC will help to read out the signal amplified by the analog part. The single-board computer will need to have real-time control and timing capabilities for synchronized excitation and detection. A replacement for the currently used NI-PXIe (a combination of sinewave generator, data acquisition, and signal processing device) must provide the following functions: analog to digital conversion, transmit waveform generation, data storage, digital signal processing, logic control, etc.

Ideally, the combination of the products of the analog portion and digital portion would result in an inexpensive, self-contained device that is able to drive the coils and measure the response from a magnetoelastic sensor. This new interrogation module will help to move the current research to the market. The module would no longer need expensive research-grade

hardware (LNA, NI-PXIe, multiple DC supplies). The new module would be self-contained and manufacturable in volume at a reasonable price.

6.3.5 The *in vitro*, *in vivo* and clinical experiments for biliary stent monitoring

The *in vitro* experiments with the magnetoelastic system discussed in Chapter 4 proved the non-inferiority of the instrumented stent with respect to a non-instrumented stent in terms of occlusion time. Also, these experiments showed the change in resonant characteristics of the sensor, specifically the quality factor and resonant frequency, after occlusion as well. However, continuous monitoring of the stent is required for a better understanding of the occlusion development inside the stent. The future work on *in vitro* experiments can follow the same procedure of bacterial culture and flow set-up but must develop real-time methods for quantifying the occlusion and compare the sensor response. The flow rate through the stent for a constant pressure head could be one way for quantifying the occlusion, but it may also destructively affect the occlusion itself. Observation of the change in sensor characteristics over time could be an alternative way to understand occlusion development in detail.

The *in vivo* experiments mentioned in Chapter 5 achieved the first recorded magnetoelastic system demonstration targeted towards biliary stent monitoring from a live animal. Continuous and long-term monitoring of the implanted sensor could provide more information on occlusion development as well as the health effects of the implanted module for a live animal. Several of these *in vivo* experiments will be good precursor set of experiments before clinical use in humans.

6.3.6 Safety of magnetoelastic materials during Magnetic Resonance imaging (MRI)

MRI is a generally used diagnostic tool in body tissue imaging. Conductive or magnetic materials implanted inside the body pose a risk of electromagnetic heating due to exposed

radiofrequency magnetic fields from the MRI tool. This radiofrequency heating can be either due to eddy current formation or hysteresis loss. Preliminary FEA simulations have indicated that the rise in temperature due to eddy current heating is well within the International Electrotechnical Commission (IEC) guidelines [Pep15a]. More FEA simulations for the specific designs of the actuator and sensor used in this work must be done to ensure that this issue is within the IEC limits.

Appendix A: Double layer mass loaded sensors

As discussed in this Chapter 3, miniaturizing the sensor is desirable to minimize the obstruction to the bile flow through the stent, to reduce the impact of the sensor on the longitudinal bending stiffness of the stent, and for enabling the use of multiple sensors along the length of the stent for spatial resolution of sludge accumulation. However, miniaturizing the sensor drastically reduces the signal strength. A decrease in sensor length to 75% of the initial value results in a drastic reduction in the signal strength to 12% of its initial value, and a length decrease to 50% of the initial value results in a signal reduction to 3.2% of its initial value [Jia18b]. This significant reduction in signal strength poses a serious challenge in miniaturizing the sensors.

One of the strategies to overcome this challenge is to use double layer sensors, formed by tightly bonding two single-layer sensors. Bonding two single layer sensors effectively doubles the material and is expected to result in double the signal strength (and quadruple the signal energy). Bonding the layers together, rather than simple stacking of the layers, is necessary in order to ensure that any mass loads on the top layer are mechanically coupled to all layers. Au/In Eutectic bonding is used to bond the sensor layers. Layers of Au and In was deposited on to the sensor (Metglas 2826) by physical vapor deposition and electroplating, and the Metglas layers were bonded under compression at 200^{o}C in a vacuum environment. Detailed fabrication steps are illustrated in Fig 4.1. Aggressive cleaning between each layer deposition (e.g. plasma stripping)

and to maintain clean bonding surfaces by carrying out as much of the process as possible within the Lurie Nanofabrication Facility cleanroom.

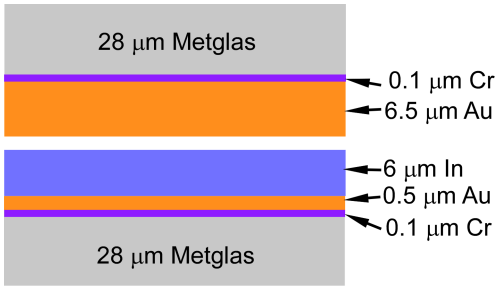

Fig. A1: Schematic of layers involved in double layer sensors with Au-In TLP bond

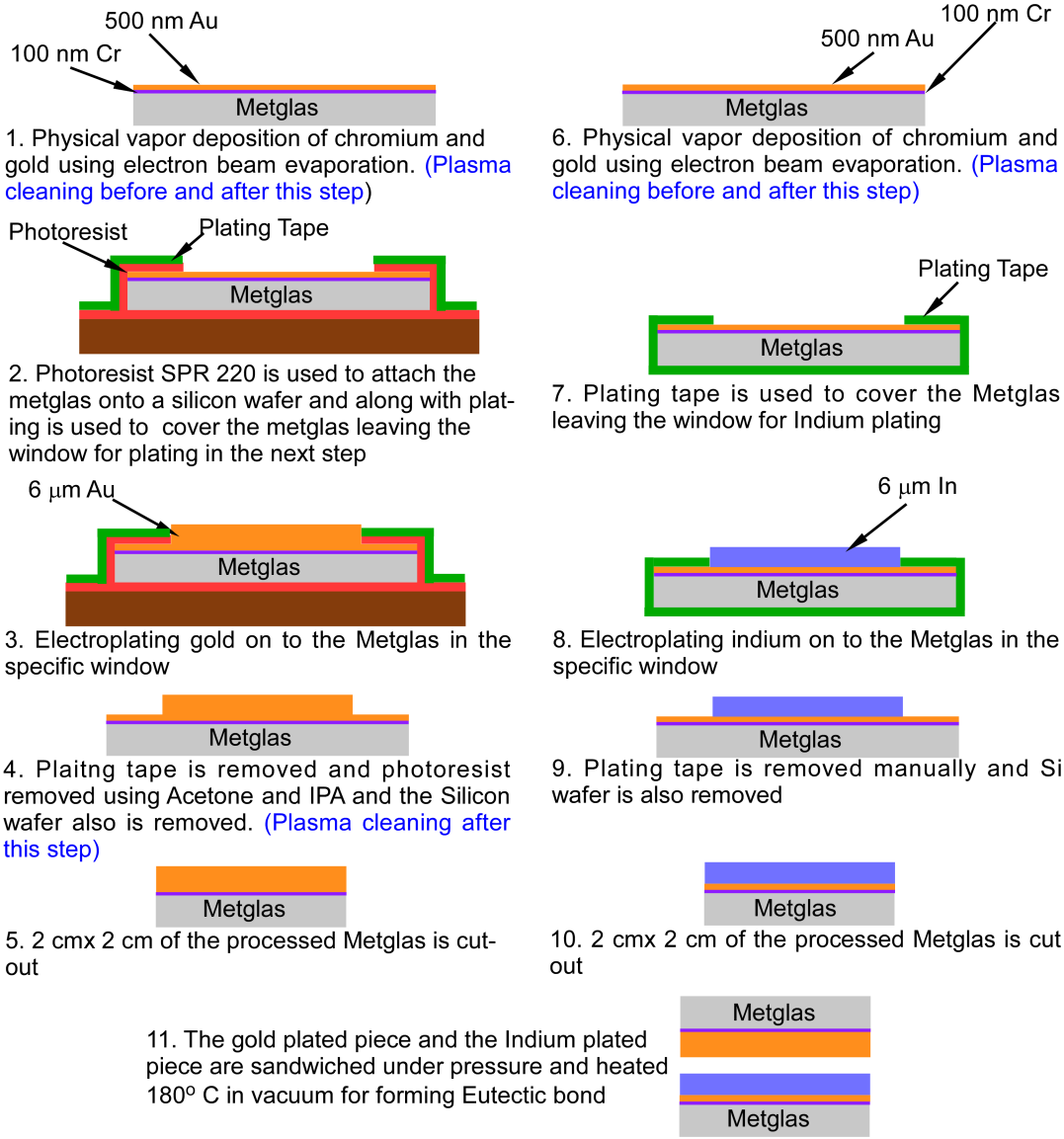

Fig. A2: Fabrication steps of double layer sensors using Au-In TLP bond

Six double layer sensors (8.25 mm x 1 mm were characterized (8d1-8d6). The setup used for characterization is shown below. The coil was made of 10 turns each for transmitting coil as well as receiving coil. The coil diameter is 3.5 cm, and the width of the coil was 2.2 cm for total 20 turns. Labview code 'BiliaryStentSensor_v3' is used. Excitation amplitude is varied with frequency to keep the excitation current through the transmit coils is consistent, 43 mA (peak to peak) in this case. The Impulse time and ring down time used are 4 ms each. Commercial Helmholtz coils were used for DC bias (conversion factor 1 A≈1 G). The interrogation system used is shown in the figure below. Note that the BPF on LNA was kept 'none' for these experiments.

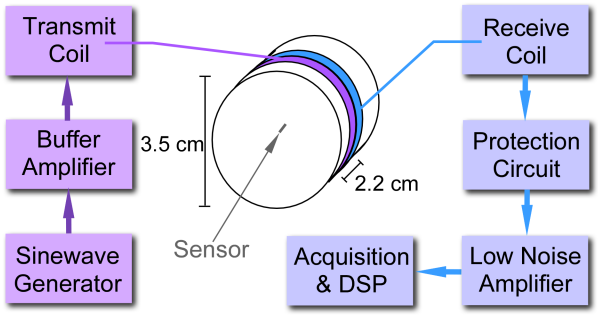

Fig. A3: Interrogation system used for characterization

Mass loaded double layer sensors were fabricated and characterized. These sensors (8.25 mm x 1 mm) have mass loads (1 mm x 1 mm) at the two ends. The sensor is fabricated from double layer Metglas (Total thickness of 68 µm), and the mass at the two ends are made of double layer Arnokrome 5 (300 Oe coercivity, mass thickness of 150 µm). The following sections discuss experiments with mass loaded double layer sensors of 1 mm long mass loads and 1.5 mm long mass loads.

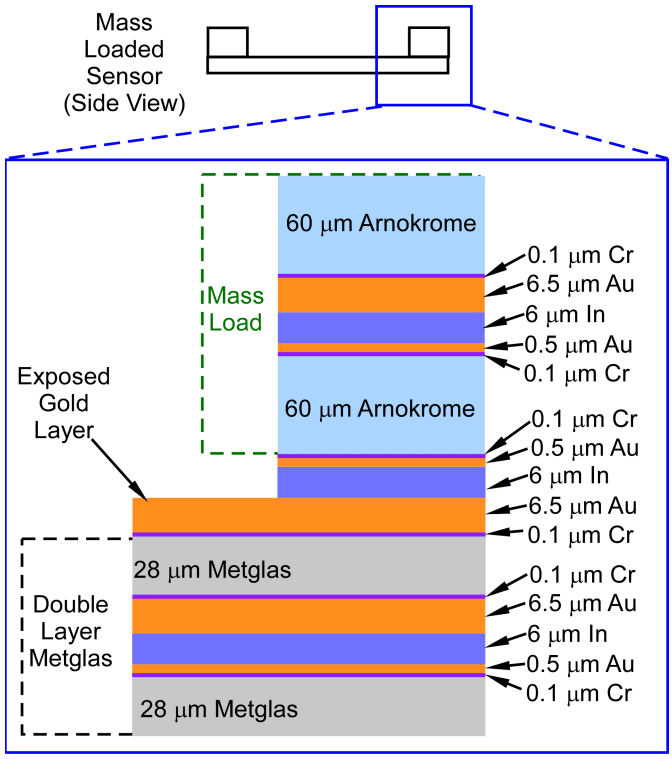

Fig. A4: Schematic of layers involved in the fabrication of mass loaded double layer sensor using Au-In TLP bond

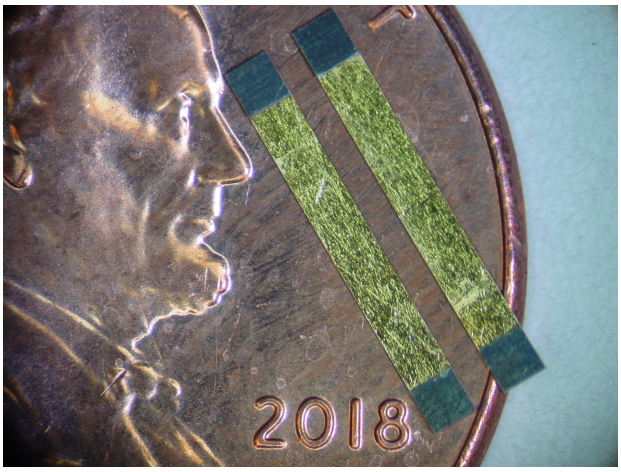

Fig. A5: Fabricated mass loaded double layer sensors using Au-In TLP bond

Seven mass loaded double layer sensors (total dimension: 8.25 mm x 1 mm with mass 1 mm x 1 mm; double layer Metglas and double layer Arnokrome 5 300 Oe coercivity) were characterized. The same setup is used for characterization (Fig. A3). After characterization with the DC bias applied with Helmholtz coils, the mass-loaded resonators were magnetized along their

length with the ASC Scientific Impulse Magnetizer (long coil, 100 V impulse, corresponding to ~10 kGauss peak flux density). The resonators were characterized again in the same setup, without any bias applied by the Helmholtz coils. Note that the Helmholtz coils were still in the setup and connected to the same power supply, just that the current from the supply was turned off (It was observed to be the same as when the supply was set to 0 A).

Two sensors of longer mass loads were tested in this part (total dimension -9.25 mm x 1 mm with mass 1 mm x 1.5 mm; double layer Metglas and double layer Arnokrome 5 300 Oe coercivity). Same interrogation module described in Fig. A3 is used. For a complete comparison, Single layer sensors were also fabricated and characterized. Table 1 lists the complete set of observations of single layer sensors (8s1 through 8s5) with highest signal strength, resonant frequency and quality factor (from plot) for each sensor at their optimized DC bias, along with observations from the previous shorter mass loaded double layer sensors (8m1 through 8m8), double layer (8d1, 8d2) and longer mass loaded double layer sensors (9m1, 9m2).

Table A1: Summary of observations on sensor characterization.

	On Metglas side				On mass side			
	DC bias (G)	Peak Signal (V^2)	Resonant Frequency (kHz)	Quality Factor	DC bias (G)	Peak Signal (V^2)	Resonant Frequency (kHz)	Quality Factor
8m1	17.1	0.0147	161.55	269	17.1	0.0123	161.5	269
	Self	0.00117	162.4	232	Self	0.0039	162.25	324
8m2	13.8	0.000664	161	201	17.1	0.000175	161.25	215
	Self	0.00054	161.7	231	Self	0.00074	161.8	270
8m3	13.8	0.000012	162.3	74	13.8	0.000048	161	196
	Self	0.00001	162.1	74	Self	0.00001	162.5	64
8m4	13.8	0.0634	162.3	405	13.8	0.0829	162.3	405
	Self	0.0244	162.65	406	Self	0.027	162.65	464
8m6	17.1	0.0129	159.65	319	13.8	0.0098	159.9	290
	Self	0.0026	160.15	400	Self	0.0011	160.25	320
8m7	17.1	0.00568	159.9	290	19.7	0.00351	159.75	245
	Self	0.00138	160.45	267	Self	0.000646	160.65	247
8m8	13.8	0.0127	161.2	358	17.1	0.0112	161.15	293
	Self	Damaged			Self	Damaged		
9m1	13.8	0.03516	136.3	340	17.1	0.02862	136.3	340
	Self	0.00567	136.6	303	Self	0.00177	137	228
9m2	13.8	0.0697	136.55	390	10.2	0.07319	136.65	390
	Self	0.034	136.65	390	Self	0.0349	136.8	390
8d1	17.1	0.44	233.3	650				
8d2	13.8	0.55	236.5	720				
8d3	17.1	0.179	228.5	457				
8d4	17.1	0.264	228.5	571				
8d5	17.1	0.364	235.4	588				
8d6	17.1	0.35	234.9	587				
8s1	6.8	0.0303	267.5	232				
8s2	3.4	0.092	271.8	452				
8s3	5.1	0.041	269.5	300				
8s4	3.4	0.0707	270.8	416				
8s5	5.1	0.101	268.5	358				

The performance of the mass loaded sensors was poor compared to the double layer sensors and single layer sensors. Some possible sources of this poor performance include: damping added by the exposed gold layer. The performance of the longer mass (1 mm long) loaded sensors was better. It is possible that more mass loaded material helps to attain DC bias better than the shorter mass loads.

Delamination issue: In most cases, the major delamination occurred between the Metglas layer and the evaporated chrome layer (Fig. A6.). There was high residual stress observed after the gold plating which essentially curved the Metglas substrate. This could be a reason to delaminate all the layers from Metglas. Also, the diffusion of the Cr adhesion layer to the gold could be another reason for delamination.

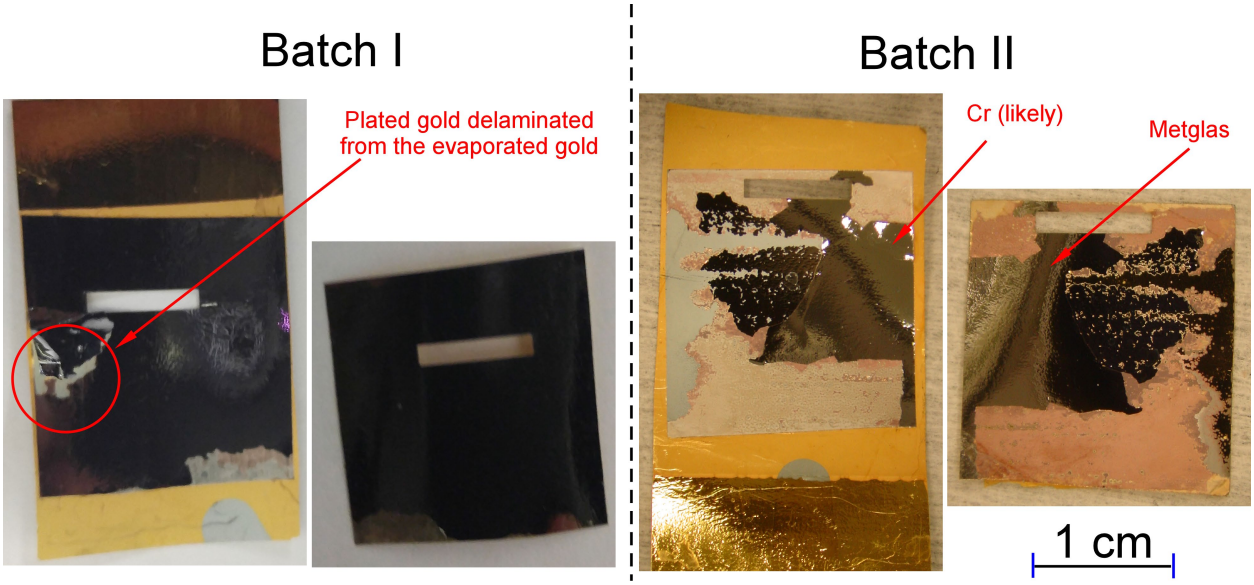

Fig. A6: Photos of delaminated samples while fabricating sensors.

Appendix B: General Principle of Kalman Filtering

A general Kalman filtering approach is described in this appendix. In Kalman filter, for a discrete single output system, the state equation is defined as:

$$x(n+1) = f(x(n)) + w(n) \tag{B.1}$$

where w is Gaussian noise with covariance Q (process noise covariance), *f(x)* is the state function. Q indicates the confidence level of the defined *f(x)* to the process behavior. $Q = 0$ will imply that the state function is expected to be exactly as *f(x)*. In the case of response from a magnetoelastic sensor, f(x) is the envelope of the ringdown signal received from the magnetoelastic sensor, and $Q = 0$ is taken here since this form of f(x) is expected with surety. Only the exact value of the decay time constant is unknown *a priori*; this initially guessed value can be improved after one iteration of Kalman filtering (as described later). In this case, the state function *f(x)* is modeled as:

$$f(x) = (1/e)^{(dt/\tau)} \tag{B.2}$$

where dt is the time step, and τ is the time constant of the exponential decay of the envelope of the ringdown. Here $dt = 1$ μs since it is the sampling interval used in the DSP. τ is estimated from the frequency plot generated from previously implemented DSP steps and used in real time. Now, the observation function is defined as:

$$z(n) = g(x(n)) + v(n) \tag{B.3}$$

where *v(n)* is Gaussian noise with covariance R_n (measurement noise covariance), and *g(x)* is the sensor response. R_n is calculated as the variance of the noise signal around its average value. R_n and the average noise are calculated for each frequency in real time. The observations *z(n)* are the measured values. The algorithm for the Kalman filter is as follows. For KF, one step projection x_p is predicted as:

$$x_p = f(x_i) \tag{B.4}$$

where x_i is the current state. The covariance of x_p is defined as:

$$p_p = fy \cdot p_i \cdot fy' + Q \tag{B.5}$$

where p_i is the estimated state covariance (set to 1 for the initial step, or otherwise calculated in the previous step as p_o), Q is the process noise covariance, and *fy* is the Jacobian of f defined as;

$$fy = \left(df \middle/ dx \right)_{x=x_p} \tag{B.6}$$

and *fy'* is the inverse of *fy*. Kalman gain is defined as:

$$K = \frac{p_p H'}{H.p_p.H' + R_n} \tag{B.7}$$

where R_n is measurement noise covariance and *H* is defined as:

$$H = \left(dg \middle/ dx \right)_{x=x_p} \tag{B.8}$$

and *H'* is the inverse of *H*. With these equations, the output state is estimated as:

$$x_o = x_p + K(z - g(x_p)) \tag{B.9}$$

where z is the observation. and the expected sensor response $g(x)$ is defined as a linear function:

$$g(x) = x_p$$

This gives Jacobian H, as:

$$H = 1 \tag{B.10}$$

(Note that the inverse of H in eq. (7) is set to 0 if H is 0). Further, the covariance of the projected state is updated as:

$$p_o = p_p(1 - K \cdot H) \tag{B.11}$$

and used as p_i in the subsequent filtering step. These steps are repeated for all the data points.

References

[Alt17] Althunian, T.A., de Boer, A., Groenwold, R.H. and Klungel, O.H., "Defining the noninferiority margin and analysing noninferiority: An overview," *British journal of clinical pharmacology*, Vol. 83, No. 8, pp.1636-1642, 2017.

[Ber12] B. Bergmair, T. Huber, F. Bruckner, C. Vogler, and D. Suess, "Removal of earth's magnetic field effect on magnetoelastic resonance sensors by an antisymmetric bias field," *Sensors and Actuators A: Physical, 183, pp.11-15*, 2012.

[Bor10] J. Borkowski, J. Mroczka, "LIDFT method with classic data windows and zero padding in multifrequency signal analysis," Measurement, Vol. 43, No. 10, pp.1595-1602, 2010.

[Bou16] A. Bouchaala, A. H. Nayfeh, M. I. Younis, "Frequency shifts of micro and nano cantilever beam resonators due to added masses," *Journal of Dynamic Systems, Measurement, and Control*, *138*(9), pp.091002, 2016.

[Cai01] Q. Y. Cai, M. K. Jain, and C.A. Grimes, "A wireless, remote query ammonia sensor," *Sensors and Actuators B: Chemical*, *77*(3), pp.614-619, 2001.

[Cai04] Q. Cai, K. Zeng, C. Ruan, T.A. Desai, and C.A. Grimes, "A wireless, remote query glucose biosensor based on a pH-sensitive polymer," *Analytical Chemistry*, *76*(14), pp.4038-4043, 2004.

[Cet97] A. E. Cetin, O. N. Gerek, Y. Yardimci, "Equiripple FIR filter design by the FFT algorithm," *IEEE Signal Processing Magazine*, Vol. 14, No. 2, pp.60-64, 1997.

[Cha13] Y. Chai, S. Horikawa, H.C. Wikle, Z. Wang, and B.A. Chin, "Surface-scanning coil detectors for magnetoelastic biosensors: A comparison of planar-spiral and solenoid coils," *Applied Physics Letters*, *103*(17), p.173510, 2013.

[Cho10] L. Choritz, K. Koynov, G. Renieri, K. Barton, N. Pfeiffer, and H. Thieme, "Surface topographies of glaucoma drainage devices and their influence on human tenon fibroblast adhesion," *Investigative Ophth. & Visual Science*, *51*(8), pp.4047-4053, 2010.

[Chu89] C. K. Chui, G. Chen, "Kalman filtering with real time applications," *Applied Optics*, Vol. 28, pp.1841, 1989.

[Com19] "Effective Mass Calculation COMSOL Multiphysics® for Thermomechanical Calibration," Available online:
https://www.comsol.com/paper/download/187999/hauer_presentation.pdf
Accessed 10/16/2019

[Cvi16] V. Cvintal, M. R. Moster, A. P. Shyu, K. McDermott, F. Ekici, M. J. Pro, and M.

Waisbourd, “Initial experience with the new Ahmed glaucoma valve model M4: short-term results,” *Journal of glaucoma, 25(5), pp.e475-e480*, 2016

[Don07] G. Donelli, E. Guaglianone, R. Di Rosa, F. Fiocca, and A. Basoli, “Plastic biliary stent occlusion: factors involved and possible preventive approaches,” *Clinical Medicine & Research*, *5*(1), pp.53-60, 2007

[Eib05] M. Eibschitz-Tsimhoni, R.M. Schertzer, D.C. Musch, and S.E. Moroi, “Incidence and management of encapsulated cysts following Ahmed glaucoma valve insertion,” *Journal of Glaucoma*, *14*(4), pp.276-279, 2005.

[Fra96] F. M. Frattaroli, D. Reggio, A. Guadalaxara, G. Illomei, and G. Pappalardo, “Benign biliary strictures: a review of 21 years of experience,” *Journal of the American College of Surgeons*, *183*(5), pp.506-513, 1996.

[Gab93] T. B. Gabrielson, “Mechanical-thermal noise in micromachined acoustic and vibration sensors,” *IEEE transactions on Electron Devices*, *40*(5), pp.903-909.

[Ged07] S.J. Gedde, J.C. Schiffman, W.J. Feuer, L.W. Herndon, J.D. Brandt, D.L. Budenz, and Tube Versus Trabeculectomy Study Group, “Treatment outcomes in the tube versus trabeculectomy study after one year of follow-up,” *American Journal of Ophthalmology*, 143(1), pp.9-22, 2007.

[Gre07] S. R. Green, M. T. Richardson, F. A. Shariff, and Y. B. Gianchandani, “Photochemically patterned biliary stents with integrated permanent magnets and deformable assembly features for wireless magnetoelastic tissue growth sensing,” In *Solid-State Sensors, Actuators and Microsystems Conference, 2007. TRANSDUCERS 2007. International* (pp. 213-217). IEEE, 2007

[Gre08] S. R. Green, and Y. B. Gianchandani, "Wireless biliary stent system with wishbone-array resonant magnetoelastic (WARM) sensor and conformal magnetic layer." Hilton Head 2008: *A Solid-State Sensors, Actuators, and Microsystems Workshop*. 2008.

[Gre09a] S.R. Green, and Y.B. Gianchandani, “Wireless magnetoelastic monitoring of biliary stents,” *Journal of Microelectromechanical Systems*, *18*(1), pp.64-78, 2009.

[Gre09b] S. R. Green, “Wireless Magnetoelastic Monitoring of Biliary Stents,” Doctoral dissertation, University of Michigan, 2009.

[Gre10] S. R. Green, and Y. B. Gianchandani, "Tailored magnetoelastic sensor geometry for advanced functionality in wireless biliary stent monitoring systems," *Journal of Micromechanics and Microengineering 20.7 (2010):* 075040, 2010

[Gre13] S. R. Green, R. S. Kwon, G. H. Elta, and Y. B. Gianchandani, “*In vivo* and *in situ* evaluation of a wireless magnetoelastic sensor array for plastic biliary stent monitoring,” *Biomedical microdevices*, *15*(3), pp.509-517, 2013

[Gri99a] C. A. Grimes, K.G. Ong, K. Loiselle, P. G. Stoyanov, D. Kouzoudis, Y. Liu, C. Tong, and F. Tefiku,” Magnetoelastic sensors for remote query environmental monitoring,” *Smart Materials and Structures*, *8*(5), p.639, 1999.

[Gri99b] C. A. Grimes, D. Kouzoudis, K. G. Ong, and R. Crump, "Thin-film magnetoelastic microsensors for remote query biomedical monitoring," *Biomedical Microdevices*, 2(1), 51, 1999

[Gri00a] C. A. Grimes, and D. Kouzoudis, "Remote query measurement of pressure, fluid-flow velocity, and humidity using magnetoelastic thick-film sensors," *Sensors and Actuators A: Physical*, *84*(3), pp.205-212, 2000.

[Gri00b] C. A. Grimes, D. Kouzoudis and C. Mungle, "Simultaneous measurement of liquid density and viscosity using remote query magnetoelastic sensors". *Review of scientific instruments*, *71*(10), pp.3822-3824, 2000.

[Gri02a] C.A. Grimes, C.S. Mungle, K. Zeng, M.K. Jain, W.R. Dreschel, M. Paulose, and K.G. Ong, "Wireless magnetoelastic resonance sensors: A critical review," *Sensors*, *2*(7), pp.294-313, 2002.

[Gri02b] K. Zeng, K. G. Ong, C. Mungle, and C. A. Grimes, "Time domain characterization of oscillating sensors: Application of frequency counting to resonance frequency determination," *Review of Scientific Instruments*, *73*(12), pp.4375-4380, 2002.

[Gri11] C. A. Grimes, S. C. Roy, S. Rani, Q. Cai, "Theory, instrumentation and applications of magnetoelastic resonance sensors: a review," *Sensors*, Vol. 11, No. 3, pp.2809-2844, 2011.

[Grw11] M. S. Grewal, "Kalman filtering," *Springer Berlin Heidelberg*, pp.705-708, 2011.

[Gur07] U. A. Gurkan, and O. Akkus, "An implantable magnetoelastic sensor system for wireless physiological sensing of viscosity. In *Proceeding of the ASME Summer Bioengineering Conference-2007* (pp. 759-760), 2007.

[Hah12] S. Hahn, "Understanding noninferiority trials," *Korean journal of pediatrics*, Vol. 55, No. 11, p.403.2012.

[Her03] G. Herzer, "Magnetic materials for electronic article surveillance," *Journal of Magnetism and Magnetic Materials*, *254*, pp.598-602, 2003.

[Ito11] Y. Ito, T. Kimura, Y. Ago, K. Nam, K. Hiraku, K. Miyazaki, T. Masuzawa, and A. Kishida, "Nano-vibration effect on cell adhesion and its shape," *Bio-medical Materials & Engg., 21*(3), pp.149-158, 2011

[Jia18a] J. Jiang, R. M. Nambisan, S. Green, Y. B. Gianchandani, "Encapsulation Approaches for In-Stent Wireless Magnetoelastic Sensors," *IEEE Transactions on Biomedical Engineering*, Vol. 66, No. 7, pp. 2044-2052, 2018.

[Jia18b] J. Jiang, "Millimeter-Scale Encapsulation of Wireless Resonators for Environmental and Biomedical Sensing Applications," Doctoral dissertation, University of Michigan, 2018.

[Jia18c] Jiang. J. "Three-dimensional Polymeric Packaging of Wireless Micro Resonators for Environmental and Biomedical Sensing Applications", Doctoral Dissertation., University of Michigan, 2018.

[Kal60] R. E. Kalman, "A new approach to linear filtering and prediction problems," Journal of Basic Engineering, Vol. 82, No. 1, pp.35-45, 1960.

[Kat59] H. W. Katz, "Electrostrictive and Magnetostrictive Systems," *Solid State Magnetic and Dielectric Devices*, New York: John Wiley and Sons, 1959

[Kos05] J. Kosel, H. Pfützner, L. Mehnen, E. Kaniusas, T. Meydan, M. Vázquez, M. Rohn, A.M. Merlo, and B> Marquardt, "Non-contact detection of magnetoelastic bilayer position sensors," *Sensors and Actuators A: Physical*, *123*, pp.349-353, 2005.

[Kou00] D. Kouzoudis, and C. A. Grimes, "The frequency response of magnetoelastic sensors to stress and atmospheric pressure," *Smart Materials and Structures*, *9*(6), p.885, 2000.

[Las03] L. L. Laster, M. F. Johnson, "Non-inferiority trials: the 'at least as good as' criterion," *Statistics in Medicine*, *22*(2), pp.187-200, 2003.[Lee14] J.W. Lee, W.Y. Park, E.A. Kim, and I.H Yun, "Tissue response to implanted Ahmed glaucoma valve with adjunctive amniotic membrane in rabbit eyes," *Ophth. Research*, *51*(3), pp.129-139. 2014.

[Lee66] D. B. Lesson, "A simple model of feedback oscillator noise spectrum," *IEEE Proceedings*, 54(2), pp.329-330.

[Les08] E. Lesaffre, " Superiority, equivalence, and non-inferiority trials," *Bulletin of the NYU hospital for joint diseases*, 66(2), 2008.

[Lib96] E. D. Libby, and J. W. Leung, "Prevention of biliary stent clogging: a clinical review." *American Journal of Gastroenterology* 91(7) 1996.

[Mas12] E. J. Mascha, D. I. and Sessler, "Equivalence and noninferiority testing in regression models and repeated-measures designs," Anesthesia & Analgesia, Vol. 112, No. 3, pp.678-687, 2011.

[Mol03] A.C. Molteno, M. Fucik, A.G. Dempster, and T.H. Bevin, "Otago Glaucoma Surgery Outcome Study: factors controlling capsule fibrosis around Molteno implants with histopathological correlation," *Ophthalmology*, *110*(11), pp.2198-2206, 2003.

[Nam17] R. M. Nambisan, S. R. Green, J. D. Stein, Y. B. Gianchandani, "In situ acoustomagnetic interrogation of a glaucoma valve with integrated wireless microactuator. "IEEE 19th International Conference on Solid-State Sensors, Actuators and Microsystems," pp. 383-386, June 2017.

[Ong05] K. G. Ong, X. Yang, K. Zeng, and C. A. Grimes, "Magnetoelastic sensors for biomedical monitoring," *Sensor Letters*, *3*(2), pp.108-116, 2005

[Par02] J.A.T.C. Parker, X.F. Walboomers, J.W. Von den Hoff, J.C. Maltha, J.A. and Jansen, "Soft tissue response to microtextured silicone and poly-L-lactic acid implants: Fibronectin pre-coating vs. radio-frequency glow discharge treatment," *Biomaterials*, *23*(17), pp.3545-3553, 2002.

[Par04] S. H. Park, J. M. Goo, J and C. H. Jo, C "Receiver operating characteristic (ROC) curve: practical review for radiologists," Korean Journal of Radiology, 5(1), pp.11-18, 2004.

[Pep15a] V. Pepakayala, "Micromachined magnetoelastic sensors and actuators for biomedical devices and other applications," Doctoral Dissertation., University of Michigan, 2015.

[Pep15b] V. Pepakayala, J. Stein, and Y. Gianchandani, "Resonant magnetoelastic

microstructures for wireless actuation of liquid flow on 3D surfaces and use in glaucoma drainage implants," *Microsystems & Nanoengineering*, *1*, 2015.

[Pep17] V. Pepakayala, S. R. Green, and Y. B. Gianchandani, "Wireless strain measurement with a micromachined magnetoelastic resonator using ringdown frequency locking," *ISSS journal of micro and smart systems*, *6*(1), pp.3-13, 2017

[Pie89] A. D. Pierce, "Acoustics: an introduction to its physical principles and applications," 2nd ed. *Acoustical Society of America*, Woodbury, NY, pp. 213–245, 1989

[Pin01] E. Pina, E. Burgos, C. Prados, J. M. González, A. Hernando, M. C. Iglesias, J. Poch, and C. Franco, "Magnetoelastic sensor as a probe for muscular activity: An *in vivo* experiment," *Sensors and Actuators A: Physical*, *91*(1), pp.99-102, 2001

[Qui06] H.A. Quigley, and A.T. Broman, "The number of people with glaucoma worldwide in 2010 and 2020," *British Journal of Ophthalmology*, *90*(3), pp.262-267, 2006.

[Reh16] S. Rehal, T. P. Morris, K. Fielding, J. R. Carpenter, P. P. Phillips, "Non-inferiority trials: are they inferior? A systematic review of reporting in major medical journals," *BMJ open*, *6*(10), pp. 012594, 2016.

[Rhe95] R. Rhea, "Oscillator design and computer simulation," *The Institution of Engineering and Technology*, 1995.

[Roh83] J.W. Rohen, "Why is Intraocular Pressure Elevated in Chronic Simple Glaucoma?: Anatomical Considerations," *Ophthalmology*, *90*(7), pp.758-765, 1983.

[Ros07] T. Rossing, Springer handbook of acoustics, Springer Science & Business Media, 2007.

[Rua04] C. Ruan, K. Zeng, O.K. Varghese, and C.A. Grimes," A staphylococcal enterotoxin B magnetoelastic immunosensor," *Biosensors and Bioelectronics*, *20*(3), pp.585-591, 2004.

[She10] W. Shen, Z. Zhang, S. Horikawa, A. Zhang, J. Teng, L. C. Mathison, and B. A. Chin, "Time domain characterization of magnetoelastic sensors: A pulse method for resonance frequency determination," *Review of Scientific Instruments*, *81*(8), p.084702, 2010.

[Soc19] "P Value from T Score Calculator," Available online: https://www.socscistatistics.com/pvalues/tdistribution.aspx Accessed 25/09/2019.

[Sur18] S. Surwase, H. Balakrishnan, S. K. Acharya, G. K. Makharia, G. Kumaraswamy, B. L. Prasad, "Accelerated in vitro model for occlusion of biliary stents: investigating the role played by dietary fibre," BMJ Innovations, Vol. 4, No. 1, pp. 39-45, 2018.

[Vis12] A. Viswanath, S.R. Green, J. Kosel, and Y.B. Gianchandani, "Metglas–Elgiloy bi-layer, stent cell resonators for wireless monitoring of viscosity and mass loading," *Journal of Micromechanics and Microengineering*, *23*(2), p.025010, 2012.

[Vis13] A. Viswanath, S. R. Green, J. Kosel, and Y. B. Gianchandani, "Conformally integrated stent cell resonators for wireless monitoring of peripheral artery disease," In *Micro Electro Mechanical Systems (MEMS), 2013 IEEE 26th International Conference on* (pp. 1069-1072). IEEE, 2013

[Vla11] E. Vlaisavljevich, L. P. Janka, K. G. Ong, and R. M. Rajachar, “Magnetoelastic materials as novel bioactive coatings for the control of cell adhesion,” *IEEE Transactions on Biomedical Engineering*, *58*(3), pp.698-704, 2011.

[Whe28] A. H. Wheeler, "Simple inductance formulas for radio coils,” Proceedings of the Institute of Radio Engineers, Vol. 16, No. 10, pp.1398-1400, 1928.

[Yan06] Y. T. Yang, “Phase noise of nanoelectromechancial systems”, Doctoral dissertation, California Institute of Technology, 2006.

[Zwe93] M. H. Zweig, G. Campbell, “Receiver-operating characteristic (ROC) plots: a fundamental evaluation tool in clinical medicine,” *Clinical chemistry*, *39*(4), pp.561-577, 1993.